
Longer ranged interactions in quantum point contacts

Lukas Weidinger



Master's Thesis
Theoretical and Mathematical Physics

Chair of Theoretical Solid State Physics
Faculty of Physics
Ludwig-Maximilians-University Munich

Supervisor: Prof. Dr. Jan von Delft

November 2014

Abstract

Since 26 years, it is well known that quantum point contacts (QPCs) show quantized conductance steps in terms of the conductance quantum $G_Q = \frac{2e^2}{h}$ when the voltage of the applied gates and thus the barrier height of the QPC is varied. This behavior can be understood in a non-interacting particle picture, assuming that the transport stems from single electrons traveling through the QPC. However, since the earliest experiments there were deviations from this ideal behavior observed. The most striking one, the so called "0.7-anomaly" is a dip in the conductance step between the pinch-off and the first conductance plateau at roughly $G \approx 0.7 \cdot G_Q$. Ever since, that anomaly has been the subject of controversial discussion which is still going on. Recently, Bauer et al. [1] managed to give a consistent explanation for the 0.7-anomaly, identifying it's origin in a smeared van Hove singularity in the center of the QPC. Using an short ranged interaction model for the QPC, the conductance was explicitly calculated, employing the functional renormalization group (fRG) method. As an approximation within this method they applied a so called "coupled ladder approximation" (CLA) which reduces efficiently the degrees of freedom by exploiting the particular structure of the fRG flow equations.

In this thesis, we will develop an fRG scheme suitable to take longer ranged interactions into account. Explicitly, we will set up a coupled ladder approximation (CLA) similar to the one of Bauer et al., but allowing also longer ranged contributions for the bare interaction. Using various symmetries of our system, we end up at a system of ODEs which we solve numerically.

We then study the results of this new algorithm using the previous model with short ranged interactions, as well as models with longer ranged interactions. For the latter, we observe that in a certain regime increased long ranged interactions are capable of actually increasing the conductance. We study this -on first sight- contra intuitive result by examining conductance, density, and magnetic susceptibility for various parameters. As cause of this physical behavior we suspect a Wigner like crystallization process of the QPC in the presence of long ranged interactions.

To conclude this thesis, we further examine two more cases modeled by short ranged interactions, namely the transition between a QPC and a quantum dot (QD) and a QPC with non-parabolic potential. This was motivated by the improved convergence of our new algorithm compared to the previous method since the last two cases are known to suffer from convergence issues due to the relative flat barrier top.

Contents

Abstract	3
1. Introduction	7
1.1. The experimental setup: 2DEG	7
1.2. The quantum point contact	8
2. The functional renormalization group - a summary	11
2.1. General definitions	11
2.2. A comment on symmetry breaking	13
2.3. Derivation of the flow equations	14
3. Modeling of QPCs	19
3.1. From the continuous to a discrete model	19
3.2. Hilbert space and model Hamiltonian	20
3.3. Integrating out the leads	21
3.4. The linear response conductance	23
3.5. The density	34
3.6. The susceptibility	37
4. Approximative treatment of longer ranged feedback	40
4.1. The bare vertex	40
4.2. The splitting in different channels	41
4.3. The coupled ladder approximation	44
4.4. A comment on symmetries	48
4.5. The flow equations in general coordinates	53
4.6. A suitable basis transformation	55
4.7. The flow equations in the new notation	59
5. A brief revision of the physics in quantum point contacts	68
6. Numerical results	77
6.1. Test of the new method on the on-site model	77
6.2. Introduction of longer ranged interactions	90
6.2.1. Results for longer ranged interactions	96
6.3. Higher order potentials for QPCs	104
6.4. Transition between QPC and quantum dot	106
7. Summary and outlook	113

A. Concrete form of the Kubo susceptibility	116
B. List of Figures	118
C. Bibliography	120
Acknowledgment	122

1. Introduction

The transport through devices on the nano-scale has been studied extensively in the last decades involving a wide range of experiments. From the "classical" quantum point contact and quantum dots in 2 dimensional electron gases (2DEG) studied in [2] one has evolved to using various kinds of other structures, including actual "wires". A prominent example for this development is the use of single carbon nanotubes, see for example [3] which are there grown to connect two electrodes. Nevertheless, the understanding of the transport mechanisms in this devices is still a topic of extensive research. One of the interesting many body features, the 0.7-anomaly which was already observed back in [2] and first reported in [4], has received a lot of controversy discussion over the years. Prominent approaches to explain the 0.7-anomaly where for example based on the Kondo effect [5], [6] or a spontaneous spin polarization [7] in the QPC.

The 0.7 feature was also extensively studied in our group, foremost by Florian Bauer and Jan Heyder who managed to give a consistent and physical intuitive explanation for this effect [1]. They actually computed the drop in the conductance at the 0.7 shoulder using an numerical fRG-approach. Furthermore, they where also able to explain the reason for this anomaly, namely a smeared out van Hove singularity [8] in the local density of states at the center of the QPC. When measuring a conductance trace of a QPC by varying the gate voltage, this smeared out singularity causes the anomalous effects in the observables whenever it is close to the chemical potential.

This many-body effects of the QPC will be elaborated in detail in chapter 5. As a starting ground, we will use this introductory chapter to explain the concept of a QPC and briefly summarize it's non-interacting key features.

1.1. The experimental setup: 2DEG

The typical environment in which quantum point contacts (QPCs) are realized is a 2-dimensional electron gas (2DEG) at the junction of oppositely doped semiconductors. A often used setup is, for example, a thin layer of n-doped GaAlAs on a p-doped semiconductor of GaAs [9]. Since the two materials have the same lattice constant, one gets a clean interface without defects acting as impurities. Due to the different doping we have a difference in the bare chemical potentials (i.e. the potentials before the two layers are brought together). Thus, when the two layers touch, the conductance band of the GaAlAs will be depleted and the electrons wander to the valence band of the GaAs ¹ (see fig. 1.1).

¹The interested reader may find a thorough introduction to the physics in the 2DEG in the textbook "Quantum Transport" by Nazarov & Blanter [9], from which we have adopted fig. 1.1 and fig. 1.2

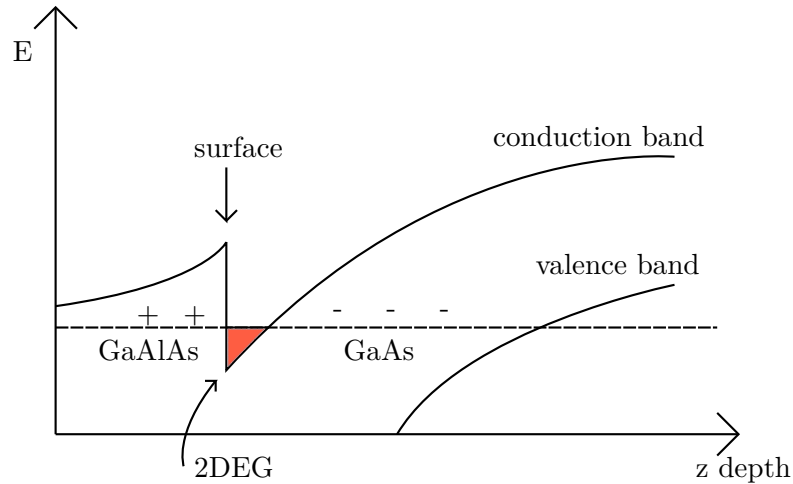


Figure 1.2.: Cut through the semiconducting layers of our GaAlAs-GaAs structure. The 2DEG (here depicted in red) forms at the junction between the layers.

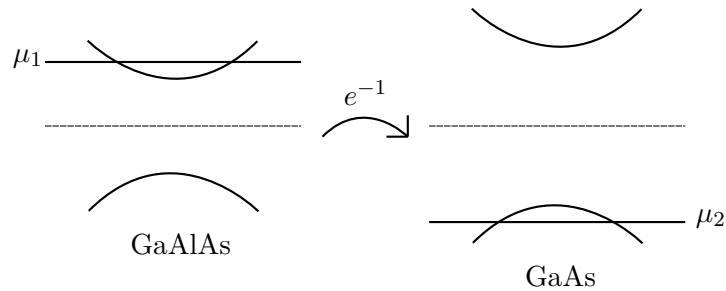


Figure 1.1.: Bandstructures of the semiconductors GaAlAs and GaAs. Note the different chemical potentials due to the respective doping.

If one inspects this redistribution of electrons closer, one finds the structure indicated in Figure 1.2.

The feature relevant for our considerations is the metallic behavior which is narrowly constricted in z direction, at the junction of the two layers. This forms then effectively a two dimensional electron gas (2DEG). Via electrodes, so called gates, attached on top of our GaAlAs-GaAs structure, one can realize a multitude of different potential shapes in this two dimensional plane. A quantum point contact (QPC) is given by such a special potential shape explained in the next section.

1.2. The quantum point contact

A QPC is given by a narrow constriction in the otherwise non depleted 2-dimensional electron gas. Essentially, this can be modeled by a saddlepoint potential like the one shown in fig. 1.3. If one applies a voltage difference V_{sd} between the leads L (source) and

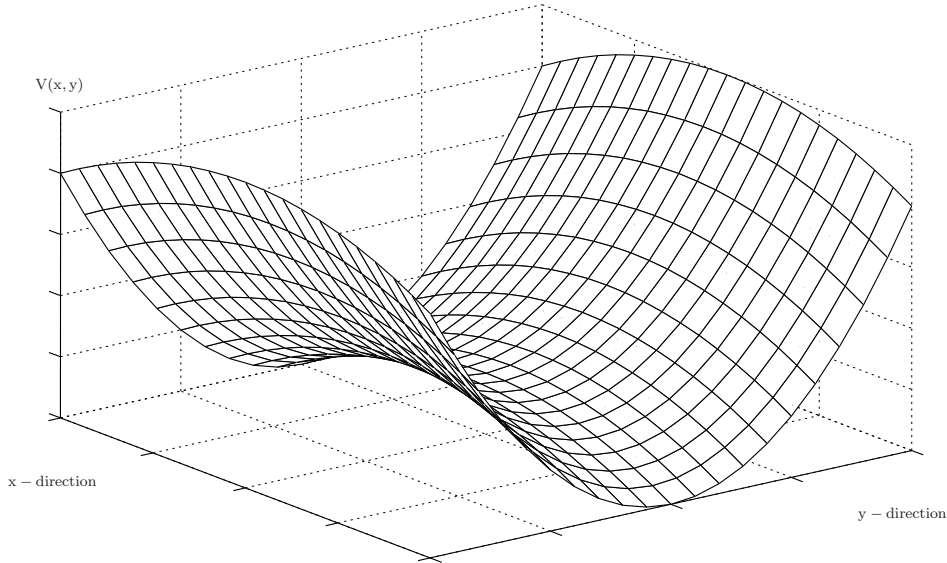


Figure 1.3.: Saddlepoint like potential form which we assume to model the shape of our QPC.

R (drain), i.e. if one effectively changes the chemical potential between the right and the left hand side of our QPC, an electric current from L to R will be induced. To linear order in V , this current I will be given by $I = G \cdot V$, where G is the linear conductance of our QPC. The probably most astonishing feature of the conductance, namely the quantization of G in steps of $G_Q = \frac{2e^2}{h}$ in terms of the gate voltage V_g (and thus in the barrier height of the QPC) can already be seen in a very simple, non interacting model. In fact, this quantization was predicted by Landauer already in 1957 [10] but was the first time observed in an experiment only back in 1988 by Van Wees et al. [2].

If we assume that the potential $V(x, y)$ in fig. 1.3 changes only adiabatically in x , the “walls” of our QPC are locally flat and we can make a local separation of variables

$$\Psi_n(x, y, z) = \psi(x)\phi_n(a(x), b(x), y, z), \quad (1.1)$$

where the wave functions $\phi_n(a, b, y, z)$ are determined by the local shape of the constriction (here assumed to be rectangular with side lengths $a(x), b(x)$)². Due to the finite shape of the constriction, these transverse wave functions ϕ_n are quantized with a discrete quantum number n and obey the differential equation

$$\left[-\frac{\hbar}{2m} \left(\frac{\partial^2}{\partial y^2} + \frac{\partial^2}{\partial z^2} \right) + U_x(y, z) \right] \phi_n(x, y, z) = E_n(x)\phi_n(x, y, z). \quad (1.2)$$

On the other hand, the longitudinal wave function $\psi(x)$ has then to fulfill the differential equation

$$\left(-\frac{\hbar^2}{2m} \frac{\partial^2}{\partial x^2} + E_n(x) \right) \psi(x) = E\psi(x), \quad (1.3)$$

²The actual shape of the walls does not really matter for our argument

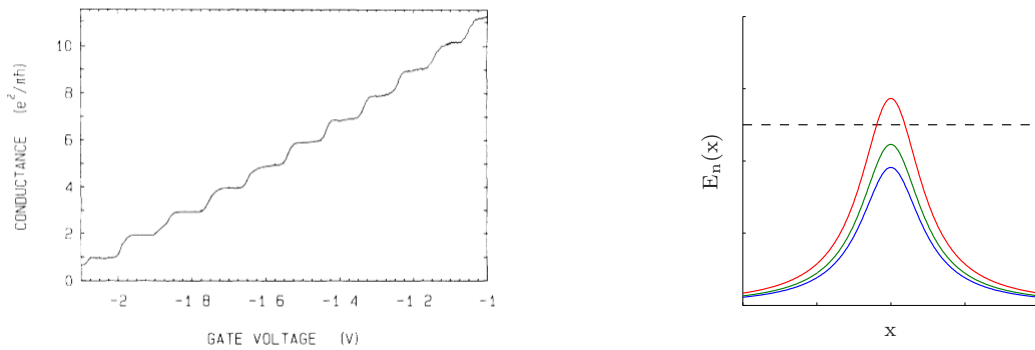


Figure 1.4.: Left: Measurement of the quantized conductance in the original paper by Van Wees et al. [2] from 1988. The height of the barrier is here reduced with increasing the gate voltage. Right: Graphical depiction of the channels leading to the conductance quantization. We sketched here a set of curves $E_n(x)$ corresponding to different channels; the ones below the E line represent open channels, the one which intersects E is a closed channel.

thus $E_n(x)$ acts like an effective one-dimensional potential. The quantization of the Conductance (see fig. 1.4) can then be understood in the following way:

At an given energy E of an incoming electron there are only a finite number of $E_n(x)$ which are everywhere smaller than E (see fig. 1.4). For this so called "channels" the QPC is open, and one can show that each of this channels contributes to the conductance with the conductance quantum $G_Q = \frac{2e^2}{h}$ (see for example [9][chapter 1.2]).

Thus, if in our case one increases the gate voltage V_g , the constriction gets narrower and therefore the quantization of ϕ_n changes, namely the energies $E_n(x)$ become smaller. As soon as they are so small that the number of $E_n(x)$ which are everywhere below E changes by one, the conductance increases by a step $\Delta G = G_Q$. In our work, we will exclusively study the transition between $G = 0$ and $G = G_Q$, i.e. the behavior of the lowest sub-band in the QPC. In order to get a more quantitative description of transport, we will study models which take also an interaction between electrons into account. Since these models will be in general not analytically solvable, one has to apply numerical methods to obtain approximate solutions. Our tool of choice will be the numerical renormalization group (fRG), discussed in the next chapter.

2. The functional renormalization group - a summary

2.1. General definitions

As starting point for the physical description of our many body system, we use the partition function in the grand canonical ensemble

$$Z = \text{Tr} e^{-\beta(\hat{H}-\mu\hat{N})}, \quad (2.1)$$

where \hat{H} is the Hamiltonian of our system, \hat{N} the particle number operator and we assume thermal equilibrium. If we express \hat{H} in terms of creation and annihilation operators and bring it in normal order, we can use coherent states, i.e. eigenstates of the annihilation operators to cast it into the usual functional integral form. In our case of interest, i.e. fermionic systems these coherent states will be constructed as an expansion of our Hilbert space using Grassmann numbers. Without elaborating to much on this we recommend the book of Negele-Orland [11] to the interested reader. The final form of the partition function, under the assumption of thermal equilibrium thus reads:

$$Z = \int \mathcal{D}\psi^* \psi e^{-\int_0^\beta d\tau [\sum_l \psi_l^*(\tau+0^+) (\frac{\partial}{\partial \tau} - \mu) \psi_l(\tau) + H(\{\psi^*\}, \{\psi\})]}, \quad (2.2)$$

where is already employed a rewriting in a continuous form for the limit of the actual discrete functional integral.

In the following, we will usually be concerned with an Hamiltonian of the form

$$H(\psi^*, \psi) = \underbrace{\sum_l \epsilon_l \psi_l^*(\tau + 0^+) \psi_l(\tau)}_a + \frac{1}{4} \underbrace{\sum_{i,j,k,l} \bar{v}_{i,j,k,l} \psi_i^*(\psi + 0^+) \psi_j^*(\tau + 0^+) \psi_l(\tau) \psi_k(\tau)}_b, \quad (2.3)$$

i.e. with an quadratic part (a) (for notational simplicity assumed to be diagonal) expressing the non interacting properties and a second, two particle part (b) expressing the interaction between particles.

To outline the idea of the function renormalization group (fRG)¹ approach, we introduce first a few nomenclature conventions². We define the n-particle imaginary-time Green's

¹For getting an overview in this technique, the author would like to recommend the works of V. Meden [12], C. Karrasch [13], and S. Andergassen [14]

²We will mainly follow here the conventions of Bauer et al.

function as follows:

$$\begin{aligned} \mathcal{G}^{(n)}(\alpha_1\tau_1, \dots, \alpha_n\tau_n | \alpha_{2n}\tau_{2n}, \dots, \alpha_{n+1}\tau_{n+1}) = \\ (-1)^n \frac{1}{Z} \int \mathcal{D}[\psi_\alpha^*(\tau)\psi_\alpha(\tau)] e^{-\int_0^\beta d\tau [\sum_\alpha \psi_\alpha^*(\tau)(\frac{\partial}{\partial\tau} - \mu)\psi_\alpha(\tau) + H(\psi_\alpha^*(\tau), \psi_\alpha(\tau))]} \\ \times \psi_{\alpha_1}(\tau) \dots \psi_{\alpha_n}(\tau_n) \psi_{\alpha_{n+1}}^*(\tau_{n+1}) \dots \psi_{\alpha_{2n}}^*(\tau_{2n}) \end{aligned} \quad (2.4)$$

and the corresponding generating function as

$$\begin{aligned} W(J_\alpha^*(\tau), J_\alpha(\tau)) &:= \frac{1}{Z} \int \mathcal{D}[\psi_\alpha^*(\tau)\psi_\alpha(\tau)] e^{-\int_0^\beta d\tau [\sum_\alpha \psi_\alpha(\tau)(\partial_\tau - \mu)\psi_\alpha(\tau) + H(\psi_\alpha^*(\tau), \psi_\alpha(\tau))]} \\ &\times e^{-\int_0^\beta d\tau \sum_\alpha [J_\alpha^*(\tau)\psi_\alpha(\tau) + \psi_\alpha^*(\tau)J_\alpha(\tau)]} \\ &=: \langle e^{-\int_0^\beta d\tau \sum_\alpha [J_\alpha^*(\tau)\psi_\alpha(\tau) + \psi_\alpha^*(\tau)J_\alpha(\tau)]} \rangle, \end{aligned} \quad (2.5)$$

where we have as usual denoted the thermal average as $\langle \cdot \rangle$. With this generating function, the n -particle imaginary-time Green's function can be expressed as:

$$\mathcal{G}^{(n)}(\alpha_1\tau_1; \dots; \alpha_n\tau_n | \alpha'_1\tau'_1; \dots; \alpha'_n\tau'_n) = \frac{\delta^{2n} \mathcal{G}(J_\alpha^*(\tau), J_\alpha(\tau))}{\delta J_{\alpha_1}^*(\tau_1) \dots \delta J_{\alpha_n}^*(\tau_n) \delta J_{\alpha'_n}(\tau'_n) \dots \delta J_{\alpha'_1}(\tau'_1)} \Bigg|_{J^*=J=0}. \quad (2.6)$$

If we furthermore denote with $\mathcal{G}_c^{(n)}(\alpha_1\tau_1; \dots; \alpha_n\tau_n | \alpha'_1\tau'_1; \dots; \alpha'_n\tau'_n)$ the n -particle connected Green's function, i.e the parts of the n -particle Green's function which consist of diagrams in which all the external legs are connected, it can be shown via the linked cluster theorem (see for example the book of Negele-Orland [11][chapter 2.4]) that

$$\mathcal{G}_c^{(n)}(\alpha_1\tau_1; \dots; \alpha_n\tau_n | \alpha'_1\tau'_1; \dots; \alpha'_n\tau'_n) = \frac{\delta^{2n} W^c(J_\alpha^*(\tau), J_\alpha(\tau))}{\delta J_{\alpha_1}^*(\tau_1) \dots \delta J_{\alpha_n}(\tau_n) \delta J_{\alpha'_n}(\tau'_n) \dots \delta J_{\alpha'_1}(\tau'_1)} \Bigg|_{J^*=J=0}, \quad (2.7)$$

where the generating function of the connected Green's function W^c is given by

$$W^c(J_\alpha^*(\tau), J_\alpha(\tau)) = \ln W(J_\alpha^*(\tau), J_\alpha(\tau)). \quad (2.8)$$

Finally, we can define the generating functional of the one-particle irreducible vertex function as the Legendre transform of W^c

$$\begin{aligned} \Gamma[\phi_\alpha^*(\tau), \phi_\alpha(\tau)] &:= -W^c(J_\alpha^*(\tau), J_\alpha(\tau)) - \sum_\gamma \int_0^\beta d\tau' [\phi_\gamma^*(\tau') J_\gamma(\tau') + J_\gamma^*(\tau') \phi_\gamma(\tau')] \\ &+ \sum_{\gamma, \bar{\gamma}} \int_0^\beta d\tau' d\tau'' \phi_\gamma^*(\tau') [\mathcal{G}^0]_{\gamma\bar{\gamma}}^{-1}(\tau', \tau'') \phi_{\bar{\gamma}}(\tau''), \end{aligned} \quad (2.9)$$

where the last term in this line, which does not depend on the source fields $J_\alpha^*(\tau)$ and $J_\alpha(\tau)$ was merely added for later convenience, and $\phi_\alpha^*(\tau), \phi_\alpha(\tau)$ are defined in terms of the source fields $J_\alpha^*(\tau), J_\alpha(\tau)$ as:

$$\begin{aligned} \phi_\alpha &= \langle a_\alpha \rangle_{J^*, J}^{\text{connected}} = \langle \psi_\alpha \rangle_{J^*, J}^{\text{connected}} = \\ &- \frac{\delta}{\delta J_\alpha^*(\tau)} W^c[J_\alpha^*(\tau), J_\alpha(\tau)], \end{aligned} \quad (2.10)$$

and analog for $\phi_\alpha^*(\tau)$:

$$\phi_\alpha^*(\tau) = \langle a_\alpha^\dagger(\tau) \rangle_{J^*, J}^{\text{connected}} = -(-1) \frac{\delta}{\delta J_\alpha(\tau)} W^c[J_\alpha^*(\tau), J_\alpha(\tau)] = \frac{\delta}{\delta J_\alpha(\tau)} W^c[J_\alpha^*(\tau), J_\alpha(\tau)]. \quad (2.11)$$

The one-particle irreducible vertex functions can then be obtained via

$$\Gamma_{m\phi^*, n\phi}(\alpha_1\tau_1, \dots, \alpha_m\tau_m | \alpha'_1\tau'_1, \dots, \alpha'_n\tau'_n) = \frac{\delta^{m+n}}{\delta\phi_{\alpha_1}^*(\tau_1) \cdots \delta\phi_{\alpha_m}^*(\tau_m) \delta\phi_{\alpha'_n}(\tau'_n) \cdots \delta\phi_{\alpha'_1}(\tau'_1)} \Gamma[\phi_\alpha^*(\tau), \phi_\alpha(\tau)] \Big|_{J_\alpha^*=J_\alpha=0}. \quad (2.12)$$

2.2. A comment on symmetry breaking

If we look at the partition function (2.2), we see that both the measure $\mathcal{D}\psi^*\psi$ as well as the action $S(\psi, \psi^*)$ are invariant under the $U(1)$ symmetry

$$\psi_l \rightarrow \psi_l e^{i\alpha}, \quad \psi_l^* \rightarrow \psi_l^* e^{-i\alpha} \quad (2.13)$$

for all indices l . We assume that this symmetry is also manifest in our physical system, i.e. the set of paths \mathfrak{M} over which we integrate in (2.2) is also invariant under this transformation. Because of this unbroken $U(1)$ symmetry of our system it is immediately clear that expectation values of products of unequal numbers of ψ 's and ψ^* 's vanish. For example we have:

$$\begin{aligned} \langle \psi_\alpha \rangle &= e^{i\alpha} \langle \psi_\alpha \rangle \forall \alpha \in [0, 2\pi] \\ \Rightarrow \langle \psi_\alpha \rangle &= 0. \end{aligned} \quad (2.14)$$

Thus, this $U(1)$ symmetry of our system translates into particle conservation, i.e. the number of electrons in our system does not change. Furthermore, we show in the following that this symmetry implies that the only non vanishing vertex functions have an equal number of incoming and outgoing legs, i.e. the only non zero terms in equation (2.12) will be of the form

$$\gamma_m(\alpha_1\tau_1, \dots, \alpha_m\tau_m | \alpha'_1\tau'_1, \dots, \alpha'_m\tau'_m) = \frac{\delta^{2m} \Gamma[\phi_\alpha^*(\tau), \phi_\alpha(\tau)]}{\delta\phi_{\alpha_1}^*(\tau_1) \cdots \delta\phi_{\alpha_m}^*(\tau_m) \delta\phi_{\alpha'_m}(\tau'_m) \cdots \delta\phi_{\alpha'_1}(\tau'_1)} \Big|_{J_\alpha^*=J_\alpha=0}. \quad (2.15)$$

To show this, it suffices to prove that $\Gamma(\phi^*, \phi)$ is invariant under the $U(1)$ symmetry $\phi \rightarrow e^{i\alpha}\phi$, $\phi^* \rightarrow e^{-i\alpha}\phi^*$, which makes sure that $\Gamma(\phi^*, \phi)$ consists only of terms with equal powers in ϕ and ϕ^* . For this we first look back at (2.5). By performing a change of variables $\psi \rightarrow e^{i\alpha}\psi$, $\psi^* \rightarrow e^{-i\alpha}\psi^*$ and using the invariance of \mathfrak{M} , $\mathcal{D}\psi^*\psi$ and S under this transformation, we see immediately that $W(e^{-i\alpha}J_\alpha^*(\tau), e^{i\alpha}J_\alpha(\tau)) = W(J_\alpha^*(\tau), J_\alpha(\tau))$, i.e. W is $U(1)$ symmetric. Then also W^c has this symmetry, which can be expressed in infinitesimal terms as

$$\int_0^\beta d\tau \left[i\alpha J_\alpha(\tau) \frac{\delta W^c(J^*, J)}{\delta J_\alpha(\tau)} + (-i\alpha) J_\alpha^*(\tau) \frac{\delta W^c(J^*, J)}{\delta J_\alpha^*(\tau)} \right] = 0. \quad (2.16)$$

We now look at the definition of $\Gamma(\phi^*, \phi)$ as the Legendre transform of W^c (eq. (2.9)) and obtain the reciprocal relations for the effective potential

$$\begin{aligned} \frac{\delta\Gamma(\phi_\alpha^*(\tau), \phi_\alpha(\tau))}{\delta\phi_\alpha(\tau)} &= \sum_\gamma \int_0^\beta d\tau' \left[-\frac{\delta W^c}{\delta J_\gamma^*(\tau')} \frac{\delta J_\gamma^*(\tau')}{\delta\phi_\alpha(\tau)} - \frac{\delta W^c}{\delta J_\gamma(\tau')} \frac{\delta J_\gamma(\tau')}{\delta\phi_\alpha(\tau)} + \phi_\gamma^*(\tau') \frac{\delta J_\gamma(\tau')}{\delta\phi_\alpha(\tau)} \right. \\ &\quad \left. - \frac{\delta J_\gamma^*(\tau')}{\delta\phi_\alpha(\tau)} \phi_\gamma(\tau') + J_\gamma^*(\tau') \delta_{\alpha\gamma} \delta(\tau - \tau') - \phi_\gamma^*(\tau') [\mathcal{G}^0]_{\gamma\alpha}^{-1}(\tau', \tau) \right] \\ &= J_\alpha^*(\tau) - \sum_\gamma \int_0^\beta d\tau' \phi_\gamma^*(\tau') [\mathcal{G}^0]_{\gamma\alpha}^{-1}(\tau', \tau) \end{aligned} \quad (2.17)$$

and

$$\begin{aligned} \frac{\delta\Gamma(\phi^*, \phi)}{\delta\phi_\alpha^*(\tau)} &= \sum_\gamma \int_0^\beta d\tau' \left[-\frac{\delta W^c}{\delta J_\gamma^*(\tau')} \frac{\delta J_\gamma^*(\tau')}{\delta\phi_\alpha^*(\tau)} - \frac{\delta W^c}{\delta J_\gamma(\tau')} \frac{\delta J_\gamma(\tau')}{\delta\phi_\alpha^*(\tau)} \right. \\ &\quad \left. - \delta_{\alpha\gamma} \delta(\tau' - \tau) J_\gamma(\tau') + \phi_\gamma^*(\tau') \frac{\delta J_\gamma(\tau')}{\delta\phi_\alpha^*(\tau)} - \frac{\delta J_\gamma^*(\tau')}{\delta\phi_\alpha^*(\tau)} \phi_\gamma(\tau') + [\mathcal{G}^0]_{\alpha\gamma}^{-1}(\tau, \tau') \phi_\gamma(\tau') \right] \\ &= -J_\alpha(\tau) + \sum_\gamma \int_0^\beta d\tau' [\mathcal{G}^0]_{\alpha\gamma}^{-1}(\tau, \tau') \phi_\gamma(\tau'). \end{aligned} \quad (2.18)$$

If we use this relations in equation (2.16) we get

$$\begin{aligned} 0 &= \int_0^\beta \left[(i\alpha) \left(-\frac{\delta\Gamma}{\delta\phi_\alpha^*(\tau)} + \sum_\gamma \int_0^\beta d\tau' [\mathcal{G}^0]_{\alpha\gamma}^{-1}(\tau, \tau') \phi_\gamma(\tau') \right) \phi_\alpha^*(\tau) \right. \\ &\quad \left. + (-i\alpha) \left(\frac{\delta\Gamma}{\delta\phi_\alpha(\tau)} + \sum_\gamma \int_0^\beta d\tau' \phi_\gamma^*(\tau') [\mathcal{G}^0]_{\gamma\alpha}^{-1}(\tau', \tau) \right) (-\phi_\alpha(\tau)) \right] \\ &= \int_0^\beta d\tau \left[(i\alpha) \left(-\frac{\delta\Gamma}{\delta\phi_\alpha^*(\tau)} \right) \phi_\alpha^*(\tau) + (-i\alpha) \left(-\frac{\delta\Gamma}{\delta\phi_\alpha(\tau)} \right) \phi_\alpha(\tau) \right]. \end{aligned} \quad (2.19)$$

Thus, $\Gamma(\phi^*, \phi)$ is invariant under the $U(1)$ symmetry $\phi \rightarrow e^{i\alpha}\phi$, $\phi^* \rightarrow e^{-i\alpha}\phi^*$ which we wanted to show.

2.3. Derivation of the flow equations

By further examination of W and Γ (which we will do a little bit later) it can be established that the self-energy Σ which is given by the famous Dyson equation

$$\mathcal{G}^{-1} = [\mathcal{G}^0]^{-1} - \Sigma, \quad (2.20)$$

can be expressed as

$$\gamma_1(\alpha_1, \tau_1 | \alpha'_1, \tau'_1) = \left. \frac{\delta^2\Gamma}{\delta\phi_{\alpha_1}^* \delta\phi_{\alpha_1}} \right|_{\phi=\phi^*=0} = -\Sigma. \quad (2.21)$$

Thus, in order to get the full propagator of the system it suffices to determine the self energy (we assume that \mathcal{G}^0 of the non-interacting system is known), which we can relate to determining the vertex functions $\{\gamma_m\}$ or Γ , respectively. This is the purpose of our fRG-scheme. The general idea is to introduce a flow parameter Λ into the propagator \mathcal{G}^0 of the non-interacting system, i.e. we consider a function $\mathcal{G}^0(\Lambda)$ with $\mathcal{G}^0(\Lambda_{\text{final}}) = \mathcal{G}^0$ and $\mathcal{G}^0(\Lambda_{\text{initial}})$ is something very simple, in our case $\mathcal{G}^0(\Lambda_{\text{initial}}) = 0$. Thinking in terms of diagrams, this initial conditions immediately imply for the one- and two-particle vertices: $\gamma_1^{\Lambda_{\text{initial}}} = 0$ and $\gamma_2^{\Lambda_{\text{initial}}} = \nu$, where ν is the bare vertex.

We can now derive a flow equation for our system in Λ and follow the flow of this equation from the simple system at Λ_{initial} to the full interacting system at Λ_{final} . Concretely, we consider for this purpose the vertex functions. Via (2.9) the flow parameter Λ is introduced in the generating functional of the vertex functions and therefore also contained in them. In order to get the desired system of differential equations, we differentiate (2.9) with respect to Λ and get

$$\begin{aligned}
\frac{d}{d\Lambda}\Gamma^\Lambda(\phi^*, \phi) &= \frac{d}{d\Lambda} \left[-W^{c\Lambda}(J_\alpha^*(\tau), J_\alpha(\tau)) - \sum_\gamma \int_0^\beta d\tau' [\phi_\gamma^*(\tau') J_\gamma(\tau') + J_\gamma^*(\tau') \phi_\gamma(\tau')] \right. \\
&\quad \left. + \sum_{\gamma, \tilde{\gamma}} \int_0^\beta d\tau' d\tau'' \phi_\gamma^*(\tau') [\mathcal{G}^0]_{\gamma\tilde{\gamma}}^{-1}(\tau', \tau'') \phi_{\tilde{\gamma}}(\tau'') \right] \\
&= -\frac{d}{d\Lambda} W^{c\Lambda}(J_\alpha^*(\tau), J_\alpha(\tau), \Lambda) - (\phi^*, \frac{d}{d\Lambda} J^\Lambda) \\
&\quad - (\frac{d}{d\Lambda} J^{*\Lambda}, \phi) + (\phi^*, \frac{d}{d\Lambda} [\mathcal{G}^{0\Lambda}]^{-1} \phi) \\
&= -\frac{\partial}{\partial \Lambda} W^{c\Lambda}(J^*, J, \Lambda) - \frac{d}{d\Lambda} J^* \frac{\delta W^c}{\delta J^*} - \frac{d}{d\Lambda} J \frac{\delta W^c}{\delta J} \\
&\quad - (\phi^*, \frac{d}{d\Lambda} J^\Lambda) - (\frac{d}{d\Lambda} J^{*\Lambda}, \phi) + (\phi^*, \frac{\partial}{\partial \Lambda} [\mathcal{G}^{0-1}]^\Lambda \phi),
\end{aligned} \tag{2.22}$$

and by definition of ϕ^*, ϕ (equations ((2.11)),((2.10))) we arrive at

$$\frac{d}{d\Lambda}\Gamma^\Lambda(\phi^*, \phi) = -\frac{\partial}{\partial \Lambda} W^{c\Lambda} + (\phi^*, \partial_\Lambda [\mathcal{G}^0]^{-1\Lambda} \phi) \tag{2.23}$$

(where we have employed the anticommutation relations for Grassmann variables). The partial derivative $\frac{\partial}{\partial \Lambda} W^{c\Lambda}$ can be obtained from differentiating equation (2.8) partially with respect to Λ .³

$$\begin{aligned}
W^\Lambda(J^*, J) &= \frac{1}{Z(\Lambda)} \int d\psi^* d\psi \exp\{S_0(\Lambda) - S_{\text{int}} - (\psi^*, J) - (J^*, \psi)\} = \\
&\quad \frac{Z_0(\Lambda)}{Z(\Lambda)} \cdot \frac{1}{Z_0(\Lambda)} \int d\psi^* d\psi \exp\{S_0(\Lambda) - S_{\text{int}} - (\psi^*, J) - (J^*, \psi)\} \\
&\Rightarrow \frac{\partial}{\partial \Lambda} W^c = \underbrace{\frac{\partial}{\partial \Lambda} \ln \left(\frac{Z_0(\Lambda)}{Z(\Lambda)} \right)}_{=: c(\Lambda)} + \frac{1}{W} \cdot \partial_\Lambda W.
\end{aligned} \tag{2.24}$$

³To illustrate the idea clearly and don't get lost in notation we forgo indices.

For this expression one evaluates first

$$\begin{aligned}
\partial_\Lambda \frac{e^{S_0(\Lambda)}}{Z_0(\Lambda)} &= \frac{1}{Z_0(\Lambda)} \partial_\Lambda S_0(\Lambda) e^{S_0(\Lambda)} - \left(\frac{1}{Z_0(\Lambda)} \right)^2 e^{S_0(\Lambda)} \partial_\Lambda Z_0(\Lambda) \\
&= \frac{1}{Z_0(\Lambda)} \dot{S}_0(\Lambda) e^{S_0(\Lambda)} - \left(\frac{1}{Z_0(\Lambda)} \right)^2 e^{S_0(\Lambda)} \int \mathcal{D}\psi^* \psi \dot{S}_0(\Lambda) e^{S_0(\Lambda)} \\
&= \frac{e^{S_0(\Lambda)}}{Z_0(\Lambda)} \left[(\psi^*, \partial_\Lambda [\mathcal{G}^0(\Lambda)]^{-1} \psi) - (\psi^*, \frac{e^{S_0(\Lambda)}}{Z_0} \partial_\Lambda [\mathcal{G}^0(\Lambda)]^{-1} \psi) \right] \\
&= \frac{e^{S_0(\Lambda)}}{Z_0(\Lambda)} \left[(\psi^*, \partial_\Lambda [\mathcal{G}^0(\Lambda)]^{-1} \psi) - \text{Tr}(\mathcal{G}^0(\Lambda) \partial_\Lambda [\mathcal{G}^0(\Lambda)]^{-1}) \right].
\end{aligned} \tag{2.25}$$

and therefore

$$\frac{\partial}{\partial \Lambda} W^c(\Lambda) = - \text{Tr}(\mathcal{G}^0(\Lambda) \partial_\Lambda [\mathcal{G}^0(\Lambda)]^{-1}) - \underbrace{\frac{1}{W(\Lambda)} \left(\frac{\delta}{\delta \eta}, \partial_\Lambda [\mathcal{G}^0(\Lambda)]^{-1} \frac{\delta}{\delta \eta^*} \right)}_{=:(2)} W(\Lambda) + c(\Lambda). \tag{2.26}$$

For (2) we can straight forwardly evaluate

$$\begin{aligned}
(2) &= e^{-W^c(\Lambda)} \left(\frac{\delta}{\delta J}, \partial_\Lambda [\mathcal{G}^0(\Lambda)]^{-1} \frac{\delta}{\delta J^*} \right) e^{W^c(\Lambda)} + c(\Lambda) = \\
&= \left(\frac{\delta W^c(\Lambda)}{\delta J}, \partial_\Lambda [\mathcal{G}^0(\Lambda)]^{-1} \frac{\delta W^c(\Lambda)}{\delta J^*} \right) + \left(\frac{\delta}{\delta J}, \partial_\Lambda [\mathcal{G}^0(\Lambda)]^{-1} \frac{\delta}{\delta J^*} \right) W^c(\Lambda) + c(\Lambda) \\
&= \left(\frac{\delta W^c(\Lambda)}{\delta J}, \partial_\Lambda [\mathcal{G}^0(\Lambda)]^{-1} \frac{\delta W^c(\Lambda)}{\delta J^*} \right) + \sum_{k,k'} \left[\frac{\delta^2 W^c(\Lambda)}{\delta J_k \delta J_k^*} \partial_\Lambda [\mathcal{G}^0(\Lambda)]_{k,k'}^{-1} \right] + c(\Lambda) = \\
&= \left(\frac{\delta W^c(\Lambda)}{\delta J}, \partial_\Lambda [\mathcal{G}^0(\Lambda)]^{-1} \frac{\delta W^c(\Lambda)}{\delta J^*} \right) - \text{Tr} \left(\partial_\Lambda [\mathcal{G}^0(\Lambda)]^{-1} \frac{\delta^2 W^c(\Lambda)}{\delta J^* \delta J} \right) + c(\Lambda).
\end{aligned} \tag{2.27}$$

And thus we have

$$\begin{aligned}
\frac{\partial}{\partial \Lambda} W^c(\Lambda) &= - \text{Tr}(\mathcal{G}^0(\Lambda) \partial_\Lambda [\mathcal{G}^0(\Lambda)]^{-1}) + \text{Tr} \left(\partial_\Lambda [\mathcal{G}^0(\Lambda)]^{-1} \frac{\delta^2 W^c(\Lambda)}{\delta J^* \delta J} \right) \\
&\quad - \left(\frac{\delta W^c(\Lambda)}{\delta J}, \partial_\Lambda [\mathcal{G}^0(\Lambda)]^{-1} \frac{\delta W^c(\Lambda)}{\delta J^*} \right).
\end{aligned} \tag{2.28}$$

If we now insert this into (2.23), we end up with

$$\begin{aligned}
\frac{d}{d\Lambda} \Gamma^\Lambda(\phi^*, \phi) &= \left(\frac{\delta W^c(\Lambda)}{\delta J}, \partial_\Lambda [\mathcal{G}^0(\Lambda)]^{-1} \frac{\delta W^c(\Lambda)}{\delta J^*} \right) - \text{Tr} \left(\partial_\Lambda [\mathcal{G}^0(\Lambda)]^{-1} \frac{\delta^2 W^c(\Lambda)}{\delta J^* \delta J} \right) \\
&\quad + \text{Tr}(\mathcal{G}^0(\Lambda) \partial_\Lambda [\mathcal{G}^0(\Lambda)]^{-1}) + (\phi^*, \partial_\Lambda [\mathcal{G}^0]^{-1\Lambda} \phi) \\
&\stackrel{(2.10),(2.11)}{=} - \text{Tr} \left(\partial_\Lambda [\mathcal{G}^0(\Lambda)]^{-1} \frac{\delta^2 W^c(\Lambda)}{\delta J^* \delta J} \right) + \text{Tr}(\mathcal{G}^0(\Lambda) \partial_\Lambda [\mathcal{G}^0(\Lambda)]^{-1}) - c(\Lambda).
\end{aligned} \tag{2.29}$$

By looking at this differential equation, one sees that the only remaining task is to express the term $\frac{\delta^2 W^c(\Lambda)}{\delta J^* \delta J}$ in terms of derivatives of Γ^Λ . If we succeed in this, we remain

with our desired system of differential equations for the vertex function. In order to proceed, we use the identity

$$\int d2 \left(\begin{array}{cc} \frac{\delta^2 W^c}{\delta J^*(3)\delta J(2)} & (-1) \frac{\delta^2 W^c}{\delta J^*(3)\delta J^*(2)} \\ (-1) \frac{\delta^2 W^c}{\delta J(3)\delta J(2)} & \frac{\delta^2 W^c}{\delta J(3)\delta J^*(2)} \end{array} \right) \underbrace{\left(\begin{array}{cc} \frac{\delta^2 \Gamma}{\delta \phi^*(2)\delta \phi(1)} + [\mathcal{G}^0]^{-1} & \frac{\delta^2 \Gamma}{\delta \phi^*(2)\delta \phi^*(1)} \\ \frac{\delta^2 \Gamma}{\delta \phi(2)\delta \phi(1)} & \frac{\delta^2 \Gamma}{\delta \phi(2)\delta \phi^*(1)} - [[\mathcal{G}^0]^{-1}]^T \end{array} \right)}_{:=A}$$

$$= \delta(31) \begin{pmatrix} 1 & 0 \\ 0 & 1 \end{pmatrix}, \quad (2.30)$$

which can be obtained straight forwardly by calculation of the derivative

$$\frac{\delta \phi}{\delta \phi} = \frac{\delta}{\delta \phi} \left(-\frac{\delta}{\delta J^*} W^c \right) \quad (2.31)$$

and the corresponding derivatives $\frac{\delta \phi}{\delta \phi^*}$, $\frac{\delta \phi^*}{\delta \phi}$ and $\frac{\delta \phi^*}{\delta \phi^*}$.

Thus, in order to determine $\frac{\delta^2 W^c(\Lambda)}{\delta J^* \delta J}$ in (2.29), we have to expand $(A^{-1})_{11}$ in powers of ϕ^* , ϕ . By looking at the structure of A , this is most conveniently achieved by first expanding $(A^{-1})_{11}$ in powers of

$$U(\Lambda) := \frac{\delta^2 \Gamma(\Lambda)}{\delta \phi^* \delta \phi} - \frac{\delta^2 \Gamma(\Lambda)}{\delta \phi^* \delta \phi} \Big|_{\phi=\phi^*=0}, \quad (2.32)$$

which has by default no 0-th order term in the fields ϕ, ϕ^* . Thus, if we have an expansion of $(A^{-1})_{11} = \frac{\delta^2 W^c(\Lambda)}{\delta J^* \delta J}$ in $U(\Lambda)$ and compare powers of ϕ, ϕ^* in equation (2.29), we have to consider for terms of power $(\phi\phi^*)^n$ only terms on the r.h.s. up to power U^n . Our desired expansion in U is achieved by writing

$$\begin{aligned} \frac{\delta^2 \Gamma}{\delta \phi^* \delta \phi} + [\mathcal{G}^0]^{-1} &= \frac{\delta^2 \Gamma}{\delta \phi^* \delta \phi} - \frac{\delta^2 \Gamma(\Lambda)}{\delta \phi^* \delta \phi} \Big|_{\phi=\phi^*=0} + \frac{\delta^2 \Gamma(\Lambda)}{\delta \phi^* \delta \phi} \Big|_{\phi=\phi^*=0} + [\mathcal{G}^0]^{-1} = \\ &\stackrel{\text{Dyson}}{=} \underbrace{\frac{\delta^2 \Gamma}{\delta \phi^* \delta \phi} - \frac{\delta^2 \Gamma(\Lambda)}{\delta \phi^* \delta \phi} \Big|_{\phi=\phi^*=0}}_{U(\Lambda)} + \mathcal{G}^{-1}, \end{aligned} \quad (2.33)$$

and analog

$$\frac{\delta^2 \Gamma}{\delta \phi \delta \phi^*} - [\mathcal{G}^0]^{-1T} = -U(\Lambda)^T - \mathcal{G}^{-1T}. \quad (2.34)$$

Therefore, we end up with

$$\begin{aligned}
A^{-1} &= \begin{pmatrix} \frac{\delta^2 \Gamma}{\delta \phi^* \delta \phi} + [\mathcal{G}^0]^{-1} & \frac{\delta^2 \Gamma}{\delta \phi^* \delta \phi^*} \\ \frac{\delta^2 \Gamma}{\delta \phi \delta \phi} & \frac{\delta^2 \Gamma}{\delta \phi \delta \phi^*} - [\mathcal{G}^0]^{-1T} \end{pmatrix}^{-1} = \begin{pmatrix} U(\Lambda) + \mathcal{G}^{-1} & \frac{\delta^2 \Gamma}{\delta \phi^* \delta \phi^*} \\ \frac{\delta^2 \Gamma}{\delta \phi \delta \phi} & -U(\Lambda)^T - \mathcal{G}^{-1T} \end{pmatrix}^{-1} = \\
&= \left[\begin{pmatrix} \mathcal{G}^{-1} & 0 \\ 0 & -\mathcal{G}^{-1T} \end{pmatrix} + \begin{pmatrix} U(\Lambda) & \frac{\delta^2 \Gamma}{\delta \phi^* \delta \phi^*} \\ \frac{\delta^2 \Gamma}{\delta \phi \delta \phi} & -U(\Lambda)^T \end{pmatrix} \right]^{-1} = \\
&= \left[1 - \underbrace{\begin{pmatrix} -\mathcal{G}^{-1} & 0 \\ 0 & \mathcal{G}^{-1T} \end{pmatrix}^{-1}}_{=:B} \underbrace{\begin{pmatrix} U(\Lambda) & \frac{\delta^2 \Gamma}{\delta \phi^* \delta \phi^*} \\ \frac{\delta^2 \Gamma}{\delta \phi \delta \phi} & -U(\Lambda)^T \end{pmatrix}}_{=:C} \right]^{-1} \cdot \begin{pmatrix} \mathcal{G}^{-1} & 0 \\ 0 & -\mathcal{G}^{-1T} \end{pmatrix}^{-1}, \tag{2.35}
\end{aligned}$$

and by expanding the inverse into a power series

$$\begin{aligned}
A^{-1} &= [1 - BC]^{-1}(-B) = \sum_{k=0}^{\infty} (BC)^k (-B) = 1(-B) + BC(-B) + \dots = \\
&= \begin{pmatrix} \mathcal{G} & 0 \\ 0 & -\mathcal{G}^T \end{pmatrix} - \begin{pmatrix} \mathcal{G} & 0 \\ 0 & -\mathcal{G}^T \end{pmatrix} \begin{pmatrix} U(\Lambda) & \frac{\delta^2 \Gamma}{\delta \phi^* \delta \phi^*} \\ \frac{\delta^2 \Gamma}{\delta \phi \delta \phi} & -U(\Lambda)^T \end{pmatrix} \begin{pmatrix} \mathcal{G} & 0 \\ 0 & -\mathcal{G}^T \end{pmatrix} + \dots \tag{2.36}
\end{aligned}$$

we arrive at

$$A_{11}^{-1} = \mathcal{G} - \mathcal{G}U(\Lambda)\mathcal{G} + \dots \tag{2.37}$$

Now we can determine the hierarchy of flow equations by plugging expansion (2.36) in equation (2.29) and count powers of ϕ, ϕ^* . As we have already seen in our section about symmetry breaking, Γ can only contain products of equal powers of ϕ and ϕ^* and we get for the first two vertex functions:

$$\begin{aligned}
\frac{d}{d\Lambda} \gamma_0 &= \text{Tr}[\mathcal{G}^0(\Lambda) \partial_\Lambda [\mathcal{G}^0(\Lambda)]^{-1}] - \text{Tr}[\partial_\Lambda [\mathcal{G}^0(\Lambda)]^{-1} \mathcal{G}] - c(\Lambda) \\
\frac{d}{d\Lambda} \gamma_1 &= \text{Tr}[\mathcal{G} \partial_\Lambda [\mathcal{G}^0(\Lambda)]^{-1} \mathcal{G} \gamma_2] = \text{Tr}[S \gamma_2], \tag{2.38}
\end{aligned}$$

where $S := \mathcal{G} \partial_\Lambda [\mathcal{G}^0(\Lambda)]^{-1} \mathcal{G}$ is the so called "single scale propagator" since it will turn out that S depends only on the scale Λ and not on another frequency. Last but not least, we obtain for the flow of the two-particle vertex:

$$\begin{aligned}
\frac{d}{d\Lambda} \gamma_2(k'_1, k'_2; k_1, k_2) &= \text{Tr}[S \gamma_3(k'_1, k'_2, \cdot; k_1, k_2, \cdot)] \\
&+ \text{Tr}[S \gamma_2(\cdot, \cdot; k_1, k_2) \mathcal{G}^T \gamma_2(k'_1, k'_2; \cdot, \cdot)] \\
&- \text{Tr}[S \gamma_2(k'_1, \cdot; k_1, \cdot) \mathcal{G} \gamma_2(k'_2, \cdot; k_2, \cdot)] \\
&- \text{Tr}[S \gamma_2(k'_2, \cdot; k_2, \cdot) \mathcal{G} \gamma_2(k'_1, \cdot; k_1, \cdot)] \\
&+ \text{Tr}[S \gamma_2(k'_2, \cdot; k_1, \cdot) \mathcal{G} \gamma_2(k'_1, \cdot; k_2, \cdot)] \\
&+ \text{Tr}[S \gamma_2(k'_1, \cdot; k_2, \cdot) \mathcal{G} \gamma_2(k'_2, \cdot; k_1, \cdot)]. \tag{2.39}
\end{aligned}$$

In this work we will make the usual fRG-approximation, namely to truncate the hierarchy of flow equations at this point and set all vertices $\gamma_{m>2} = 0$.

3. Modeling of QPCs

3.1. From the continuous to a discrete model

In chapter 1, we have modeled our QPC by two semi-finite leads joined by a narrow constriction which is described by a potential $V(x, y)$, see figure 1.3. Furthermore, we have seen that we get an essentially one dimensional model whose Hamiltonian is given by

$$H_0 = -\frac{\hbar^2}{2m}\partial_x^2 + V(x) - \frac{\sigma}{2}B, \quad (3.1)$$

where we have inserted a Zeeman term to include the effects of an external magnetic field coupled to the spin of the electrons. As discussed, the one-dimensional potential consists of the "real" part, that is the part of $V(x, y)$ along $y = 0$, as well as the part $E_n(x)$ coming from the energy of the transverse component of the wave function. Therefore,

$$V(x) = V(x, y = 0) + E_n(x). \quad (3.2)$$

In order to carry out numerical calculations, it is convenient to discretize this model by assuming $x = ja$ to be lattice points where a is the lattice spacing and $j \in \mathbb{Z}$ is the site index. In this discrete form the spacial derivatives become

$$\begin{aligned} \partial_x \psi(x) &= \frac{\psi((j+1)a) - \psi(ja)}{a} \\ \partial_x^2 \psi(x) &= \frac{\psi((j+1)a) - 2\psi(ja) + \psi((j-1)a)}{a^2}. \end{aligned} \quad (3.3)$$

Thus, we can rewrite our continuous Hamiltonian (3.1) in discrete form as

$$H_0(\psi) = -\frac{\hbar^2}{2m} \frac{\psi((j+1)a) - 2\psi(ja) + \psi((j-1)a)}{a^2} + (V_j - \frac{\sigma}{2}B)\psi(ja). \quad (3.4)$$

Since our systems contains not only one but many electrons, it is convenient to employ second quantization and rewrite this single particle Hamiltonian on Fock space. If the energy is measured relative to the chemical potential at half filling $\mu = 0$ where the hopping τ is defined via $\frac{m}{\hbar^2} = \frac{1}{2\tau a^2}$, we end up with

$$H_0 = \sum_{j,\sigma} [(V_j - \frac{\sigma}{2}B - \mu)d_{j,\sigma}^\dagger d_{j,\sigma} - \tau(d_{j+1,\sigma}^\dagger d_{j,\sigma} + h.c.)]. \quad (3.5)$$

In the following, we will divide this H_0 in two parts $H_0 = H_c + H_l$ ¹, where H_c consists of the sites in the center of our QPC, i.e the sites we assume to have $V_j \neq 0$. On the other hand, H_l consists only of sites where $V_j = 0$, namely the leads. For a graphical depiction of this model, see fig. 3.1.

¹ H_c "center" and H_l "lead"

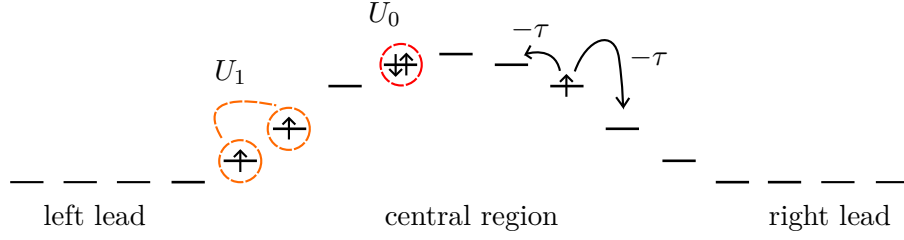


Figure 3.1.: Graphical depiction of our model. We have the hopping $-\tau$ between neighboring lattice sites, a quadratic potential barrier in the central region, as well as off- and on-site interactions. In the leads neither a potential nor interactions are present, leaving us thus just with two semi-infinite tight binding chains. Notice that due to the Pauli principle, the on-site interaction can only occur between electrons with opposite spins, whereas the off-site interactions are spin independent.

3.2. Hilbert space and model Hamiltonian

Before we proceed further and introduce interactions, we will just say a few words about the Hilbert space \mathcal{H} of our model to make sure everything is well defined. In the discrete form, the Hilbert space of a single electron is $\mathcal{H}_s = L^2(\mathbb{Z})$ ². The full physical Hilbert space of our model will then be

$$\mathcal{H} = \mathcal{F} \left(\bigotimes_{N=0}^{\infty} L^2(\mathbb{Z})^N \right), \quad (3.6)$$

i.e. the fermionic Fock space over $L^2(\mathbb{Z})$. Lastly, for our fRG approach we have expanded this physical Hilbert space using a Grassmann algebra generated by ξ_j, ξ_j^* where $j \in \mathbb{Z}$ as scalars, instead of the complex numbers \mathbb{C} .

Having specified our Hilbert space, we can now write down the full model including interactions

$$H = H_l + H_c + H_{lc}, \quad (3.7)$$

with

$$\begin{aligned} H_l &= - \sum_{\sigma} \sum_{s=L, R} \sum_{j=1}^{\infty} [\mu_s c_{j,s,\sigma}^{\dagger} c_{j,s,\sigma} + \tau (c_{j+1,s,\sigma}^{\dagger} c_{j+1,s,\sigma} + h.c.)] \\ H_c &= \sum_{j=-N}^N \sum_{\sigma} [E_{j,\sigma} d_{j,\sigma}^{\dagger} d_{j,\sigma} - \tau (d_{j+1,\sigma} d_{j,\sigma} + h.c.)] \\ &\quad + \frac{1}{2} \sum_{\sigma_1, \sigma_2} \sum_{l,k} U(l,k) d_{l,\sigma_1}^{\dagger} d_{k,\sigma_2}^{\dagger} d_{k,\sigma_2} d_{l,\sigma_1} \\ H_{lc} &= - \tau \sum_{\sigma} (c_{1,L,\sigma}^{\dagger} d_{-N,\sigma} + d_{N,\sigma}^{\dagger} c_{1,R,\sigma} + h.c.), \end{aligned} \quad (3.8)$$

²Note that due to the discreteness of our model, we don't have to worry about the differentiability of our functions. Thus, we are allowed to consider here simply $L^2(\mathbb{Z})$ without additional restrictions.

where $E_{j,\sigma} = (V_j - \mu - \frac{\sigma B}{2})$. We take here interactions $U(l, k)$ only in the central region into account. This is physical sensible due to the following reasoning: The effective interaction strength is given by the product $U \cdot \mathcal{A}_j(\mu)$ -which we will see later- where $\mathcal{A}_j(\mu)$ is the local density of states at the chemical potential. Since $\mathcal{A}_j(\mu)$ has its maximum in the central region but is outside of it much smaller, we can neglect it in the leads and therefore start from the beginning with non interacting leads. As mentioned before, our goal is now to obtain the full propagator \mathcal{G} of our system.

3.3. Integrating out the leads

By construction, the bare interaction in the leads is zero. Looking at the fRG equations (2.38) and (2.39), we see that this property remains during the whole flow. Both the derivatives of the self-energy Σ as well as of the two particle vertex γ_2 have on their right hand side (r.h.s.) a vertex γ_2 . Thus, if one index in $\frac{d}{d\Lambda}\Sigma$ or $\frac{d}{d\Lambda}\gamma_2$ is taken from the leads, this particular index enters also in γ_2 in the r.h.s.. Since at the beginning of the flow $\gamma_2 = \nu = 0$ in the leads and thus $\frac{d}{d\Lambda}\Sigma = 0$, $\frac{d}{d\Lambda}\gamma_2 = 0$, the self-energy and the two particle vertex will remain zero during the flow. What remains is a system of flow equations with a number of spacial degrees of freedom (dof) $\leq (2N+1)^2 + (2N+1)^4$, since the indices in $\gamma_1(j_1, j'_1)$ and $\gamma_2(j_1, j_2; j'_1, j'_2)$ have to be taken only from the $2N+1$ sites of the central region. Thus, the interaction does not enter the leads. It is then convenient to split our single particle Hilbert space between the interacting central region and the leads. According to this splitting, the Hamiltonian can be divided into H_{cc} , H_{cl} , H_{lc} , and H_{ll} :

$$H = \begin{pmatrix} H_{cc} & H_{cl} \\ H_{lc} & H_{ll} \end{pmatrix}. \quad (3.9)$$

Using Dyson's equation

$$\mathcal{G} = \frac{1}{[\mathcal{G}^0]^{-1} + \gamma_1} \quad (3.10)$$

the full propagator \mathcal{G} can be obtained via

$$\mathcal{G}(z) = \begin{pmatrix} z - H_{cc} - \Sigma_{cc} & -H_{cl} \\ -H_{lc} & z - H_{ll} \end{pmatrix}^{-1} =: \begin{pmatrix} \mathcal{G}_{cc} & \mathcal{G}_{cl} \\ \mathcal{G}_{lc} & \mathcal{G}_{ll} \end{pmatrix} \quad (3.11)$$

since $\Sigma_{lc} = \Sigma_{cl} = \Sigma_{ll} = 0$.

Using the general formula for the inverse of a block matrix

$$\begin{bmatrix} A & B \\ C & D \end{bmatrix}^{-1} = \begin{bmatrix} (A - BD^{-1}C)^{-1} & -A^{-1}B(D - CA^{-1}B)^{-1} \\ -D^{-1}C(A - BD^{-1}C)^{-1} & (D - CA^{-1}B)^{-1} \end{bmatrix}, \quad (3.12)$$

we straight forwardly end up with

$$\begin{aligned} \mathcal{G}_{cc} &= \frac{1}{z - H_{cc} - \Sigma_{cc} - H_{cl}g_l H_{lc}}, \\ \mathcal{G}_{ll} &= \frac{1}{z - H_{ll} - H_{lc}g_c H_{cl}}, \\ \mathcal{G}_{cl} &= \mathcal{G}_{cc}H_{cl}g_l = g_c H_{cl}\mathcal{G}_{ll}, \\ \mathcal{G}_{lc} &= g_l H_{lc}\mathcal{G}_{cc} = \mathcal{G}_{ll}H_{lc}g_c, \end{aligned} \quad (3.13)$$

with $g_l = \frac{1}{z-H_{ll}}$ and $g_c = \frac{1}{z-H_{cc}}$. Furthermore, we can also express \mathcal{G}_{ll} in terms of \mathcal{G}_{cc} as

$$\mathcal{G}_{ll} = g_l + g_l H_{lc} \mathcal{G}_{cc} H_{cl} g_l. \quad (3.14)$$

We note here that these expressions for the different parts of the propagator in terms of \mathcal{G}_{cc} can be interpreted very easily. For example, $\mathcal{G}_{cl} = \mathcal{G}_{cc} H_{cl} g_l$ describes the movement of a particle from the leads to the central region. The internal sums are easily evaluated since H_{cl} consists only of two entries, namely the coupling of the uttermost sites of the central region to the first sites of the corresponding leads. Since the leads themselves are not coupled directly, i.e.

$$H_{ll} = \begin{pmatrix} H_{Ll} & 0 \\ 0 & H_{Rl} \end{pmatrix}, \quad (3.15)$$

the lead propagator splits also in this blocks

$$g_l = \begin{pmatrix} g_{Ll} & 0 \\ 0 & g_{Rl} \end{pmatrix} \quad (3.16)$$

and equation $\mathcal{G}_{cl} = \mathcal{G}_{cc} H_{cl} g_l$ describes the following electron movement: Assume we start at some point in the right lead. From there we can move arbitrarily in the right lead till at some time we end up at the first site of the lead and then hop to the site N (the right outermost site) of the dot. From that site, we can then move arbitrarily (including moving back into the leads) to the point of the central region where the movement is supposed to end. Equation $\mathcal{G}_{ll} = g_l + g_l H_{lc} \mathcal{G}_{cc} H_{cl} g_l$ admits an analogous interpretation. The movement to go from one lead point to another lead point consists of the motion which is purely contained in the leads (g_l), as well as the motion where at least once we enter and leave the central region ($g_l H_{lc} \mathcal{G}_{cc} H_{cl} g_l$).

From the relations (3.13) we see that the only remaining task is to calculate the propagator $\mathcal{G}_{cc} = \frac{1}{z-H_{cc}-\Sigma_{cc}-H_{cl}g_l H_{lc}}$. To achieve this, we notice again that the internal summation over site indices in $H_{cl}g_l H_{lc}$ collapses into a single term since the coupling in H_{lc} connects only the outermost sites of the central region with the respective leads and the leads themselves are not directly coupled. It thus suffices to know the value of g_l at the innermost sites $R,1$ and $L,1$ of the leads. Since the right and the left lead are symmetric to each other, these two values are the same. This leaves us just with the task to calculate the one-one component $g_{11}(z)$ of the propagator of a semi-infinite tight binding chain, which again is most easily established via the matrix identity (3.12). The Hamiltonian is here (for notational convenience we will not explicitly write down a possible Zeeman term in the leads but absorb it into the chemical potential μ which thus might depend on spin)

$$H_{tb} = \begin{pmatrix} \mu & -\tau & & 0 \\ -\tau & \mu & -\tau & \\ & -\tau & \ddots & \ddots \\ 0 & & \ddots & \ddots \\ & & & \ddots \end{pmatrix} \quad (3.17)$$

and therefore the propagator reads

$$g(z) = \begin{pmatrix} z - \mu & \tau & 0 & \cdots \\ \tau & z - \mu & \tau & \\ 0 & \tau & \ddots & \\ \vdots & & \ddots & \ddots \end{pmatrix}^{-1}. \quad (3.18)$$

If we use now the inversion formula for block matrices (3.12), we get

$$\begin{aligned} g_{11}(z) &= [z - \mu - (\tau \ 0 \ \cdots) g(z) (\tau \ 0 \ \cdots)]_{11}^{-1} \\ &= [z - \mu - \tau^2 g_{11}(z)]_{11}^{-1} \\ &\Rightarrow (z - \mu) g_{11}(z) - \tau^2 g_{11}(z)^2 - 1 = 0 \\ &\Rightarrow g_{11}(z) = \frac{1}{2\tau^2} \left[z + \mu \pm i\sqrt{4\tau^2 - (z + \mu)^2} \right]. \end{aligned} \quad (3.19)$$

To determine the "±" sign, we use the general properties a propagator has to satisfy. Firstly, it must hold $\lim_{|z| \rightarrow \infty} g_{11}(z) = 0$. We immediately see that $\lim_{R \rightarrow \infty} g_{11}(iR) = 0$, only if we choose the "-" sign and $\lim_{R \rightarrow \infty} g_{11}(-iR) = 0$, only if we choose the "+" sign. Secondly, since the only brunch cut of the propagator can be at the real axis, this sign change has to occur there:

$$g_{11}(z) = \begin{cases} \frac{1}{2\tau^2} [z + \mu - i\sqrt{4\tau^2 - (z + \mu)^2}] , & \text{if } \text{Im}(z) > 0 \\ \frac{1}{2\tau^2} [z + \mu + i\sqrt{4\tau^2 - (z + \mu)^2}] , & \text{if } \text{Im}(z) < 0 \end{cases}. \quad (3.20)$$

Thus, we end up with

$$\mathcal{G}_{cc} = \left[z - H_{cc} - \Sigma_{cc} - \begin{pmatrix} g_{11} \cdot \tau^2 & 0 \\ 0 & g_{11} \cdot \tau^2 \end{pmatrix} \right]^{-1} \quad (3.21)$$

and equipped with this machinery, we can come to the calculation of our observables in the next sections.

3.4. The linear response conductance

In physical terms, the conductance is the dependence of the current in our system on an external applied source-drain voltage. Since this is obviously a non equilibrium quantity, we use linear response theory to calculate it in 1st order. For our derivation, we will first specify what we understand as the current. Due to the form of our Hamiltonian

$$H = H_l + H_c + H_{lc} \quad (3.22)$$

with

$$H_l = - \sum_{\sigma} \sum_{s=L,R} \sum_{j=1}^{\infty} [\mu_s c_{j,s,\sigma}^{\dagger} c_{j,s,\sigma} + \tau (c_{j+1,s,\sigma}^{\dagger} c_{j,s,\sigma} + h.c.)] \quad (3.23)$$

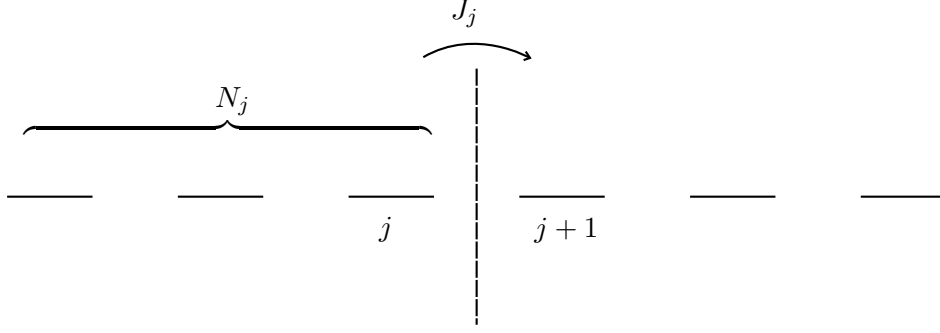


Figure 3.2.: The current operator at site j measures the change of the total particle number N_j to the left of site j

$$H_c = \sum_{j=-N}^N \sum_{\sigma} [E_{j\sigma} d_{j\sigma}^{\dagger} d_{j\sigma} - \tau (d_{j+1\sigma}^{\dagger} d_{j\sigma} + h.c.)] + \frac{1}{2} \sum_{\sigma_1, \sigma_2} \sum_{l, k} U(l-k) d_{l\sigma_1}^{\dagger} d_{k\sigma_2}^{\dagger} d_{k\sigma_2} d_{l\sigma_1} \quad (3.24)$$

and

$$H_{lc} = -\tau \sum_{\sigma} (c_{1,L,\sigma}^{\dagger} d_{-N,\sigma} + d_{N,\sigma}^{\dagger} c_{1,R,\sigma} + h.c.), \quad (3.25)$$

we define the current operator J_j at an arbitrary site j (in the leads or in the interacting region) as

$$J_j = -i \sum_{\sigma} [\tau (a_{j\sigma}^{\dagger} a_{j+1\sigma} - a_{j+1\sigma}^{\dagger} a_{j\sigma})], \quad (3.26)$$

where a_j can either be c_j or d_j , depending on whether we are in the leads or in the central region of the QPC.

As one can easily check, these currents satisfy the continuity equation

$$\frac{d}{dt} \rho + \nabla J = 0 \Leftrightarrow -i[\rho, H] + \nabla J = 0, \quad (3.27)$$

i.e. in discrete terms $-i[a_{j\sigma}^{\dagger} a_{j\sigma}, H] + J_{j+1} - J_j = 0$.

Thus, the current operator simply counts the particles moving to the right and subtracts the number of particles moving to the left. This is also expressed in the straight forward relation $\dot{N}_j = -J_j$, where N_j is the particle number operator which counts all particles on sites to the left (including j) from site j .

After having established the current operator, we can specify the response of this operator to external perturbations³. In our case, we apply an external voltage difference between the left and the right lead. This induces an electric field in our QPC, which we can describe by a vector potential (ϕ_{ext}, A_{ext}) .⁴ We assume that this external potential

³We will follow here the derivation in the book of Bruus-Flensberg [15]

⁴Since our model is one dimensional, A_{ext} has only one component.

couples to our Hamiltonian in the usual way

$$H_{ext}(t) = -e \sum_{j,\sigma} n_{j,\sigma} \phi_{ext}(j) + e \sum_{j,\sigma} J_{j,\sigma} A_{ext,j}(t). \quad (3.28)$$

To make our life easier, we adopt a gauge where $\phi_{ext} = 0$ and thus end up with

$$H_{ext} = e \sum_{j,\sigma} J_{j\sigma} A_{ext,j}(t). \quad (3.29)$$

We can now compute the change in the expectation value of the current

$$\delta \langle J_{j\sigma} \rangle(t) := \langle J_{j\sigma} \rangle(t) - \langle J_{j\sigma}^{(H)}(t) \rangle_0, \quad (3.30)$$

where

$$\langle J_{j\sigma} \rangle(t) = \frac{1}{Z_0} \text{Tr}[\rho(t) J_{j\sigma}] \quad (3.31)$$

is the expectation value of $J_{j\sigma}$ at time t , calculated using the full Hamiltonian $H_{full} = H + H_{ext}$. We assume here, as usual, the system to be in equilibrium at $t = -\infty$:

$$\rho(-\infty) = e^{-\beta H} = \sum_n |n\rangle \langle n| e^{-\beta E_n} \quad (3.32)$$

and then get

$$\rho(t) = \sum_n |n(t)\rangle \langle n(t)| e^{-\beta E_n} \quad (3.33)$$

by letting the eigenstates $|n\rangle$ of the unperturbed Hamiltonian evolve in time using the full Hamiltonian

$$i\partial_t n(t) = H(t)|n(t)\rangle, \quad (3.34)$$

where H_{ext} is switched on at a certain time $t_0 \rightarrow \infty$. On the other hand, $\langle J_{j\sigma}^{(H)}(t) \rangle_0$ simply denotes the expectation value of the current operator in the Heisenberg picture using only the unperturbed Hamiltonian H and an usual equilibrium average $\langle \rangle_0$. Since $\langle J_{j\sigma}^{(H)}(t) \rangle_0 = 0$ in equilibrium, we have

$$\delta \langle J_{j\sigma} \rangle(t) = \langle J_{j\sigma} \rangle(t). \quad (3.35)$$

Due to the usual Kubo formula (see for example [11, chapter 2.1]), we get then for the response of the total current to an external potential

$$D_{J(j)J(l)}^R(t-t') := \frac{\delta \langle \sum_{\sigma} J_{j\sigma} \rangle(t)}{\delta (eA_{ext,l}(t'))} = -i\theta(t-t') \left\langle \left[\sum_{\sigma_1} J_{j\sigma_1}^{(H)}(t), \sum_{\sigma_2} J_{l\sigma_2}^{(H)}(t) \right] \right\rangle_0, \quad (3.36)$$

where $D_{J(j)J(l)}^R$ denotes the retarded current-current correlation function. Due to Maxwell's equation and our choice of gauge, we have $E(t) = -\partial_t A(t)$ and after a Fourier transformation $E(\omega) = i\omega A(\omega)$. Up to linear order in A_{ext} one gets

$$\langle J_j \rangle(t) = \sum_{\sigma} \langle J_{j\sigma} \rangle(t) = \sum_{\sigma} \delta \langle J_{j\sigma} \rangle(t) = \int_{-\infty}^{\infty} dt' D_{J(j)J(l)}^R(t-t') eA_{ext,l}(t'). \quad (3.37)$$

Using again Fourier transformation in t , the convolution on the r.h.s. becomes a simple product and we have

$$\langle J_j(\omega) \rangle = \sum_l D_{J(j)J(l)}^R(\omega) e A_{ext,l}(\omega) = \sum_l D_{J(j)J(l)}^R(\omega) e \frac{1}{i\omega} E_{ext,l}(\omega). \quad (3.38)$$

In the end, we will only be interested in the DC current, i.e. $\langle J_j(\omega \rightarrow 0) \rangle$. To proceed further, two important observations are in order:

1. We assume that after a while, when we have turned on the external voltage difference, the system will be in a steady state in the sense of $\langle \dot{\rho}(t) \rangle = 0$, i.e. $\langle \nabla J \rangle = 0$ and therefore $\langle J \rangle$ is constant in space. This is simply the statement that the DC current will be conserved, i.e. it does not matter whether we measure the current at site i or site j .
2. The second observation will be a bit trickier, namely we will show ⁵ that the retarded current-current correlation function in the DC-limit $D_{J(j)J(l)}^R(\omega \rightarrow 0)$ is in fact symmetric in j and l , i.e.

$$D_{J(j)J(l)}^R(\omega) = D_{J(l)J(j)}^R(\omega). \quad (3.39)$$

With this observations we can make an important conclusion. Since equation (3.38) does not depend on j (observation 1), $D_{J(j)J(l)}^R(\omega)$ is symmetric in j and l , and we are allowed to apply arbitrary external probes $A_{ext,l}(\omega)$, we must in fact have that $D_{J(j)J(l)}^R(\omega)$ does neither depend on j nor l . Therefore, it suffices to evaluate it at two points $j = j_1$, $l = l_1$ which we can choose to our convenience. In practice different choices of l and j will simply lead to different representations of the conductance in terms of the Green's functions. Equation (3.38) then yields

$$\langle J_j(\omega) \rangle = \frac{e}{i\omega} D_{J(j_1)J(l_1)}^R(\omega) \sum_l E_{ext,l}(\omega). \quad (3.40)$$

As said before, in our considerations we will only be interested in the DC conductance, i.e. the $\lim_{\omega \rightarrow 0} \langle J_j(\omega) \rangle$ case. We see from (3.40) that $\sum_l E_{ext,l}(0) = V$ is simply the voltage difference between our two leads. Since the electric current (due to electrons) is $I_e = -e \langle J_j \rangle$, we get in the DC case:

$$I_e = \lim_{\omega \rightarrow 0} \frac{ie^2}{\omega} D_{J(j_1)J(l_1)}^R(\omega) \cdot V \quad (3.41)$$

and therefore for the linear response conductance

$$G = \lim_{\omega \rightarrow 0} \frac{ie^2}{\omega} D_{J(j_1)J(l_1)}^R(\omega). \quad (3.42)$$

⁵This we will see a little bit later when we explicitly calculate $D_{J(j)J(l)}^R$.

Thus, our remaining task is to calculate

$$D_{J(j)J(l)}^R(\omega) = FT \left[-i\theta(t-t') \left\langle \sum_{\sigma_1} J_{j\sigma_1}^{(H)}(t), \sum_{\sigma_2} J_{l\sigma_2}^{(H)}(t') \right\rangle_0 \right]. \quad (3.43)$$

To accomplish this, we use a quite general statement about the connection between a retarded response function in real time

$$D_{AB}^R(t, t') = -i\theta(t-t') \langle A^{(H)}(t), B^{(H)}(t') \rangle \quad (3.44)$$

and the thermal response function $D_{AB}(\tau, \tau')$ in imaginary time

$$D_{AB}(\tau, \tau') = -\langle T[A^{(H)}(\tau)B^{(H)}(\tau')] \rangle, \quad (3.45)$$

where $T[\]$ denotes the time ordered product (here in imaginary time). If we have time translational invariance, we have of course $D_{AB}^R(t, t') = D_{AB}^R(t-t')$ and $D_{AB}(\tau, \tau') = D_{AB}(\tau - \tau')$. A general argument using the spectral representation of the response functions shows (see for example [15, chapter 11]) that $D_{AB}^R(\omega)$ can be extracted from $D_{AB}(\omega_n)$ via analytic continuation from above. The frequencies ω_n denote here even or odd Matsubara frequencies, depending on the symmetry or antisymmetry of the operators A, B . Stated in formulas, this means

$$D_{AB}^R(\omega) = D_{AB}(\omega + i0^+). \quad (3.46)$$

Therefore, in our application we must calculate

$$D_{J(j)J(l)}(\tau) = -\left\langle T \left[\sum_{\sigma_1} J_{j\sigma_1}^{(H)}(\tau), \sum_{\sigma_2} J_{l\sigma_2}^{(H)}(0) \right] \right\rangle_0. \quad (3.47)$$

or in terms of frequencies

$$D_{J(j)J(l)}(\omega_n) = -\int_0^\beta d\tau e^{\omega_n \tau} \left\langle T \left[\sum_{\sigma_1} J_{j\sigma_1}^{(H)}(\tau), \sum_{\sigma_2} J_{l\sigma_2}^{(H)}(0) \right] \right\rangle_0, \quad (3.48)$$

where $\omega_n = i\frac{2n\pi}{\beta}$ denote even Matsubara frequencies.

At this point, it is a good time to stop for a moment and show the symmetry of $D_{J(j)J(l)}(\omega_n)$ or equivalently $D_{J(j)J(l)}^R(\omega)$ in $l \leftrightarrow j$ which we have stated before. Us-

ing the periodicity in β , one gets

$$\begin{aligned}
D_{J(j)J(l)}(\omega_n) &= - \int_0^\beta d\tau e^{\omega_n \tau} \left\langle T \left[\sum_{\sigma_1} J_{j\sigma_1}^{(H)}(\tau) \sum_{\sigma_2} J_{l\sigma_2}^{(H)}(0) \right] \right\rangle_0 \\
&= - \int_{-\beta}^0 d\tau e^{\omega_n \tau} \left\langle T \left[\sum_{\sigma_1} J_{j\sigma_1}^{(H)}(\tau) \sum_{\sigma_2} J_{l\sigma_2}^{(H)}(0) \right] \right\rangle_0 \\
&= - \int_{-\beta}^0 d\tau e^{\omega_n \tau} \theta(-\tau) \text{Tr} \left[e^{\beta(H-\mu N)} \sum_{\sigma_2} J_{l\sigma_2} e^{(H-\mu N)\tau} \sum_{\sigma_1} J_{j\sigma_1} e^{-(H-\mu N)\tau} \right] \\
&= - \int_{-\beta}^0 d\tau e^{\omega_n \tau} \left\langle T \left[\sum_{\sigma_2} J_{l\sigma_2}^{(H)}(-\tau) \sum_{\sigma_1} J_{j\sigma_1}^{(H)}(0) \right] \right\rangle_0 \\
&= - \int_0^\beta d\tau e^{-\omega_n \tau} \left\langle T \left[\sum_{\sigma_2} J_{l\sigma_2}^{(H)}(\tau) \sum_{\sigma_1} J_{j\sigma_1}^{(H)}(0) \right] \right\rangle_0 \\
&= D_{J(l)J(j)}(-\omega_n).
\end{aligned} \tag{3.49}$$

Therefore, we have in the DC case

$$D_{J(j)J(l)}(0) = D_{J(l)J(j)}(0). \tag{3.50}$$

After having shown the second observation, we can now explicitly calculate

$$\begin{aligned}
D_{J(j)J(l)}(\omega_n) &= - \int_0^\beta d\tau e^{\omega_n \tau} \left\langle T \left[\sum_{\sigma_1} J_{j\sigma_1}^{(H)}(\tau) \sum_{\sigma_2} J_{l\sigma_2}^{(H)}(0) \right] \right\rangle_0 \\
&= - \int_0^\beta d\tau e^{\omega_n \tau} \sum_{\sigma_1} \sum_{\sigma_2} \left\langle T \left[\left(a_{j,\sigma_1}^{\dagger(H)}(\tau) a_{j+1,\sigma_1}^{(H)}(\tau) - a_{j+1,\sigma_1}^{\dagger(H)}(\tau) a_{j,\sigma_1}^{(H)}(\tau) \right) (-i\tau) \right. \right. \\
&\quad \left. \left. \times \left(a_{l,\sigma_2}^{\dagger(H)}(0) a_{l+1,\sigma_2}^{(H)}(0) - a_{l+1,\sigma_2}^{\dagger(H)}(0) a_{l,\sigma_2}^{(H)}(0) \right) (-i\tau) \right] \right\rangle_0 \\
&= \tau^2 \int_0^\beta d\tau e^{\omega_n \tau} \sum_{\sigma_1, \sigma_2} \left\{ \left\langle T \left[a_{j,\sigma_1}^{\dagger(H)}(\tau) a_{j+1,\sigma_1}^{(H)}(\tau) a_{l,\sigma_2}^{\dagger(H)}(0) a_{l+1,\sigma_2}^{(H)}(0) \right] \right\rangle \right. \\
&\quad - \left\langle T \left[a_{j,\sigma_1}^{\dagger(H)}(\tau) a_{j+1,\sigma_1}^{(H)}(\tau) a_{l+1,\sigma_2}^{\dagger(H)}(0) a_{l,\sigma_2}^{(H)}(0) \right] \right\rangle_0 \\
&\quad - \left\langle T \left[a_{j+1,\sigma_1}^{\dagger(H)}(\tau) a_{j,\sigma_1}^{(H)}(\tau) a_{l,\sigma_2}^{\dagger(H)}(0) a_{l+1,\sigma_2}^{(H)}(0) \right] \right\rangle_0 \\
&\quad \left. + \left\langle T \left[a_{j+1,\sigma_1}^{\dagger(H)}(\tau) a_{j,\sigma_1}^{(H)}(\tau) a_{l+1,\sigma_2}^{\dagger(H)}(0) a_{l,\sigma_2}^{(H)}(0) \right] \right\rangle \right\}
\end{aligned} \tag{3.51}$$

and thus in terms of two particle Green's functions

$$\begin{aligned}
D_{J(j)J(l)}(\omega_n) &= -\tau^2 \int_0^\beta d\tau e^{\omega_n \tau} \sum_{\sigma_1, \sigma_2} \left\{ \mathcal{G}^{(2)}(j+1 \sigma_1 \tau, l+1 \sigma_2 0 | l \sigma_2 0, j \sigma_1 \tau) \right. \\
&\quad - \mathcal{G}^{(2)}(j+1 \sigma_1 \tau, l \sigma_2 0 | l+1 \sigma_2 0, j \sigma_1 \tau) \\
&\quad - \mathcal{G}^{(2)}(j \sigma_1 \tau, l+1 \sigma_2 0 | l \sigma_2 0, j+1 \sigma_1 \tau) \\
&\quad \left. + \mathcal{G}^{(2)}(j \sigma_1 \tau, l \sigma_2 0 | l+1 \sigma_2 0, j+1 \sigma_1 \tau) \right\}.
\end{aligned} \tag{3.52}$$

To evaluate this two-particle Green's functions, we divide them into the connected part $\mathcal{G}_c^{(2)}$ consisting of all diagrams in which all external legs are connected and the parts consisting of diagrams in which a pair of external legs each is connected. In obvious short notation:

$$\mathcal{G}^{(2)}(1, 2|1', 2') = \mathcal{G}_c^{(2)}(1, 2|1', 2') + \mathcal{G}_c^{(1)}(1|1')\mathcal{G}_c^{(1)}(2|2') - \mathcal{G}_c^{(1)}(1|2')\mathcal{G}_c^{(1)}(2|1'). \quad (3.53)$$

Let's first focus on the parts which consist of products of one-particle Green's functions. Moreover, in order to proceed further we will have to choose which currents $J(j)$, $J(l)$ we take to evaluate the current-current correlation function. Here we will follow a common approach (see [16, 13, 17]) and take J_L and J_R , where J_L is the current operator at the right end of the left lead and J_R the current operator at the left end of the right lead, respectively. Explicitly,

$$\begin{aligned} J_L &= -i \sum_{\sigma} [\tau (c_{L1\sigma}^{\dagger} d_{-N\sigma} - d_{-N\sigma}^{\dagger} c_{L1\sigma})] \\ J_R &= -i \sum_{\sigma} [\tau (d_{N\sigma}^{\dagger} c_{R1\sigma} - c_{R1\sigma}^{\dagger} d_{N\sigma})]. \end{aligned} \quad (3.54)$$

The one-particle product part reads then

$$\begin{aligned} K^{(1)}(\omega_n) &:= -\tau^2 \int_0^{\beta} d\tau e^{\omega_n \tau} \sum_{\sigma_1, \sigma_2} \{ \\ &\quad \mathcal{G}(j+1 \sigma_1 \tau | l \sigma_2 0) \mathcal{G}(l+1 \sigma_2 0 | j \sigma_1 \tau) - \mathcal{G}(j+1 \sigma_1 \tau | j \sigma_1 \tau) \mathcal{G}(l+1 \sigma_2 0 | l \sigma_2 0) \\ &\quad - \mathcal{G}(j+1 \sigma_1 \tau | l+1 \sigma_2 0) \mathcal{G}(l \sigma_2 0 | j \sigma_1 \tau) + \mathcal{G}(j+1 \sigma_1 \tau | j \sigma_1 \tau) \mathcal{G}(l \sigma_2 0 | l+1 \sigma_2 0) \\ &\quad - \mathcal{G}(j \sigma_1 \tau | l \sigma_2 0) \mathcal{G}(l+1 \sigma_2 0 | j+1 \sigma_1 \tau) + \mathcal{G}(j \sigma_1 \tau | j+1 \sigma_1 \tau) \mathcal{G}(l+1 \sigma_2 0 | l \sigma_2 0) \\ &\quad + \mathcal{G}(j \sigma_2 \tau | l+1 \sigma_2 0) \mathcal{G}(l \sigma_2 0 | j+1 \sigma_1 \tau) - \mathcal{G}(j \sigma_1 \tau | j+1 \sigma_1 \tau) \mathcal{G}(l \sigma_2 0 | l+1 \sigma_2 0) \}. \end{aligned} \quad (3.55)$$

We notice that the terms in which the Green's functions are evaluated at equal times do not depend on time at all. Therefore, since ω_n are even Matsubara frequencies, the Fourier transform of this terms is zero and thus they vanish in $K^{(1)}(\omega_n)$. We are then left with

$$\begin{aligned} K^{(1)}(\omega_n) &= -\tau^2 \int_0^{\beta} d\tau e^{\omega_n \tau} \sum_{\sigma} \{ \mathcal{G}(j+1 \sigma \tau | l \sigma 0) \mathcal{G}(l+1 \sigma 0 | j \sigma \tau) \\ &\quad - \mathcal{G}(j+1 \sigma \tau | l+1 \sigma 0) \mathcal{G}(l \sigma 0 | j \sigma \tau) \\ &\quad - \mathcal{G}(j \sigma \tau | l \sigma 0) \mathcal{G}(l+1 \sigma 0 | j+1 \sigma \tau) \\ &\quad + \mathcal{G}(j \sigma \tau | l+1 \sigma 0) \mathcal{G}(l \sigma 0 | j+1 \sigma \tau) \}, \end{aligned} \quad (3.56)$$

where we furthermore used that the one-particle Green's functions are diagonal in spin space for our system. And with our particular choice of the currents⁶

$$\begin{aligned} j+1 &= c, -N \\ j &= L, 1 \\ l+1 &= R, 1 \\ l &= c, N \end{aligned} \quad (3.57)$$

⁶The index " c, j " stands here for site j of the central region.

we get

$$\begin{aligned}
K^{(1)}(\omega_n) = & -\tau^2 \int_0^\beta d\tau e^{\omega_n \tau} \sum_\sigma \{ \mathcal{G}(c, -N \sigma \tau | c, N \sigma 0) \mathcal{G}(R, 1 \sigma 0 | L, 1 \sigma \tau) \\
& - \mathcal{G}(c, -N \sigma \tau | R, 1 \sigma 0) \mathcal{G}(c, N \sigma 0 | L, 1 \sigma \tau) \\
& - \mathcal{G}(L, 1 \sigma \tau | c, N \sigma 0) \mathcal{G}(R, 1 \sigma 0 | c, -N \sigma \tau) \\
& + \mathcal{G}(L, 1 \sigma \tau | R, 1 \sigma 0) \mathcal{G}(c, N \sigma 0 | c, -N \sigma \tau) \}. \tag{3.58}
\end{aligned}$$

For our ultimate goal, namely the calculation of the conductance G (3.42) we will have to perform the limit $\frac{K(\omega)}{\omega} \rightarrow 0$. Therefore, we will now work out the frequency dependence of $K^{(1)}(\omega_n)$. We have⁷

$$\begin{aligned}
K^{(1)}(\omega_n) = & -\tau^2 \int_0^\beta d\tau e^{\omega_n \tau} \sum_\sigma \left(\frac{1}{\beta} \right)^2 \sum_{\omega_1, \omega_2} e^{-(\omega_1 \tau - \omega_2 \tau)} \{ \\
& \mathcal{G}(c, -N \sigma | c, N \sigma)(\omega_1) \mathcal{G}(R, 1 \sigma | L, 1 \sigma)(\omega_2) \\
& - \mathcal{G}(c, -N \sigma | R, 1 \sigma)(\omega_1) \mathcal{G}(c, N \sigma | L, 1 \sigma)(\omega_2) \\
& - \mathcal{G}(L, 1 \sigma | c, N \sigma)(\omega_1) \mathcal{G}(R, 1 \sigma | c, -N \sigma)(\omega_2) \\
& + \mathcal{G}(L, 1 \sigma | R, 1 \sigma)(\omega_1) \mathcal{G}(c, N \sigma | c, -N \sigma)(\omega_2) \} \\
= & -\frac{1}{\beta^2} \tau^2 \sum_{\omega_1, \omega_2} \sum_\sigma \delta(\omega_n + \omega_2 - \omega_1) \{ \dots \} \\
= & -\frac{1}{\beta} \tau^2 \sum_{\omega_2} \sum_\sigma \{ \mathcal{G}(c, -N \sigma | c, N \sigma)(\omega_2 + \omega_n) \mathcal{G}(R, 1 \sigma | L, 1 \sigma)(\omega_2) \\
& - \mathcal{G}(c, -N \sigma | R, 1 \sigma)(\omega_2 + \omega_n) \mathcal{G}(c, N \sigma | L, 1 \sigma)(\omega_2) \\
& - \mathcal{G}(L, 1 \sigma | c, N \sigma)(\omega_2 + \omega_n) \mathcal{G}(R, 1 \sigma | c, -N \sigma)(\omega_2) \\
& + \mathcal{G}(L, 1 \sigma | R, 1 \sigma)(\omega_2 + \omega_n) \mathcal{G}(c, N \sigma | c, -N \sigma)(\omega_2) \}. \tag{3.59}
\end{aligned}$$

With our earlier derived formulas for the Green's functions $\mathcal{G}_{L,1j}(\omega)$ and $\mathcal{G}_{R,1j}(\omega)$ connecting the last site of the leads with an arbitrary index in the central region (3.13), we can rewrite this as

$$\begin{aligned}
K^{(1)}(\omega_n) = & -\frac{1}{\beta} \tau^2 \sum_{\omega'_n} \sum_\sigma \{ \mathcal{G}_{-N,N}^\sigma(\omega'_n + \omega_n) \mathcal{G}_{N,-N}^\sigma(\omega'_n) \tau^2 g_L^\sigma(\omega'_n) g_R^\sigma(\omega'_n) \\
& - \mathcal{G}_{-N,N}^\sigma(\omega'_n + \omega_n) \tau g_R^\sigma(\omega'_n + \omega_n) \mathcal{G}_{N,-N}^\sigma(\omega'_n) \tau g_L^\sigma(\omega'_n) \\
& - \mathcal{G}_{-N,N}^\sigma(\omega'_n + \omega_n) \tau g_L^\sigma(\omega'_n + \omega_n) \mathcal{G}_{N,-N}^\sigma(\omega'_n) \tau g_R^\sigma(\omega'_n) \\
& + \mathcal{G}_{-N,N}^\sigma(\omega'_n + \omega_n) \tau^2 g_L^\sigma(\omega'_n + \omega_n) g_R^\sigma(\omega'_n + \omega_n) \mathcal{G}_{N,-N}^\sigma(\omega'_n) \} \\
= & -\frac{1}{\beta} \tau^4 \sum_{\omega'_n} \sum_\sigma \mathcal{G}_{-N,N}^\sigma(\omega'_n + \omega_n) \mathcal{G}_{N,-N}^\sigma(\omega'_n) \\
& \{ g_L^\sigma(\omega'_n) g_R^\sigma(\omega'_n) - g_R^\sigma(\omega'_n + \omega_n) g_L^\sigma(\omega'_n) - g_L^\sigma(\omega'_n + \omega_n) g_R^\sigma(\omega'_n) \\
& + g_L^\sigma(\omega'_n + \omega_n) g_R^\sigma(\omega'_n + \omega_n) \}. \tag{3.60}
\end{aligned}$$

⁷ ω_1, ω_2 are now fermionic Matsubara frequencies

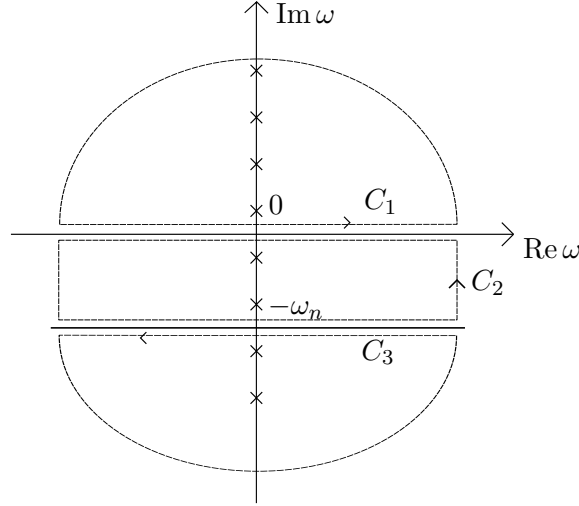


Figure 3.3.: Due to the two branch cuts at the real axis $\text{Im } \omega = 0$ and the axis $\text{Im } \omega = -\omega_n$, the complex plane is split into three regions. Since ω_n is an even Matsubara frequency, this second branch cut always lies in the middle between two odd Matsubara frequencies and thus we can evaluate the sum over the fermionic Matsubara frequencies (crosses on the imaginary axis) by computing the line integral over the shown paths $C_1 \cup C_2 \cup C_3$.

In our case $g_R^\sigma = g_L^\sigma =: g$ and with the definition

$$\lambda(\omega'_n, \omega'_n + \omega_n) = (g(\omega'_n) - g(\omega'_n + \omega_n))^2 \quad (3.61)$$

we get

$$K^{(1)}(\omega_n) = -\frac{1}{\beta} \tau^4 \sum_{\omega'_n} \sum_{\sigma} \mathcal{G}_{-N,N}^\sigma(\omega'_n + \omega_n) \mathcal{G}_{N,-N}^\sigma(\omega'_n) \lambda(\omega'_n, \omega'_n + \omega_n)^2. \quad (3.62)$$

To evaluate the sum over the odd Matsubara frequencies ω'_n we use the residue theorem and write sums of the form $\frac{1}{\beta} \sum_{\omega'_n} F(\omega'_n)$ as the complex contour integral $\frac{1}{2\pi i} \int dz F(z) f(z)$, where $f(z)$ is simply the Fermi function $f(z) = \frac{1}{e^{\beta z} + 1}$. Since the propagators have branch cuts at the real axis, we see that in order to calculate (3.62) we have to divide the complex frequency plane like shown in fig. 3.3.

Thus, we get

$$K(\omega_n) = -\tau^4 \frac{1}{2\pi i} \int d\omega f(\omega) F_{\omega_n}(\omega), \quad (3.63)$$

where $F_{\omega_n}(\omega)$ is given by equation (3.62). Since the products $\mathcal{G}_{-N,N}^\sigma(\omega'_n + \omega_n) \mathcal{G}_{N,-N}^\sigma(\omega'_n)$, $g^\sigma(\omega'_n)^2$, and $g^\sigma(\omega'_n)g^\sigma(\omega_n + \omega'_n)$ vanish like $\frac{1}{|\omega'_n|^2}$ for $|\omega'_n| \rightarrow \infty$, we can neglect the parts

of the arc contributions (by taking the arc radius to ∞) and finally end up with

$$\begin{aligned}
K^{(1)}(\omega_n) &= -\tau^4 \frac{1}{2\pi i} \int_{C_1 \cup C_2 \cup C_3} d\omega f(\omega) F(\omega) \\
&= -\frac{\tau^4}{2\pi i} \int_{-\infty}^{\infty} d\omega f(\omega) \sum_{\sigma} \left\{ \mathcal{G}_{-N,N}^{\sigma}(\omega + \omega_n + i\epsilon) \mathcal{G}_{N,-N}^{\sigma}(\omega + i\epsilon) \lambda(\omega + i\epsilon, \omega + i\epsilon + \omega_n)^2 \right. \\
&\quad - \mathcal{G}_{-N,N}^{\sigma}(\omega + \omega_n - i\epsilon) \mathcal{G}_{N,-N}^{\sigma}(\omega - i\epsilon) \lambda(\omega - i\epsilon, \omega - i\epsilon + \omega_n)^2 \\
&\quad + \mathcal{G}_{-N,N}^{\sigma}(\omega - \omega_n + i\epsilon + \omega_n) \mathcal{G}_{N,-N}^{\sigma}(\omega - \omega_n + i\epsilon) \lambda(\omega - \omega_n + i\epsilon, \omega + i\epsilon)^2 \\
&\quad \left. - \mathcal{G}_{-N,N}^{\sigma}(\omega - i\epsilon) \mathcal{G}_{N,-N}^{\sigma}(\omega - \omega_n - i\epsilon) \lambda(\omega - \omega_n - i\epsilon, \omega - i\epsilon)^2 \right\}.
\end{aligned} \tag{3.64}$$

To analyze now the behavior for $\omega_n \rightarrow 0$, we use (3.20)

$$g(z) = \frac{1}{2\tau^2} \begin{cases} z + \mu - i\sqrt{4\tau^2 - (z + \mu)^2}, & \text{for } \text{Im}(z) > 0 \\ z + \mu + i\sqrt{4\tau^2 - (z + \mu)^2}, & \text{for } \text{Im}(z) < 0 \end{cases} \tag{3.65}$$

Therefore, we have for $\delta > 0$ and $x \in \mathbb{R}$

$$\begin{aligned}
g(x \pm i\delta) &= \frac{1}{2\tau^2} \begin{cases} x + i\delta + \mu - i\sqrt{4\tau^2 - (x + i\delta + \mu)^2} \\ x - i\delta + \mu + i\sqrt{4\tau^2 - (x - i\delta + \mu)^2} \end{cases} \\
&= \frac{1}{2\tau^2} \begin{cases} x + \mu - i\sqrt{4\tau^2 - (x + \mu)^2} + O(\delta) \\ x + \mu + i\sqrt{4\tau^2 - (x + \mu)^2} + O(\delta) \end{cases}
\end{aligned} \tag{3.66}$$

Thus, we get for the λ s appearing in (3.64) and $\omega_n/i > 0$ ⁸

$$\begin{aligned}
\lambda(\omega + i\epsilon, \omega + i\epsilon + \omega_n)^2 &= (g(\omega + i\epsilon + i\omega_n) - g(\omega + i\epsilon))^2 \sim O(\omega_n^2) \\
\lambda(\omega - i\epsilon, \omega - i\epsilon + \omega_n)^2 &= (g(\omega - i\epsilon + \omega_n) - g(\omega - i\epsilon))^2 \\
&= \left(-\frac{i}{\tau^2} \sqrt{4\tau^2 - (\omega + \mu)^2} \right)^2 + O(\omega_n) \\
\lambda(\omega - \omega_n - i\epsilon, \omega - i\epsilon)^2 &= (g(\omega - i\epsilon) - g(\omega - \omega_n - i\epsilon))^2 \sim O(\omega_n^2).
\end{aligned} \tag{3.67}$$

Therefore,

$$\begin{aligned}
K^{(1)}(\omega_n) &= -\frac{\tau^4}{2\pi i} \int_{-\infty}^{\infty} d\omega f(\omega) \sum_{\sigma} \left\{ -\mathcal{G}_{-N,N}^{\sigma}(\omega + \omega_n - i\epsilon) \mathcal{G}_{N,-N}^{\sigma}(\omega - i\epsilon) \lambda(\omega - i\epsilon, \omega - i\epsilon + \omega_n)^2 \right. \\
&\quad \left. + \mathcal{G}_{-N,N}^{\sigma}(\omega + i\epsilon) \mathcal{G}_{N,-N}^{\sigma}(\omega - \omega_n + i\epsilon) \lambda(\omega - \omega_n + i\epsilon, \omega + i\epsilon)^2 + O(\omega_n^2) \right\}.
\end{aligned} \tag{3.68}$$

If we now perform the analytic continuation $\omega_n \rightarrow \Omega + i0^+$ (which is easy in the zero temperature case) and substitute $\omega \rightarrow \omega + \Omega$ in the second term, we can safely take the

⁸It suffices here to consider only the $\omega_n/i > 0$ case since we have to perform analytic continuation from above.

limit $\epsilon \rightarrow 0$ in the $0^+ \pm \epsilon$ terms and finally end up with

$$K^{(1)}(\Omega) = -\frac{\tau^4}{2\pi i} \int_{-\infty}^{\infty} d\omega (f(\omega) - f(\Omega + \omega)) \sum_{\sigma} \mathcal{G}_{-N,N}^{\sigma}(\omega + \Omega + i0^+) \mathcal{G}_{N,-N}^{\sigma}(\omega - i0^+) \times \lambda(\omega - i0^+, \omega + \Omega + i0^+)^2. \quad (3.69)$$

Using our formula (3.42) we thus get for the one-particle product part of the linear response conductance

$$\begin{aligned} G^{(1)} &= \lim_{\Omega \rightarrow 0} \frac{ie^2}{\Omega} K^{(1)}(\Omega) = \lim_{\Omega \rightarrow 0} \frac{\tau^4 e^2}{2\pi} \int_{-\infty}^{\infty} d\omega \frac{f(\Omega + \omega) - f(\omega)}{\Omega} \\ &\quad \sum_{\sigma} \mathcal{G}_{-N,N}^{\sigma}(\omega + \Omega + i0^+) \mathcal{G}_{N,-N}^{\sigma}(\omega - i0^+) \underbrace{\lambda(\omega - i0^+, \omega + \Omega + i0^+)^2}_{-\frac{1}{\tau^4}(4\tau^2 - (\omega + \mu)^2) + O(\Omega)} \\ &= -\frac{e^2}{2\pi} \int_{-\infty}^{\infty} d\omega f'(\omega) \sum_{\sigma} \mathcal{G}_{-N,N}^{\sigma}(\omega + i0^+) \mathcal{G}_{N,-N}^{\sigma}(\omega - i0^+) \cdot (4\tau^2 - (\omega + \mu)^2). \end{aligned} \quad (3.70)$$

Due to the general properties of Green's functions, we have for the retarded propagator $\mathcal{G}_{-N,N}^{\sigma}(\omega + i0^+) = \mathcal{G}_{-N,N}^{\sigma}(\omega - i0^+)^*$, i.e. it is the complex conjugate of the advanced one. Using the symmetry of our Hamiltonian, i.e. $H = H^T$, we furthermore get $\mathcal{G}_{-N,N}^{\sigma}(z) = \mathcal{G}_{N,-N}^{\sigma}(z)$ and thus (3.70) becomes

$$G^{(1)} = -\frac{e^2}{2\pi} \int_{-\infty}^{\infty} d\omega f'(\omega) \sum_{\sigma} |\mathcal{G}_{-N,N}^{\sigma}(\omega + i0^+)|^2 \cdot (4\tau^2 - (\omega + \mu)^2). \quad (3.71)$$

A similar analysis can be done for the part of the conductance which arises from the contributions of the connected two-particle parts of the correlation function in the splitting (3.53). Going back to equation (3.52) and using that the two-particle (and one-particle irreducible) vertex γ_2 is simply the two-particle connected Green's function with amputated legs⁹ (see for example [11, chapter 2.4])

$$\begin{aligned} &\mathcal{G}_c^{(2)}(\alpha_1 \beta_1, \alpha_2 \beta_2 | \alpha'_1 \beta'_1, \alpha'_2 \beta'_2) = \\ &\quad - \sum_{\alpha_3 \alpha_4 \alpha'_3 \alpha'_4} \int_0^{\beta} d\tau_3 d\tau_4 d\tau'_3 d\tau'_4 \mathcal{G}_c^{(1)}(\alpha_1 \beta_1 | \alpha_3 \tau_3) \mathcal{G}_c^{(1)}(\alpha_2 \beta_2 | \alpha_4 \tau_4) \\ &\quad \times \gamma_2(\alpha_3 \tau_3, \alpha_4 \tau_4 | \alpha'_3 \tau'_3, \alpha'_4 \tau'_4) \mathcal{G}_c^{(1)}(\alpha'_3 \tau'_3 | \alpha'_1 \beta'_1) \mathcal{G}_c^{(1)}(\alpha'_4 \tau'_4 | \alpha'_2 \beta'_2), \end{aligned} \quad (3.72)$$

or in frequency space

$$\begin{aligned} &\mathcal{G}_c^{(2)}(\alpha_1 \beta_1, \alpha_2 \beta_2 | \alpha'_1 \beta'_1, \alpha'_2 \beta'_2) = - \sum_{\alpha_3 \alpha_4 \alpha'_3 \alpha'_4} \left(\frac{1}{\beta}\right)^4 \sum_{\omega_1 \omega_2 \omega'_1 \omega'_2} \delta(\omega_1 + \omega_2 - \omega'_1 - \omega'_2) \\ &\quad \times e^{-(\omega_1 \beta_1 + \omega_2 \beta_2 - \omega'_1 \beta'_1 - \omega'_2 \beta'_2)} \\ &\quad \times \mathcal{G}(\alpha_1, \alpha_3; \omega_1) \mathcal{G}(\alpha_2, \alpha_4; \omega_2) \gamma_2(\alpha_3 \omega_1, \alpha_4 \omega_2 | \alpha'_3 \omega'_1, \alpha'_4 \omega'_2) \mathcal{G}(\alpha'_3, \alpha'_1; \omega'_1) \mathcal{G}(\alpha'_4, \alpha'_2; \omega'_2) \end{aligned} \quad (3.73)$$

⁹where the β 's are imaginary time indices and $\alpha = j, \sigma$ labels site and spin.

we obtain

$$\begin{aligned}
K^{(2)}(\omega_n) = & \tau^2 \sum_{\sigma} \left(\frac{1}{\beta}\right)^3 \sum_{\alpha_3 \alpha_4 \alpha'_3 \alpha'_4} \sum_{\omega_1 \omega_2} \{ \mathcal{G}(j+1 \sigma, \alpha_3; \omega_1 + \omega_n) \mathcal{G}(l+1 \sigma, \alpha_4; \omega_2) \\
& \times \gamma_2(\alpha_3(\omega_1 + \omega_n), \alpha_4 \omega_2 | \alpha_3(\omega_2 + \omega_n), \alpha'_4 \omega_1) \mathcal{G}(\alpha'_3, l \sigma; \omega_2 + \omega_n) \mathcal{G}(\alpha'_4, j \sigma; \omega_1) \\
& - \mathcal{G}(j+1 \sigma, \alpha_3; \omega_1 + \omega_n) \mathcal{G}(l \sigma, \alpha_4; \omega_2) \gamma_2(\alpha_3(\omega_1 + \omega_n), \alpha_4 \omega_2 | \alpha_3(\omega_2 + \omega_n), \alpha'_4 \omega_1) \\
& \times \mathcal{G}(\alpha'_3, l+1 \sigma; \omega_2 + \omega_n) \mathcal{G}(\alpha'_4, j \sigma; \omega_2) \\
& - \mathcal{G}(j \sigma, \alpha_3; \omega_1 + \omega_n) \mathcal{G}(l+1 \sigma, \alpha_4; \omega_2) \gamma_2(\alpha_3(\omega_1 + \omega_n), \alpha_4 \omega_2 | \alpha_3(\omega_2 + \omega_n), \alpha'_4 \omega_1) \\
& \times \mathcal{G}(\alpha'_3, l \sigma; \omega_2 + \omega_n) \mathcal{G}(\alpha'_4, j+1 \sigma; \omega_2) \\
& + \mathcal{G}(j \sigma, \alpha_3; \omega_1 + \omega_n) \mathcal{G}(l \sigma, \alpha_4; \omega_2) \gamma_2(\alpha_3(\omega_1 + \omega_n), \alpha_4 \omega_2 | \alpha_3(\omega_2 + \omega_n), \alpha'_4 \omega_1) \\
& \times \mathcal{G}(\alpha'_3, l+1 \sigma; \omega_2 + \omega_n) \mathcal{G}(\alpha'_4, j+1 \sigma; \omega_2) \}.
\end{aligned} \tag{3.74}$$

The trick is now that in our later on adopted approximation scheme the two-particle vertex γ_2 does not depend on the frequency at all (except for frequency conservation, of course). Thus, it can be taken out of the sums and the dependence of the remaining structure on ω_n can be analyzed as in the one-particle product case. Since this is completely analogous to what we have done above, we simply state here the result, namely¹⁰

$$K^{(2)}(\omega_n) \sim O(\omega_n^2). \tag{3.75}$$

Therefore, due to the limit $\lim_{\omega \rightarrow 0} \frac{K(\omega)}{\omega}$, which is taken in (3.42), the two-particle part in the conductance $G^{(2)}$ is zero. At the end of the day, we remain with the formula for the conductance

$$G = -G_Q \cdot \frac{1}{2} \int_{-\infty}^{\infty} d\omega f'(\omega) [4\tau^2 - (\omega + \mu)^2] \cdot \sum_{\sigma} |\mathcal{G}_{-N,N}^{\sigma}(\omega + i0^+)|^2, \tag{3.76}$$

which was here rewritten in terms of the Conductance quantum $\frac{2e^2}{h} = G_Q$ and reintroducing the appropriate powers of \hbar . At this point, we remind ourselves that a possible Zeeman term induced through a external magnetic field was absorbed into the chemical potential and would lead to a shift of the bare μ , according to $\mu \rightarrow \mu + \frac{\sigma}{2} B$.

3.5. The density

The density of electrons can easily be calculated, using

$$\begin{aligned}
n_j^{\sigma} = & \langle a_{j\sigma}^{\dagger} a_{j\sigma} \rangle = \langle T[a_{j\sigma}^{\dagger(H)}(\tau + i0^+) a_{j\sigma}^{(H)}(\tau)] \rangle = -\langle T[a_{j\sigma}^{(H)}(\tau) a_{j\sigma}^{\dagger(H)}(\tau + i0^+)] \rangle \\
= & \mathcal{G}_{jj}^{\sigma}(\tau, \tau + i0^+) = \frac{1}{\beta} \sum_{\omega_n} e^{\omega_n 0^+} \mathcal{G}_{jj}^{\sigma}(\omega_n),
\end{aligned} \tag{3.77}$$

where $\omega_n = i \frac{(2n+1)\pi}{\beta}$ are as usual the odd Matsubara frequencies. The sum in (3.77) over the Matsubara frequencies can be evaluated via the residue theorem, transforming the sum in a contour integral, as seen in Fig. 3.4

¹⁰The interested reader can find a complete calculation in [13].

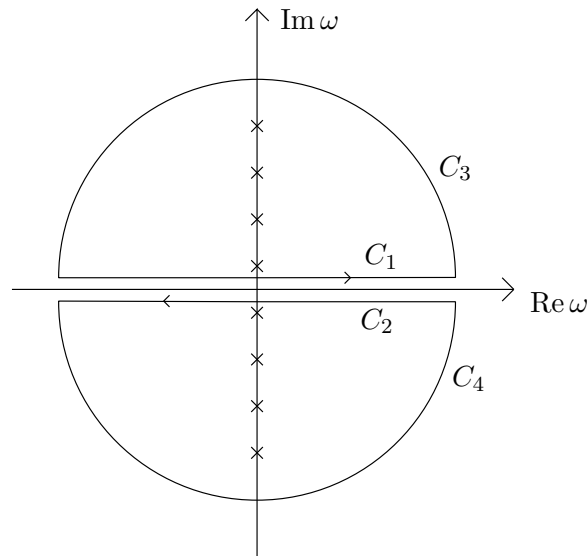


Figure 3.4.: The summation over fermionic Matsubara frequencies (crosses on the imaginary axis) is equivalent to the evaluation of the line integral over the shown paths $C =: C_1 \cup C_2 \cup C_3 \cup C_4$.

where the real axis is not in the interior of the integration paths since \mathcal{G}_{jj}^σ has a branch cut there. Thus, we get

$$n_j^\sigma = \frac{1}{\beta} \sum_{\omega_n} e^{\omega_n 0^+} \mathcal{G}_{jj}^\sigma(\omega_n) = -\frac{1}{2\pi i} \int_C d\omega e^{\omega 0^+} \mathcal{G}_{jj}^\sigma(\omega) f(\omega), \quad (3.78)$$

where $f(\omega) = \frac{1}{e^{\beta\omega} + 1}$ is again the Fermi function which has simple poles at the odd Matsubara frequencies with residues $-\frac{1}{\beta}$. Furthermore the line integrals over the arcs go to zero if we let their radius go to infinity, since

$$\frac{e^{\omega 0^+}}{e^{\beta\omega} + 1} \sim e^{\omega(0^+ - \beta)} \xrightarrow{\text{exponentially}} 0 \quad (3.79)$$

and

$$\frac{e^{\omega 0^+}}{e^{\beta\omega} + 1} \xrightarrow{\text{exponentially}} 0, \quad (3.80)$$

if we let $\text{Re}(\omega) \rightarrow \infty$ or $\text{Re}(\omega) \rightarrow -\infty$, respectively. Thus, according to fig. 3.4 we end

up with

$$\begin{aligned}
n_j^\sigma &= -\frac{1}{2\pi i} \int_{-\infty}^{\infty} d\omega \left[e^{(\omega+i0^+)0^+} \mathcal{G}_{jj}^\sigma(\omega+i0^+) f(\omega+i0^+) - e^{(\omega-i0^+)0^+} \mathcal{G}_{jj}^\sigma(\omega-i0^+) f(\omega-i0^+) \right] \\
&= -\frac{1}{2\pi i} \int_{-\infty}^{\infty} d\omega f(\omega) \left[\underbrace{\mathcal{G}_{jj}^\sigma(\omega+i0^+) - \mathcal{G}_{jj}^\sigma(\omega-i0^+)}_{\mathcal{G}_{jj}^{R\sigma}(\omega) - \mathcal{G}_{jj}^{A\sigma}(\omega) \stackrel{\omega \text{ real}}{=} \mathcal{G}_{jj}^{R\sigma}(\omega) - \mathcal{G}_{jj}^{R\sigma*}(\omega)} \right] \\
&= -\frac{1}{2\pi i} \int_{-\infty}^{\infty} d\omega f(\omega) 2i \operatorname{Im}[\mathcal{G}_{jj}^{R\sigma}(\omega)] = \int_{-\infty}^{\infty} d\omega f(\omega) \left[-\frac{1}{\pi} \operatorname{Im}[\mathcal{G}_{jj}^{R\sigma}(\omega)] \right] = \\
&= \int_{-\infty}^{\infty} f(\omega) \mathcal{A}_j(\omega),
\end{aligned} \tag{3.81}$$

where

$$\mathcal{A}_j^\sigma(\omega) := -\frac{1}{\pi} \operatorname{Im} \mathcal{G}_{jj}^{R\sigma}(\omega) = -\frac{1}{\pi} \operatorname{Im} \mathcal{G}_{jj}^\sigma(\omega+i0^+) \tag{3.82}$$

is the local density of states. In the second line of the above calculation, we have dropped the convergence factors, since the difference $\mathcal{G}_{jj}^\sigma(\omega+i0^+) - \mathcal{G}_{jj}^\sigma(\omega-i0^+)$ is proportional to $\frac{1}{\omega^2}$ if $|\omega| \rightarrow \infty$.

In principle, we could use now formula (3.81) to compute the electron density. However, since $\mathcal{A}_j(\omega) = -\frac{1}{\pi} \operatorname{Im} \mathcal{G}_{jj}^{R\sigma}(\omega)$ has its poles infinitesimally near the real axis it would be numerically very hard to perform the frequency integral along that axis. Therefore, we use here a slightly different approach. We start again from

$$\begin{aligned}
n_j^\sigma &= \frac{1}{\beta} \sum_{\omega_n} e^{\omega_n 0^+} \mathcal{G}_{jj}^\sigma(\omega_n) = -\frac{1}{2\pi i} \int_C d\omega e^{\omega 0^+} \mathcal{G}_{jj}^\sigma(\omega) f(\omega) = \\
&\quad -\frac{1}{2\pi i} \int_{C_1 \cup C_2} d\omega e^{\omega 0^+} \mathcal{G}_{jj}^\sigma(\omega) f(\omega) - \frac{1}{2\pi i} \int_{C_3 \cup C_4} d\omega e^{\omega 0^+} \mathcal{G}_{jj}^\sigma(\omega) f(\omega),
\end{aligned} \tag{3.83}$$

where we have split the line integral in the contributions C_1, C_2 along the real axis and the arc contributions C_3, C_4 . Above we have seen that for the first integral the convergence factor is meaningless, however, it is important for the second term in the limit of the arc radius going to infinity. If one calculates the second integral without the convergence factor, one obtains

$$-\frac{1}{2\pi i} \int_{C_3 \cup C_4} d\omega \mathcal{G}_{jj}^\sigma(\omega) f(\omega) = -\frac{1}{2\pi i} \int_{C_3 \cup C_4} d\omega \frac{1}{e^{\beta\omega} + 1} \mathcal{G}_{jj}^\sigma(\omega). \tag{3.84}$$

For the arc contribution where $\operatorname{Re} \omega \rightarrow +\infty$ the integral is zero, but for the contribution

with $\text{Re } \omega \rightarrow -\infty$ we get a finite value¹¹

$$\begin{aligned}
& -\frac{1}{2\pi i} \int_{C'_3 \cup C'_4} d\omega \frac{1}{e^{\beta\omega} + 1} \cdot \frac{1}{\omega} = -\frac{1}{2\pi i} \lim_{R \rightarrow \infty} \int_{\frac{\pi}{2}}^{\frac{3}{2}\pi} d\phi \frac{1}{e^{\beta R e^{i\phi}} + 1} \cdot \frac{1}{R e^{i\phi}} \cdot i R e^{i\phi} = \\
& -\frac{1}{2\pi i} \lim_{R \rightarrow \infty} \int_{\frac{\pi}{2}}^{\frac{3}{2}\pi} d\phi \frac{i}{e^{\beta R e^{i\phi}} + 1} \stackrel{\text{maj. Conv.}}{=} -\frac{1}{2\pi} \int_{\frac{\pi}{2}}^{\frac{3}{2}\pi} d\phi \lim_{R \rightarrow \infty} \frac{1}{e^{\beta R e^{i\phi}} + 1} = \\
& -\frac{1}{2\pi} \int_{\frac{\pi}{2}}^{\frac{3}{2}\pi} d\phi 1 = -\frac{1}{2},
\end{aligned} \tag{3.85}$$

where we used again that $\mathcal{G}_{jj}^\sigma(\omega) \sim \frac{1}{\omega}$ for $|\omega| \rightarrow \infty$. Therefore, we have for the density

$$\begin{aligned}
n_j^\sigma &= -\frac{1}{2\pi i} \int_{C_1 \cup C_2} d\omega \mathcal{G}_{jj}^\sigma(\omega) f(\omega) - \frac{1}{2\pi i} \int_{C_3 \cup C_4} d\omega \mathcal{G}_{jj}^\sigma(\omega) f(\omega) + \frac{1}{2} = \\
& \frac{1}{\beta} \sum_{\omega_n} \mathcal{G}_{jj}^\sigma(\omega_n) + \frac{1}{2} = \frac{1}{\beta} \left[\sum_{\omega_n > 0} \mathcal{G}_{jj}^{R\sigma}(\omega_n) + \sum_{\omega_n < 0} \underbrace{\mathcal{G}_{jj}^{A\sigma}(\omega_n)}_{=[\mathcal{G}_{jj}^{R\sigma}(-\omega_n)]^*} \right] + \frac{1}{2} = \\
& \frac{1}{\beta} \sum_{\text{Im}(\omega_n) > 0} 2 \text{Re } \mathcal{G}_{jj}^{R\sigma}(\omega_n) + \frac{1}{2}.
\end{aligned} \tag{3.86}$$

In our work, we will exclusively consider the zero temperature limit, i.e. the case $\beta \rightarrow \infty$. For this case, the summation $\frac{1}{\beta} \sum_{\omega_n}$ becomes an integral over frequencies $\frac{1}{2\pi} \int d\omega$ and we end up with

$$n_j^\sigma = \frac{1}{\pi} \int_0^\infty d\omega \text{Re } \mathcal{G}_{jj}^{R\sigma}(i\omega) + \frac{1}{2}. \tag{3.87}$$

For numerical computations we use this with the variable transformation $\omega = \frac{x}{1-x}$ and get

$$n_j^\sigma = \frac{1}{\pi} \int_0^1 \frac{dx}{(1-x)^2} \text{Re} \left[\mathcal{G}_{jj}^R \left(i \frac{x}{1-x} \right) \right] + \frac{1}{2}. \tag{3.88}$$

3.6. The susceptibility

Another important physical quantity of our system is the response of the magnetization to a variation of the external magnetic field, i.e. the magnetic susceptibility. Per site we get here

$$X_i = \partial_B m_i |_{B=0} = \frac{1}{2} \partial_B (n_i^\uparrow - n_i^\downarrow) |_{B=0}. \tag{3.89}$$

In principle, we have two ways to determine the magnetic susceptibility. Possibility one is to take a simple "numerical" derivative via

$$X_i \approx \frac{1}{2} \frac{(n_i^\uparrow - n_i^\downarrow)(\Delta B) - (n_i^\uparrow - n_i^\downarrow)(0)}{\Delta B} \tag{3.90}$$

¹¹We denote the parts of the arcs with $\text{Re}(\omega) < 0$ as C'_3 and C'_4 , respectively.

for a small magnetic field ΔB . This is the numerically cheapest method and we used this to generate most of our susceptibility plots.

The second possibility is to use again the Kubo formalism (as in our calculation of the conductance) to determine the response of the magnetization to a change in the magnetic field. However, our fRG approach grants us here a very elegant way to get our hands on the Kubo susceptibility. For this, we observe the following

$$X_j = \frac{1}{2} \partial_B (n_j^\uparrow - n_j^\downarrow)|_{B=0} = \frac{1}{2} \partial_B \sum_\sigma \sigma \left(\frac{1}{\beta} \sum_{\omega_n} \mathcal{G}_{jj}^{R\sigma}(\omega_n) + \frac{1}{2} \right) = \frac{1}{2\beta} \sum_{\sigma, \omega_n} \sigma \partial_B \mathcal{G}_{jj}^{R\sigma}(\omega_n) \quad (3.91)$$

and since

$$\mathcal{G}_{jj}^{R\sigma}(\omega_n) = \left[\frac{1}{\omega_n + \sigma \frac{B}{2} - \Sigma^\sigma(\omega_n) - H} \right]_{jj} \quad (3.92)$$

the derivative yields

$$\begin{aligned} \partial_B \mathcal{G}_{jj}^{R\sigma}(\omega_n) &= -\mathcal{G}_{j\alpha}^{R\sigma}(\omega_n) \partial_B \left[\omega_n + \sigma \frac{B}{2} - \Sigma^\sigma(\omega_n) - H \right]_{\alpha\beta} \mathcal{G}_{\beta j}^{R\sigma}(\omega_n) \\ &= -\mathcal{G}_{j\alpha}^{R\sigma}(\omega_n) \left[\frac{\sigma}{2} - \partial_B \Sigma^\sigma(\omega_n) \right]_{\alpha\beta} \mathcal{G}_{\beta j}^{R\sigma}(\omega_n). \end{aligned} \quad (3.93)$$

Plugging everything together, we get

$$X_j = -\frac{1}{2\beta} \sum_{\sigma, \omega_n} \mathcal{G}_{j\alpha}^{R\sigma}(\omega_n) \left[\frac{1}{2} - \sigma \partial_B \Sigma^\sigma(\omega_n) \right]_{\alpha\beta} \mathcal{G}_{\beta j}^{R\sigma}(\omega_n), \quad (3.94)$$

where the internal summation indices α and β run over all sites, including the leads.

The trick is now to consider a fRG flow with magnetic field B as flow parameter instead of the usual frequency cutoff. If we look then at the flow equation of the self energy (2.38) and insert there our new single scale propagator

$$S^{\sigma, B=0} = \mathcal{G} \partial_B [\mathcal{G}_0^\sigma]_{B=0}^{-1} \mathcal{G} = \frac{\sigma}{2} \mathcal{G}^2 \quad (3.95)$$

we end up with

$$\partial_B \Sigma_{kl}^\sigma(\omega_n) = -\frac{T}{2} \sum_{n', j_1, j_2, j_3, \sigma'} \sigma' \mathcal{G}_{j_1 j_2}^{\sigma'}(\omega'_n) \mathcal{G}_{j_2 j_3}^{\sigma'}(\omega'_n) \gamma_2(j_3 \sigma' \omega'_n, k \sigma \omega_n; j_1 \sigma' \omega'_n, l \sigma \omega_n). \quad (3.96)$$

And thus, we arrive at the Kubo formula for the magnetic susceptibility (cf. [18, chapter 3])

$$\begin{aligned} X_j &= -\frac{T}{4} \sum_{\sigma, \omega_n} \mathcal{G}_{jk}^{R\sigma}(\omega_n) \mathcal{G}_{kj}^{R\sigma}(\omega_n) - \frac{T}{4} \sum_{\sigma, \omega_n} \mathcal{G}_{j\alpha_1}^{R\sigma}(\omega_n) \mathcal{G}_{\alpha_1 j}^{R\sigma}(\omega_n) \\ &\quad - \frac{1}{2\beta} \sum_{\sigma, \omega_n} \sigma \mathcal{G}_{jk}^{R\sigma}(\omega_n) \frac{T}{2} \sum_{n', j_1, j_2, j_3, \sigma'} \sigma' \mathcal{G}_{j_1 j_2}^{\sigma'}(\omega'_n) \mathcal{G}_{j_2 j_3}^{\sigma'}(\omega'_n) \\ &\quad \times \gamma_2(j_3 \sigma' \omega'_n, k \sigma \omega_n; j_1 \sigma' \omega'_n, l \sigma \omega_n) \mathcal{G}_{lj}^{R\sigma}(\omega_n), \end{aligned} \quad (3.97)$$

where we have split the summation over site indices into two terms: In the first term the summation index k runs over the central region, whereas the index α_l in the second term runs exclusively over the leads. In fact, we can use in the second term our relations (3.13) to obtain

$$\begin{aligned} \sum_{\alpha_l} \mathcal{G}_{j\alpha_l}^{R\sigma}(\omega_n) \mathcal{G}_{\alpha_l j}^{R\sigma}(\omega_n) &= \sum_{\alpha=1}^{\infty} \left(\mathcal{G}_{j-N}^{R\sigma}(\omega_n) \tau^2 g_{1\alpha} \mathcal{G}_{-N j}^{R\sigma}(\omega_n) g_{\alpha 1} + \mathcal{G}_{j N}^{R\sigma}(\omega_n) \tau^2 g_{1\alpha} \mathcal{G}_{N j}^{R\sigma}(\omega_n) g_{\alpha 1} \right) \\ &= \tau^2 h \left(\mathcal{G}_{j-N}^{R\sigma}(\omega_n) \mathcal{G}_{-N j}^{R\sigma}(\omega_n) + \mathcal{G}_{j N}^{R\sigma}(\omega_n) \mathcal{G}_{N j}^{R\sigma}(\omega_n) \right), \end{aligned} \quad (3.98)$$

where we have defined h as the one-one element of the squared lead propagator

$$h := [g^2]_{11} = \sum_{\alpha=1}^{\infty} g_{1\alpha} g_{\alpha 1}. \quad (3.99)$$

In fact, h can be calculated analytically, as was done, for example, in [19] and one obtains

$$h(\omega_n) = \frac{1}{2\tau^2} \left(\frac{\omega_n + \mu}{\omega_n + \mu - 2\tau} \sqrt{\frac{\omega_n + \mu - 2\tau}{\omega_n + \mu + 2\tau}} - 1 \right). \quad (3.100)$$

The complete formula in terms of the numerical quantities introduced in the next chapter, including our approximation schemes for the calculation of the γ_2 vertex via the fRG flow, can be found in the appendix A.

4. Approximative treatment of longer ranged feedback

In this chapter, we will finally apply the general fRG technique introduced in chapter 2 to our problem at hand. The approach we choose here, is to first set up the concrete fRG equations for our system with a full feedback, i.e. correct in the sense of the equations 2.39 without additional approximation. In this form the flow equations have a very simple structure which we use to explain the coupled ladder approximation (CLA) (which in this context introduces only an approximation in frequency space but is still correct in the space indices). Furthermore, we will use this simple form to identify various symmetries in our flow equations. In the sections 4.6 and 4.7 we will then transform these symmetries and equations into a basis more suited for numerical calculations. In this basis, the symmetries and equations will look more difficult but it will be obvious how we can change from the full feedback to an approximate one using the CLA. At the end of this chapter, we will briefly comment on the actual numerical form of our quantities.

4.1. The bare vertex

Having established the general fRG equations and keeping in mind our desired observables, we are now at the point to specify the concrete form of the interaction and apply various approximations to end up at a numerical differential equation which can be implemented on a computer. On the specific form of the interaction strength we will elaborate at a later point. Here, it is sufficient to assume the general form of the bare vertex as

$$\begin{aligned} \nu(j_1 \sigma_1, j_2 \sigma_2; j_3 \sigma_3, j_4 \sigma_4) = & \underbrace{U_{j_1} \delta_{j_1 j_2} \delta_{j_3 j_4} \delta_{j_4 j_1} \delta_{\sigma_1 \bar{\sigma}_2} \delta_{\sigma_3 \bar{\sigma}_4} (\delta_{\sigma_1 \sigma_3} - \delta_{\sigma_1 \sigma_4})}_{=:\nu_1} \\ & + \underbrace{U_{j_1 j_2} (\delta_{j_1 j_3} \delta_{\sigma_1 \sigma_3} \delta_{j_2 j_4} \delta_{\sigma_2 \sigma_4} - \delta_{j_1 j_4} \delta_{j_2 j_3} \delta_{\sigma_1 \sigma_4} \delta_{\sigma_2 \sigma_3}) (1 - \delta_{j_1 j_2})}_{=:\nu_2}, \end{aligned} \quad (4.1)$$

where ν_1 represents the on-site and ν_2 the off-site interaction. Of course, we could write this in a more compact notation

$$\begin{aligned} \nu(j_1 \sigma_1, j_2 \sigma_2; j_3 \sigma_3, j_4 \sigma_4) = & \underbrace{[U_{j_1 j_2} (1 - \delta_{j_1 j_2}) + U_{j_1} \delta_{j_1 j_2} \delta_{\sigma_1 \bar{\sigma}_2}]}_{=:\tilde{U}_{j_1 j_2}} \\ & \times (\delta_{j_1 j_3} \delta_{\sigma_1 \sigma_3} \delta_{j_2 j_4} \delta_{\sigma_2 \sigma_4} - \delta_{j_1 j_4} \delta_{j_2 j_3} \delta_{\sigma_1 \sigma_4} \delta_{\sigma_2 \sigma_3}), \end{aligned} \quad (4.2)$$

however, we will in several occasions explicitly distinguish between on-site and off-site interactions and thus (4.1) is more handy.

We assume the interaction to be symmetric in the site indices, i.e. $U_{j_1 j_2} = U_{j_2 j_1}$, and therefore have the following symmetries for ν_2 :

$$\begin{aligned}
\nu_2(j_3 \sigma_3, j_4 \sigma_4; j_1 \sigma_1, j_2 \sigma_2) &= \nu_2(j_1 \sigma_1, j_2 \sigma_2; j_3 \sigma_3, j_4 \sigma_4) \\
\nu_2(j_3 \sigma_1, j_4 \sigma_2; j_1 \sigma_3, j_2 \sigma_4) &= \nu_2(j_1 \sigma_1, j_2 \sigma_2; j_3 \sigma_3, j_4 \sigma_4) \\
\nu_2(j_1 \sigma_3, j_2 \sigma_4; j_3 \sigma_1, j_4 \sigma_2) &= \nu_2(j_1 \sigma_1, j_2 \sigma_2; j_3 \sigma_3, j_4 \sigma_4) \\
\nu_2(j_2 \sigma_2, j_1 \sigma_1; j_3 \sigma_3, j_4 \sigma_4) &= -\nu_2(j_1 \sigma_1, j_2 \sigma_2; j_3 \sigma_3, j_4 \sigma_4) \\
\nu_2(j_1 \sigma_1, j_2 \sigma_2; j_4 \sigma_4, j_3 \sigma_3) &= -\nu_2(j_1 \sigma_1, j_2 \sigma_2; j_3 \sigma_3, j_4 \sigma_4) \\
\nu_2(j_1 \sigma_2, j_2 \sigma_1; j_3 \sigma_4, j_4 \sigma_3) &= \nu_2(j_1 \sigma_1, j_2 \sigma_2; j_3 \sigma_3, j_4 \sigma_4).
\end{aligned} \tag{4.3}$$

For ν_1 we get the symmetries

$$\begin{aligned}
\nu_1(j_3 \sigma_3, j_4 \sigma_4; j_1 \sigma_1, j_2 \sigma_2) &= \nu_1(j_1 \sigma_1, j_2 \sigma_2; j_3 \sigma_3, j_4 \sigma_4) \\
\nu_1(j_2 \sigma_2, j_1 \sigma_1; j_3 \sigma_3, j_4 \sigma_4) &= -\nu_1(j_1 \sigma_1, j_2 \sigma_2; j_3 \sigma_3, j_4 \sigma_4) \\
\nu_1(j_1 \sigma_1, j_2 \sigma_2; j_4 \sigma_4, j_3 \sigma_3) &= -\nu_1(j_1 \sigma_1, j_2 \sigma_2; j_3 \sigma_3, j_4 \sigma_4).
\end{aligned} \tag{4.4}$$

And thus we have as symmetries of the bare vertex:

$$\begin{aligned}
\nu(j_3 \sigma_3, j_4 \sigma_4; j_1 \sigma_1, j_2 \sigma_2) &= \nu(j_1 \sigma_1, j_2 \sigma_2; j_3 \sigma_3, j_4 \sigma_4) \\
\nu(j_3 \sigma_1, j_4 \sigma_2; j_1 \sigma_3, j_2 \sigma_4) &= \nu(j_1 \sigma_1, j_2 \sigma_2; j_3 \sigma_3, j_4 \sigma_4) \\
\nu(j_1 \sigma_3, j_2 \sigma_4; j_3 \sigma_1, j_4 \sigma_2) &= \nu(j_1 \sigma_1, j_2 \sigma_2; j_3 \sigma_3, j_4 \sigma_4) \\
\nu(j_2 \sigma_2, j_1 \sigma_1; j_3 \sigma_3, j_4 \sigma_4) &= -\nu(j_1 \sigma_1, j_2 \sigma_2; j_3 \sigma_3, j_4 \sigma_4) \\
\nu(j_1 \sigma_1, j_2 \sigma_2; j_4 \sigma_4, j_3 \sigma_3) &= -\nu(j_1 \sigma_1, j_2 \sigma_2; j_3 \sigma_3, j_4 \sigma_4) \\
\nu(j_1 \sigma_2, j_2 \sigma_1; j_3 \sigma_4, j_4 \sigma_3) &= \nu(j_1 \sigma_1, j_2 \sigma_2; j_3 \sigma_3, j_4 \sigma_4).
\end{aligned} \tag{4.5}$$

4.2. The splitting in different channels

Since the evaluation of the complete fRG flow equations including frequency and space structure is numerically not feasible (see the discussion in section 4.3), we will use an approximation scheme called the coupled ladder approximation (CLA). This scheme was introduced as approximation for the frequency structure of the single impurity Anderson model (SIAM) in [20, 21] and extended for inhomogeneous systems in [19]. The basic idea is here to divide the two-particle vertex into different channels

$$\gamma_2^\Lambda = \nu + \gamma_p^\Lambda + \gamma_x^\Lambda + \gamma_d^\Lambda, \tag{4.6}$$

where ν is the bare vertex and γ_p^Λ , γ_x^Λ , and γ_d^Λ are referred to as the particle-particle channel, the exchange part and the direct part of the particle-hole channel, respectively.

These channels are defined by the flow equation of the two-particle vertex γ_2 (2.39) via

$$\begin{aligned}\frac{d}{d\Lambda}\gamma_p^\Lambda(q'_1, q'_2; q_1, q_2) &= T \sum_{q_3, q_4, q'_3, q'_4} \gamma_2^\Lambda(q'_1, q'_2; q_3, q_4) \mathcal{S}_{q_3, q'_3}^\Lambda \mathcal{G}_{q_4, q'_4}^\Lambda \gamma_2^\Lambda(q'_3, q'_4; q_1, q_2) \\ \frac{d}{d\Lambda}\gamma_x^\Lambda(q'_1, q'_2; q_1, q_2) &= T \sum_{q_3, q_4, q'_3, q'_4} \gamma_2^\Lambda(q'_1, q'_4; q_3, q_2) \left[\mathcal{S}_{q_3, q'_3}^\Lambda \mathcal{G}_{q_4, q'_4}^\Lambda + \mathcal{G}_{q_3, q'_3}^\Lambda \mathcal{S}_{q_4, q'_4}^\Lambda \right] \gamma_2^\Lambda(q'_3, q'_2; q_1, q_4) \\ \frac{d}{d\Lambda}\gamma_d^\Lambda(q'_1, q'_2; q_1, q_2) &= -T \sum_{q_3, q_4, q'_3, q'_4} \gamma_2^\Lambda(q'_1, q'_3; q_1, q_4) \left[\mathcal{S}_{q_4, q'_4}^\Lambda \mathcal{G}_{q_3, q'_3}^\Lambda + \mathcal{G}_{q_4, q'_4}^\Lambda \mathcal{S}_{q_3, q'_3}^\Lambda \right] \gamma_2^\Lambda(q'_4, q'_2; q_3, q_2),\end{aligned}\tag{4.7}$$

where we applied the earlier mentioned truncation of the fRG flow $\gamma_n = 0$ for $n > 2$, and thus

$$\frac{d}{d\Lambda}\gamma_2^\Lambda = \frac{d}{d\Lambda}(\gamma_p^\Lambda + \gamma_x^\Lambda + \gamma_d^\Lambda).\tag{4.8}$$

For completeness, we write here also the flow equation for the 1PI one-particle vertex which remains

$$\frac{d}{d\Lambda}\gamma_1^\Lambda(q'_1, q_1) = T \sum_{q'_2, q_2} \mathcal{S}_{q_2, q'_2}^\Lambda \gamma_2^\Lambda(q'_2, q'_1; q_2, q_1).\tag{4.9}$$

In fact, this division is based on the index structure of the r.h.s of the flow equations. This is most clearly seen by looking at Figure 4.1, where we have drawn the flow equations of γ_2^Λ in a diagrammatic fashion. The advantage of the division will become clear as soon as we set up the CLA. The indices q of the particles consist in our case of three different parts, namely the site j , the spin σ , as well as the Matsubara frequency ω_n . Since the frequency is conserved at each vertex

$$\begin{aligned}\gamma_1(q'_1, q_1) &\sim \delta(\omega_{n'_1} - \omega_{n_1}) \\ \gamma_2(q'_1, q'_2; q_1, q_2) &\sim \delta(\omega_{n'_1} + \omega_{n'_2} - \omega_{n_1} - \omega_{n_2})\end{aligned}\tag{4.10}$$

we can parametrize the frequency dependence of our vertices in terms of the three bosonic frequencies

$$\begin{aligned}\Pi &= \omega_{n'_1} + \omega_{n'_2} = \omega_{n_1} + \omega_{n_2} \\ X &= \omega_{n'_2} - \omega_{n_1} = \omega_{n_2} - \omega_{n'_1} \\ \Delta &= \omega_{n'_1} - \omega_{n_1} = \omega_{n_2} - \omega_{n'_2},\end{aligned}\tag{4.11}$$

or solved for the fermionic frequencies

$$\begin{aligned}\omega_{n'_1} &= \frac{1}{2}(\Pi - X + \Delta) \\ \omega_{n'_2} &= \frac{1}{2}(\Pi + X - \Delta) \\ \omega_{n_1} &= \frac{1}{2}(\Pi - X - \Delta) \\ \omega_{n_2} &= \frac{1}{2}(\Pi + X + \Delta).\end{aligned}\tag{4.12}$$

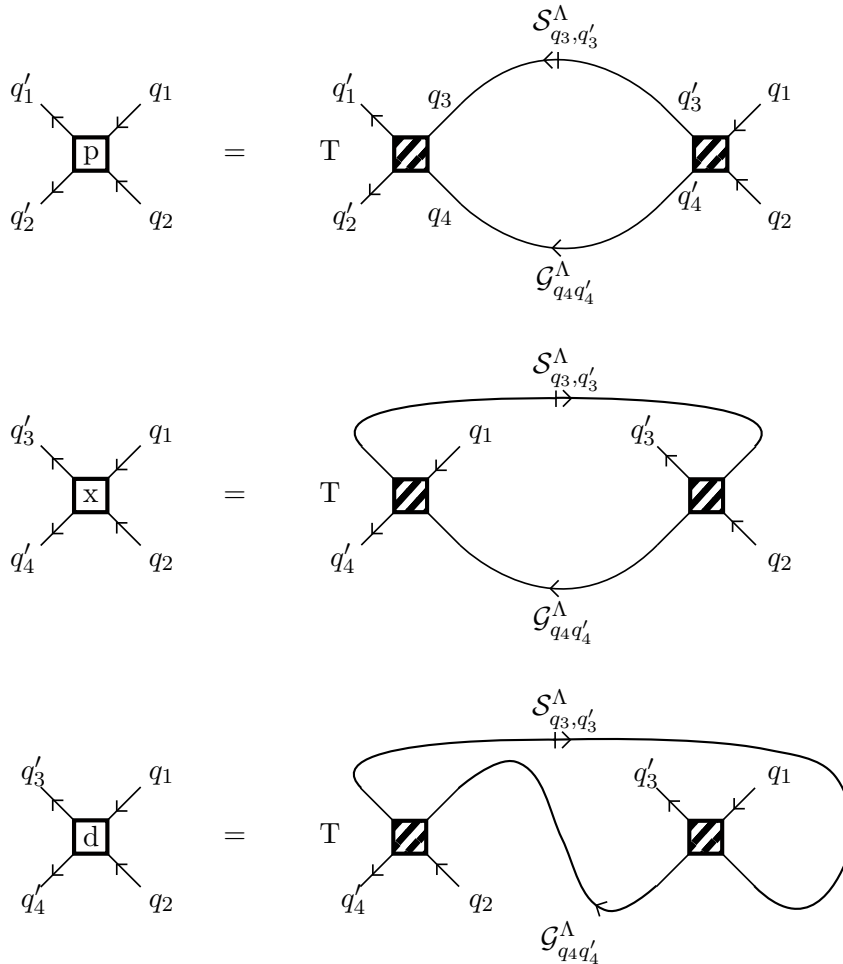


Figure 4.1.: The flow equations of the two particle vertex written in a diagrammatic fashion. The vertices with diagonal stripes correspond to the 1PI two-particle vertices, lines with an arrow are Green's functions, a line with an arrow followed by a bar denotes the single scale propagator, and the vertices with an letter p, x, d denote the channels as introduced above. Note that we employ here no conventions regarding implicit factors, in particular there are no implicit minus signs.

When we apply the coupled ladder approximation in the next section, it will turn out that in this approximation each of the different γ_2 's depends only on one of these bosonic frequencies.

4.3. The coupled ladder approximation

In order to arrive at the CLA, we will now sweep through a chain of improved approximation schemes. If we make the replacement

$$\gamma_2^\Lambda(\Pi, X, \Delta) \rightarrow \nu \quad (4.13)$$

on the r.h.s. of the equations (4.7), we end up in generating all the diagrams appearing in second order perturbation theory with an additional feedback in the self energy. By looking at this second order diagrams, we notice that the generated index, spin, and frequency structures of the channels are of the form

$$P_{j_3 j_4 j_1 j_2}^{\sigma\sigma}(\Pi) = \gamma_p^\Lambda(j_3 \sigma \Pi - \omega'_n, j_4 \sigma \omega'_n; j_1 \sigma \Pi - \omega_n, j_2 \sigma \omega_n) \quad (4.14)$$

$$O(U^2) \hat{=} \sum_{i_1, i_2, i_3, i_4} \sum_{\omega''_n} \begin{array}{c} \omega''_n \sigma \\ \swarrow \quad \searrow \\ \bullet \quad \quad \bullet \\ \nwarrow \quad \nearrow \\ j_3 \sigma \Pi - \omega'_n \quad j_1 \sigma \Pi - \omega_n \\ \swarrow \quad \searrow \\ j_4 \sigma \omega'_n \quad j_2 \sigma \omega_n \\ \Pi - \omega''_n \sigma \end{array}$$

$$P_{j_3 j_4 j_1 j_2}^{\sigma\bar{\sigma}}(\Pi) = \gamma_p^\Lambda(j_3 \sigma \Pi - \omega'_n, j_4 \bar{\sigma} \omega'_n; j_1 \sigma \Pi - \omega_n, j_2 \bar{\sigma} \omega_n) \quad (4.15)$$

$$O(U^2) \hat{=} \sum_{\mu} \sum_{i_1, i_2, i_3, i_4} \sum_{\omega''_n} \begin{array}{c} \omega''_n \mu \\ \swarrow \quad \searrow \\ \bullet \quad \quad \bullet \\ \nwarrow \quad \nearrow \\ j_3 \sigma \Pi - \omega'_n \quad j_1 \sigma \Pi - \omega_n \\ \swarrow \quad \searrow \\ j_4 \bar{\sigma} \omega'_n \quad j_2 \bar{\sigma} \omega_n \\ \Pi - \omega''_n \bar{\mu} \end{array}$$

$$\bar{P}_{j_3 j_4 j_1 j_2}^{\sigma\bar{\sigma}}(\Pi) = \gamma_p^\Lambda(j_3 \sigma \Pi - \omega'_n, j_4 \bar{\sigma} \omega'_n; j_1 \bar{\sigma} \Pi - \omega_n, j_2 \sigma \omega_n) \quad (4.16)$$

$$O(U^2) \hat{=} \sum_{\mu} \sum_{i_1, i_2, i_3, i_4} \sum_{\omega''_n} \begin{array}{c} \omega''_n \mu \\ \swarrow \quad \searrow \\ \bullet \quad \quad \bullet \\ \nwarrow \quad \nearrow \\ j_3 \sigma \Pi - \omega'_n \quad j_1 \bar{\sigma} \Pi - \omega_n \\ \swarrow \quad \searrow \\ j_4 \bar{\sigma} \omega'_n \quad j_2 \sigma \omega_n \\ \Pi - \omega''_n \bar{\mu} \end{array}$$

$$X_{j_3 j_4 j_1 j_2}^{\sigma\sigma}(\chi) = \gamma_x^\Lambda(j_3 \sigma \chi + \omega'_n, j_4 \sigma \omega_n; j_1 \sigma \chi + \omega_n, j_2 \sigma \omega'_n) \quad (4.17)$$

$$O(U^2) \hat{=} \sum_{\mu} \sum_{i_1, i_2, i_3, i_4} \sum_{\omega''_n} \left[\begin{array}{c} \begin{array}{c} X + \omega''_n \mu \\ \rightarrow \\ \begin{array}{c} i_1 \mu \quad j_1 \sigma X + \omega_n \quad j_3 \sigma X + \omega_n \quad i_3 \mu \\ \bullet \quad \quad \quad \bullet \\ \leftarrow \\ j_4 \sigma \omega'_n \quad i_4 \mu \quad i_2 \mu \quad j_2 \sigma \omega'_n \\ \omega''_n \mu \end{array} \\ \end{array} \end{array} \right] + \mathcal{G} \leftrightarrow \mathcal{S} \quad (4.18)$$

$$X_{j_3 j_4 j_1 j_2}^{\sigma \bar{\sigma}}(\chi) = \gamma_x^\Lambda(j_3 \sigma \chi + \omega'_n, j_4 \bar{\sigma} \omega_n; j_1 \sigma \chi + \omega_n, j_2 \bar{\sigma} \omega'_n)$$

$$O(U^2) \hat{=} \sum_{i_1, i_2, i_3, i_4} \sum_{\omega''_n} \left[\begin{array}{c} \begin{array}{c} X + \omega''_n \mu \\ \rightarrow \\ \begin{array}{c} i_1 \sigma \quad j_1 \sigma X + \omega_n \quad j_3 \sigma X + \omega_n \quad i_3 \sigma \\ \bullet \quad \quad \quad \bullet \\ \leftarrow \\ j_4 \bar{\sigma} \omega'_n \quad i_4 \bar{\sigma} \quad i_2 \bar{\sigma} \quad j_2 \bar{\sigma} \omega'_n \\ \omega''_n \bar{\mu} \end{array} \\ \end{array} \end{array} \right] + \mathcal{G} \leftrightarrow \mathcal{S} \quad (4.19)$$

$$\bar{X}_{j_3 j_4 j_1 j_2}^{\sigma \bar{\sigma}}(\chi) = \gamma_x^\Lambda(j_3 \sigma \chi + \omega'_n, j_4 \bar{\sigma} \omega_n; j_1 \bar{\sigma} \chi + \omega_n, j_2 \sigma \omega'_n)$$

$$O(U^2) \hat{=} \sum_{\mu} \sum_{i_1, i_2, i_3, i_4} \sum_{\omega''_n} \left[\begin{array}{c} \begin{array}{c} X + \omega''_n \mu \\ \rightarrow \\ \begin{array}{c} i_1 \mu \quad j_1 \sigma X + \omega_n \quad j_3 \sigma X + \omega_n \quad i_3 \mu \\ \bullet \quad \quad \quad \bullet \\ \leftarrow \\ j_4 \sigma \omega'_n \quad i_4 \bar{\mu} \quad i_2 \bar{\mu} \quad j_2 \sigma \omega'_n \\ \omega''_n \bar{\mu} \end{array} \\ \end{array} \end{array} \right] + \mathcal{G} \leftrightarrow \mathcal{S} \quad (4.20)$$

$$D_{j_3 j_4 j_1 j_2}^{\sigma \sigma}(\Delta) = \gamma_d^\Lambda(j_3 \sigma \Delta + \omega'_n, j_4 \sigma \omega_n; j_1 \sigma \omega'_n, j_2 \sigma \Delta + \omega_n)$$

$$O(U^2) \hat{=} \sum_{\mu} \sum_{i_1, i_2, i_3, i_4} \sum_{\omega''_n} \left[\begin{array}{c} \begin{array}{c} \Delta + \omega''_n \mu \\ \rightarrow \\ \begin{array}{c} i_4 \mu \quad i_2 \mu \quad j_3 \sigma \Delta + \omega_n \quad j_1 \sigma \omega'_n \\ \bullet \quad \quad \quad \bullet \\ \leftarrow \\ j_4 \sigma \omega'_n \quad j_2 \sigma \Delta + \omega_n \quad i_3 \mu \quad i_1 \mu \\ \omega''_n \bar{\mu} \end{array} \\ \end{array} \end{array} \right] + \mathcal{G} \leftrightarrow \mathcal{S} \quad (4.21)$$

$$D_{j_3 j_4 j_1 j_2}^{\sigma \bar{\sigma}}(\Delta) = \gamma_d^\Lambda(j_3 \sigma \Delta + \omega'_n, j_4 \bar{\sigma} \omega_n; j_1 \sigma \omega'_n, j_2 \bar{\sigma} \Delta + \omega_n)$$

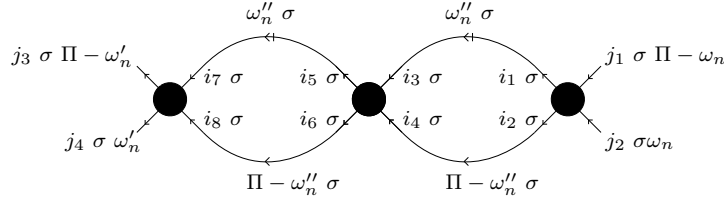
$$O(U^2) \stackrel{\cong}{=} \sum_{\mu} \sum_{i_1, i_2, i_3, i_4} \sum_{\omega''_n} - \left[\text{Diagram} \right] + \mathcal{G} \leftrightarrow \mathcal{S} \quad (4.22)$$

$$O(U^2) \stackrel{\cong}{=} \sum_{i_1, i_2, i_3, i_4} \sum_{\omega''_n} - \left[\text{Diagram} \right] + \mathcal{G} \leftrightarrow \mathcal{S}$$

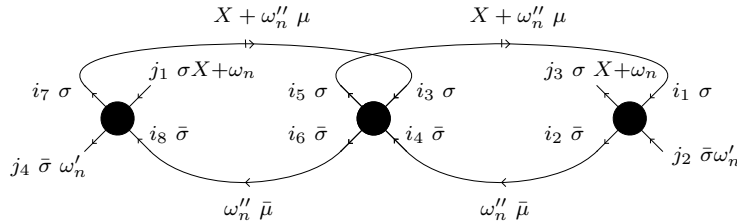
The idea of the CLA is now to improve this second order results by instead of making replacement (4.13), to distinguish between the three channels and set

$$\gamma_2(\Pi, X, \Delta) \rightarrow \nu + \gamma_a(A) \quad (4.23)$$

in the r.h.s. of the flow equation of $\gamma_a(A)$, where $a = p, x, d$ and $A = \Pi, X, \Delta$. The crucial point is that by this improved feed back we do not generate diagrams with new structures in the external indices, but remain with the external index structures we have listed above. To illustrate this, we look at some diagrams of the p- and x-channel generated by that feedback method (cf. the diagrams below), which are essentially RPA like diagrams. The only difference is that here the propagators \mathcal{G}^Λ and \mathcal{S}^Λ also take contributions from the other channels into account.



and analog for the x-channel



Thus, we see that in each diagram generated in the p-channel the two incoming legs are at the same vertex, as well as the outgoing ones. The overall frequency dependence is again given by the single frequency Π . In the x-channel each one incoming and one outgoing line are attached to the same vertex and the frequency structure is again specified by the frequency X . Analogous statements hold for the d-channel.

Here, it is maybe a good point to comment on the names of our channels, which originate in fact, in the on-site interaction case (cf. [19]), i.e. where the bare vertex is given by

$$\nu(j_1 \sigma_1, j_2 \sigma_2; j_3 \sigma_3, j_4 \sigma_4) = U_{j_1} \delta_{j_1 j_2} \delta_{j_3 j_4} \delta_{j_1 j_4} \delta_{\sigma_1 \bar{\sigma}_2} \delta_{\sigma_3 \sigma_4} (\delta_{\sigma_1 \sigma_3} - \delta_{\sigma_1 \sigma_4}). \quad (4.24)$$

The legs attached to one bare vertex all have the same site index. After reducing our second order vertex equations above to this case, only three independent matrix quantities remain (cf. [19]), namely

$$\begin{aligned} P_{ji}^\Lambda(\Pi) &= P_{ji}^{\uparrow\downarrow}(\Pi) \\ X_{ji}^\Lambda(X) &= X_{ji}^{\uparrow\downarrow}(X) \\ D_{ji}^{\sigma\Lambda}(\Delta) &= D_{ji}^{\sigma\sigma}(\Delta). \end{aligned} \quad (4.25)$$

Thus, in the p-channel two incoming particles at site j with opposite spin interact and scatter both to some site i , hence the name particle-particle channel. In the x-channel we have incoming particles at site j with spin σ and site i with spin $\bar{\sigma}$, which after interacting result in one particle at site j with spin $\bar{\sigma}$ and one particle at site i with spin σ . Hence the effective result is a switching of the spins, which may be interpreted as an exchange of the two incoming particles. The d-channel on the other hand has two incoming particles at sites i, j and two outgoing particles at sites i, j , all with the same spin. This can be seen as a direct density-density interaction of the particles, without having to exchange them. Therefore, one ends up with the commonly used names, we introduced above.

Looking again at the diagrams in section 4.3 and section 4.3 above, these parquet like diagrams remind us strongly of the type of diagrams summed in an RPA treatment of the individual channels. However, our channels are at this point already coupled via the self energy entering in the propagators \mathcal{G} and \mathcal{S} and are therefore not independent.

The last step in our CLA treatment is to notice that for certain external site and spin indices and disregarding the frequency dependence, the index structure of different channels can coincide. In fact, this is trivial in the notation we have employed up to now, namely where each of the quantities $A_{j_1 j_2 j_3 j_4}^{\sigma\mu}$ is considered to be a function of independent site indices. Thus, they have $(2N+1)^4$ different values arising from different site combinations. In this notation, the direct feedback of the different channels into each other reads simply

$$\gamma_2 \rightarrow \nu + \gamma_a(A) + \gamma_b(0) + \gamma_c(0), \quad (4.26)$$

i.e. the only artificial restriction to conserve the index structure, is to set the frequencies $B = 0$ and $C = 0$ in order to avoid frequency mixing.

However, later on we will consider only bare off-site interactions with a finite range, i.e. there exists an $0 \leq L \leq 2N + 1$ such that $U_{j_1 j_2} = 0$ for all j_2, j_2 with $|j_1 - j_2| > L$.

Usually, we will think of $L \ll 2N + 1$, thus we have a near on-site interaction. Since in our channels two external legs each are attached to the same bare vertex, it would be an numerical overkill to consider $\gamma_{a j_1 j_2 j_3 j_4}(A)$ as a function with $(2N + 1)^4$ different values in the site indices. Due to the revoked independence of the j_1, j_2, j_3, j_4 indices, most of these values would be zero. To encounter this problem, we will introduce a smaller basis j, i, l, k where $\gamma_{a j_i}^{l k}(A)$ has again only independent values. In this smaller basis, though more suited for actual numerical computations, the feedback of the different channels will become more messy and also the symmetries of the channels will be not so clearly visible. Hence, in order to investigate these symmetries and write down the first version of our fRG flow equations, we will stick with our somewhat "overcomplete" basis. For the numerical treatment it is then easy to transform these symmetries and equations into our new basis.

4.4. A comment on symmetries

Due to the symmetries of our bare vertex and the symmetry $H^T = H$ (i.e. the Hamiltonian H is real), we have lots of symmetries satisfied by our γ_p, γ_x and γ_d channels, as well as the propagators and the self energy. Our approach to study these symmetries, was to first look for symmetries in second order and then check if this symmetries are conserved in the flow equations, thus being correct to arbitrary order in perturbation theory. Since there are many of these symmetries, we will here not derive all of them, but rather show in some exemplary cases the general procedure and then simply state the rest.

Before we look at the individual channels, let's start with a very basic symmetry involving the propagator \mathcal{G} , the selfenergy Σ , and the general two-particle vertex γ_2 . First we take a look at the non-interacting propagator \mathcal{G}^0 :

$$\mathcal{G}^0(\omega_n) = \frac{1}{\omega_n - H_0}, \quad (4.27)$$

where H_0 is the Hamiltonian without the interaction term. Since H_0 is symmetric, so is \mathcal{G}^0 , i.e. $\mathcal{G}_{j_i}^0(\omega_n) = \mathcal{G}_{i_j}^0(\omega_n)$. Furthermore, we have already seen that the bare interaction ν is symmetric under exchange of the incoming with the outgoing legs:

$$\nu(j_1 \sigma_1, j_2 \sigma_2; j_3 \sigma_3, j_4 \sigma_4) = \nu(j_3 \sigma_3, j_4 \sigma_4; j_1 \sigma_1, j_2 \sigma_2). \quad (4.28)$$

Using the interplay of the different flow equations, we now show that these properties hold in fact for the full propagator \mathcal{G}^Λ as well as for the full vertex γ_2^Λ at each step of the flow. Moreover, we will see that the self energy is symmetric in it's indices ¹, too:

$$\begin{aligned} \mathcal{G}^\Lambda(q'_1, q_1) &= \mathcal{G}^\Lambda(q_1, q'_1) \\ \Sigma^\Lambda(q'_1, q_1) &= \Sigma^\Lambda(q_1, q'_1) \\ \gamma_2^\Lambda(q'_1, q'_2; q_1, q_2) &= \gamma_2^\Lambda(q_1, q_2; q'_1, q'_2). \end{aligned} \quad (4.29)$$

¹For the following derivation, it suffices to consider composite indices $q = (j, \sigma, \omega)$ without distinguishing between the space, spin, and frequency component.

Since at the beginning of the flow $\Sigma^{\Lambda_{initial}} = 0$, $\mathcal{G}^{\Lambda_{initial}} = 0$, as well as $\gamma_2^{\Lambda_{initial}} = \nu$ satisfy this properties trivially, we just have to show that they are conserved under the flow equations. Thus, let's look at the derivative of Σ^Λ (2.38)

$$\begin{aligned}
\frac{d}{d\Lambda} \Sigma^\Lambda(q'_1, q_1) &= -T \sum_{q'_2, q_2} \text{Diagram 1} &= -T \sum_{q'_2, q_2} \text{Diagram 2} \\
&= -T \sum_{q'_2, q_2} \text{Diagram 3} &= -T \sum_{q'_2, q_2} \text{Diagram 4} \\
&= \frac{d}{d\Lambda} \Sigma^\Lambda(q_1, q'_1)
\end{aligned}$$

Therefore, the self energy is symmetric in it's indices. In the same way, it is easy to show that the self energy is diagonal in spin and frequency space. If one then computes the new propagator $\mathcal{G}^{\Lambda_{initial}-\Delta\Lambda}$ from the Dyson equation, it also will be diagonal in spin space and symmetric in the site indices. It remains to show the symmetry in γ_2 . For this we look back at equations (4.7). For example one can easily calculate for the p-channel:

$$\begin{aligned}
\frac{d}{d\Lambda} \gamma_p^\Lambda(q'_1, q'_2; q_1, q_2) &= T \sum_{q'_3, q_3, q'_4, q_4} \text{Diagram 1} \\
&= T \sum_{q'_3, q_3, q'_4, q_4} \text{Diagram 2} \cdot \text{Diagram 3}
\end{aligned}$$

$$\begin{aligned}
&= T \sum_{q'_3, q_3, q'_4, q_4} \begin{array}{c} q_3 \quad q'_1 \\ \swarrow \quad \searrow \\ \text{[shaded box]} \\ \nwarrow \quad \nearrow \\ q_4 \quad q'_2 \end{array} \cdot \begin{array}{c} q_1 \quad q'_3 \\ \swarrow \quad \searrow \\ \text{[shaded box]} \\ \nwarrow \quad \nearrow \\ q_2 \quad q'_4 \end{array} S_{q'_3 q_3}^\Lambda G_{q'_4 q_4}^\Lambda \\
&= T \sum_{q'_3, q_3, q'_4, q_4} \begin{array}{c} q_1 \quad q'_3 \\ \swarrow \quad \searrow \\ \text{[shaded box]} \\ \nwarrow \quad \nearrow \\ q_2 \quad q'_4 \end{array} \begin{array}{c} S_{q'_3 q_3}^\Lambda \\ \text{---} \\ G_{q'_4 q_4}^\Lambda \end{array} \begin{array}{c} q_3 \quad q'_1 \\ \swarrow \quad \searrow \\ \text{[shaded box]} \\ \nwarrow \quad \nearrow \\ q_4 \quad q'_2 \end{array} \\
&= \frac{d}{d\Lambda} \gamma_p^\Lambda(q_1, q_2; q'_1, q'_2)
\end{aligned}$$

and likewise for the other channels:

$$\begin{aligned}
\frac{d}{d\Lambda} \gamma_x^\Lambda(q'_1, q'_2; q_1, q_2) &= \frac{d}{d\Lambda} \gamma_x^\Lambda(q_1, q_2; q'_1, q'_2) \\
\frac{d}{d\Lambda} \gamma_d^\Lambda(q'_1, q'_2; q_1, q_2) &= \frac{d}{d\Lambda} \gamma_d^\Lambda(q_1, q_2; q'_1, q'_2)
\end{aligned} \tag{4.30}$$

Therefore, we indeed have shown that (4.28) holds for the new $\Lambda_{initial} + \delta\Lambda$ when we go an infinitesimal step $\delta\Lambda$ with the flow. Thus, in the interplay with each other these three symmetries are conserved during the whole flow.

From this basic symmetry follow as a direct consequence lots of symmetries in the individual vertex quantities, for example

$$P_{j_3 j_4 j_1 j_2}^{\sigma\sigma}(\Pi) = P_{j_1 j_2 j_3 j_4}^{\sigma\sigma}(\Pi). \tag{4.31}$$

For the previous symmetries we used just the properties of the general flow equations (4.7). However, there are also symmetries especially introduced by our CLA treatment of the flow. As an example we show here one of them, namely

$$X_{j_3 j_4 j_1 j_2}^{\sigma\bar{\sigma}}(X) = X_{j_4 j_3 j_2 j_1}^{\bar{\sigma}\sigma}(-X). \tag{4.32}$$

Since the symmetry is trivially satisfied at $\Lambda_{initial}$ it again suffices to show that it is conserved under the flow (with the applied CLA)

Likewise we can argue in a lot of other cases and end up with a long list of symmetries

$$\begin{aligned}
\mathcal{G}_{ij}^{\sigma\Lambda}(\omega_n) &= \mathcal{G}_{ji}^{\sigma\Lambda}(\omega_n) = [\mathcal{G}_{ij}^{\sigma\Lambda}(-\omega_n)]^* \\
\Sigma_{ij}^{\sigma\Lambda}(\omega_n) &= \Sigma_{ji}^{\sigma\Lambda}(\omega_n) = [\Sigma_{ij}^{\sigma\Lambda}(-\omega_n)]^* \\
P_{j_3j_4j_1j_2}^{\sigma\sigma}(\Pi) &= P_{j_1j_2j_3j_4}^{\sigma\sigma}(\Pi) \\
P_{j_4j_3j_1j_2}^{\sigma\sigma}(\Pi) &= -P_{j_3j_4j_1j_2}^{\sigma\sigma}(\Pi) \\
P_{j_3j_4j_2j_1}^{\sigma\sigma}(\Pi) &= -P_{j_3j_4j_1j_2}^{\sigma\sigma}(\Pi) \\
P_{j_3j_4j_1j_2}^{\sigma\bar{\sigma}}(\Pi) &= P_{j_1j_2j_3j_4}^{\sigma\bar{\sigma}}(\Pi) \\
P_{j_3j_4j_1j_2}^{\bar{\sigma}\sigma}(\Pi) &= P_{j_4j_3j_2j_1}^{\bar{\sigma}\sigma}(\Pi) \\
\bar{P}_{j_3j_4j_1j_2}^{\sigma\bar{\sigma}}(\Pi) &= \bar{P}_{j_1j_2j_3j_4}^{\sigma\bar{\sigma}}(\Pi) = \bar{P}_{j_2j_1j_4j_3}^{\sigma\bar{\sigma}}(\Pi) \\
\bar{P}_{j_3j_4j_1j_2}^{\bar{\sigma}\sigma}(\Pi) &= \bar{P}_{j_4j_3j_2j_1}^{\bar{\sigma}\sigma}(\Pi) \\
P_{j_3j_4j_1j_2}^{\sigma\bar{\sigma}}(\Pi) &= -\bar{P}_{j_4j_3j_1j_2}^{\bar{\sigma}\sigma}(\Pi) \Rightarrow \bar{P}_{j_3j_4j_1j_2}^{\sigma\bar{\sigma}}(\Pi) = -P_{j_4j_3j_1j_2}^{\bar{\sigma}\sigma}(\Pi) \\
[P_{j_3j_4j_1j_2}^{\sigma\sigma}(\Pi)]^* &= P_{j_3j_4j_1j_2}^{\sigma\sigma}(-\Pi) \\
[P_{j_3j_4j_1j_2}^{\sigma\bar{\sigma}}(\Pi)]^* &= P_{j_3j_4j_1j_2}^{\sigma\bar{\sigma}}(-\Pi) \\
[P_{j_3j_4j_1j_2}^{\bar{\sigma}\sigma}(\Pi)]^* &= P_{j_3j_4j_1j_2}^{\bar{\sigma}\sigma}(-\Pi) \\
[X_{j_3j_4j_1j_2}^{\sigma\sigma}] &= X_{j_1j_2j_3j_4}^{\sigma\sigma} \\
[X_{j_3j_4j_1j_2}^{\sigma\bar{\sigma}}] &= X_{j_1j_2j_3j_4}^{\sigma\bar{\sigma}} \\
[\bar{X}_{j_3j_4j_1j_2}^{\sigma\bar{\sigma}}] &= \bar{X}_{j_1j_2j_3j_4}^{\sigma\bar{\sigma}} \\
[X_{j_3j_4j_1j_2}^{\sigma\sigma}(\chi)]^* &= X_{j_3j_4j_1j_2}^{\sigma\sigma}(-\chi) \\
[X_{j_3j_4j_1j_2}^{\sigma\bar{\sigma}}(\chi)]^* &= X_{j_3j_4j_1j_2}^{\sigma\bar{\sigma}}(-\chi) \\
[\bar{X}_{j_3j_4j_1j_2}^{\sigma\bar{\sigma}}(\chi)]^* &= \bar{X}_{j_3j_4j_1j_2}^{\sigma\bar{\sigma}}(-\chi) \\
X_{j_3j_4j_1j_2}^{\sigma\bar{\sigma}}(-\chi) &= X_{j_4j_3j_2j_1}^{\sigma\bar{\sigma}}(\chi) \\
\bar{X}_{j_3j_4j_1j_2}^{\sigma\bar{\sigma}}(-\chi) &= \bar{X}_{j_2j_1j_4j_3}^{\sigma\bar{\sigma}}(\chi) \\
X_{j_3j_4j_1j_2}^{\sigma\sigma}(-\chi) &= X_{j_4j_3j_2j_1}^{\sigma\sigma}(\chi) \\
X_{j_3j_4j_1j_2}^{\sigma\sigma}(\chi) &= -D_{j_3j_4j_2j_1}^{\sigma\sigma}(\chi) \Rightarrow D_{j_3j_4j_1j_2}^{\sigma\sigma}(\chi) = -X_{j_3j_4j_2j_1}^{\sigma\sigma}(\chi) \\
X_{j_3j_4j_1j_2}^{\sigma\bar{\sigma}}(\chi) &= -\bar{D}_{j_3j_4j_2j_1}^{\sigma\bar{\sigma}}(\chi) \Rightarrow \bar{D}_{j_3j_4j_1j_2}^{\sigma\bar{\sigma}}(\chi) = -X_{j_3j_4j_2j_1}^{\sigma\bar{\sigma}}(\chi) \\
\bar{X}_{j_3j_4j_1j_2}^{\sigma\bar{\sigma}}(\chi) &= -D_{j_3j_4j_2j_1}^{\sigma\bar{\sigma}}(\chi) \Rightarrow D_{j_3j_4j_1j_2}^{\sigma\bar{\sigma}}(\chi) = -\bar{X}_{j_3j_4j_2j_1}^{\sigma\bar{\sigma}}(\chi)
\end{aligned} \tag{4.33}$$

Due to the symmetries above, there exist only seven independent vertex quantities. Namely,

$$\begin{aligned}
P_{j_3j_4j_1j_2}^{\sigma\sigma}(\Pi) &= \gamma_p^\Lambda(j_3 \sigma \Pi - \omega'_n, j_4 \sigma \omega'_n; j_1 \sigma \Pi - \omega_n, j_2 \sigma \omega_n) \\
P_{j_3j_4j_1j_2}^{\uparrow\downarrow}(\Pi) &= \gamma_p^\Lambda(j_3 \uparrow \Pi - \omega'_n, j_4 \downarrow \omega'_n; j_1 \uparrow \Pi - \omega_n, j_2 \downarrow \omega_n) \\
X_{j_3j_4j_1j_2}^{\uparrow\downarrow}(X) &= \gamma_x^\Lambda(j_3 \uparrow X + \omega'_n, j_4 \downarrow \omega_n; j_1 \uparrow X + \omega_n, j_2 \downarrow \omega'_n) \\
\bar{X}_{j_3j_4j_1j_2}^{\uparrow\downarrow}(X) &= \gamma_x^\Lambda(j_3 \uparrow X + \omega'_n, j_4 \downarrow \omega_n; j_1 \downarrow X + \omega_n, j_2 \uparrow \omega'_n) \\
D_{j_3j_4j_1j_2}^{\sigma\sigma}(\Delta) &= \gamma_d^\Lambda(j_3 \sigma \Delta + \omega'_n, j_4 \sigma \omega_n; j_1 \sigma \omega'_n, j_2 \sigma \Delta + \omega_n),
\end{aligned} \tag{4.35}$$

where σ can take both the values \uparrow and \downarrow . Thus, we will write down the flow equations for this vertex quantities in the next section.

4.5. The flow equations in general coordinates

The derivation of the flow equations for the individual vertex quantities always goes along the same line. First we use in the general equations (4.7) the coupled ladder approximation and write down the resulting equations in terms of γ_p^Λ , γ_x^Λ and γ_d^Λ , including the direct feedback of the different channels into each other. As an example we write this down here for $P_{j_3 j_4 j_1 j_2}^{\sigma\sigma}(\Pi)$:

$$\begin{aligned}
& \dot{P}_{j_3 j_4 j_1 j_2}^{\sigma\sigma}(\Pi) = \dot{\gamma}_p^\Lambda(j_3 \sigma \Pi - \omega'_n, j_4 \sigma \omega'_n; j_1 \sigma \Pi - \omega_n, j_2 \sigma \omega_n) = \\
& = \sum_{\omega''_n} T \gamma_2^\Lambda(j_3 \sigma \Pi - \omega'_n, j_4 \sigma \omega'_n; i_3 \sigma \Pi - \omega''_n, i_4 \sigma \omega''_n) S_{i_3 i_1}^{\sigma\Lambda}(\Pi - \omega'') \mathcal{G}_{i_4 i_2}^{\sigma\Lambda}(\omega''_n) \cdot \\
& \quad \gamma_2^\Lambda(i_1 \sigma \Pi - \omega''_n, i_2 \sigma \omega''_n; j_1 \sigma \Pi - \omega_n, j_2 \sigma \omega_n) \\
& = \sum_{\omega''_n} T \left\{ \nu(j_3 \sigma, j_4 \sigma; i_3 \sigma, i_4 \sigma) + \gamma_p^\Lambda(j_3 \sigma \Pi - \omega'_n, j_4 \sigma \omega'_n; i_3 \sigma \Pi - \omega''_n, i_4 \sigma \omega''_n) \right. \\
& \quad \left. + \gamma_x^\Lambda(j_3 \sigma - \omega'_n, j_4 \sigma \omega'_n; i_3 \sigma - \omega''_n, i_4 \sigma \omega''_n) + \gamma_d^\Lambda(j_3 \sigma - \omega'_n, j_4 \sigma \omega'_n; i_3 \sigma - \omega''_n, i_4 \sigma \omega''_n) \right\} \cdot \\
& \quad S_{i_3 i_1}^{\sigma\Lambda}(\Pi - \omega''_n) \mathcal{G}_{i_4 i_2}^{\sigma\Lambda}(\omega''_n) \cdot \\
& \quad \left\{ \nu(i_1 \sigma, i_2 \sigma; j_1 \sigma, j_2 \sigma) + \gamma_p^\Lambda(i_1 \sigma \Pi - \omega''_n, i_2 \sigma \omega''_n; j_1 \sigma \Pi - \omega_n, j_2 \sigma \omega_n) \right. \\
& \quad \left. + \gamma_x^\Lambda(i_1 \sigma \Pi - \omega''_n, i_2 \sigma \omega''_n; j_1 \sigma \Pi - \omega_n, j_2 \sigma \omega_n) + \gamma_d^\Lambda(i_1 \sigma \Pi - \omega''_n, i_2 \sigma \omega''_n; j_1 \sigma \Pi - \omega_n, j_2 \sigma \omega_n) \right\} \\
& = \sum_{\omega''_n} T \left\{ \nu(j_3 \sigma, j_4 \sigma; i_3 \sigma, i_4 \sigma) + P_{j_3 j_4 i_3 i_4}^{\sigma\sigma}(\Pi) + X_{j_3 j_4 i_3 i_4}^{\sigma\sigma}(0) + D_{j_3 j_4 i_3 i_4}^{\sigma\sigma}(0) \right\} \\
& \quad S_{i_3 i_1}^{\sigma\Lambda}(\Pi - \omega''_n) \mathcal{G}_{i_4 i_2}^{\sigma\Lambda}(\omega''_n) \cdot \\
& \quad \left\{ \nu(i_1 \sigma, i_2 \sigma; j_1 \sigma, j_2 \sigma) + P_{i_1 i_2 j_1 j_2}^{\sigma\sigma}(\Pi) + X_{i_1 i_2 j_1 j_2}^{\sigma\sigma}(0) + D_{i_1 i_2 j_1 j_2}^{\sigma\sigma}(0) \right\}
\end{aligned} \tag{4.36}$$

Using all our symmetries from above 4.33, the flow equations can finally be cast into the form

$$\begin{aligned}
& \dot{P}_{j_3 j_4 j_1 j_2}^{\sigma\sigma}(\Pi) = T \left\{ \nu(j_3 \sigma, j_4 \sigma; i_3 \sigma, i_4 \sigma) + P_{j_3 j_4 i_3 i_4}^{\sigma\sigma}(\Pi) - D_{j_3 j_4 i_4 i_3}^{\sigma\sigma}(0) + D_{j_3 j_4 i_3 i_4}^{\sigma\sigma}(0) \right\} \\
& \quad \sum_{\omega''_n} S_{i_3 i_1}^{\sigma\Lambda}(\Pi - \omega''_n) \mathcal{G}_{i_4 i_2}^{\sigma\Lambda}(\omega''_n) \\
& \quad \left\{ \nu(i_1 \sigma, i_2 \sigma; j_1 \sigma, j_2 \sigma) + P_{i_1 i_2 j_1 j_2}^{\sigma\sigma}(\Pi) - D_{i_1 i_2 j_2 j_1}^{\sigma\sigma}(0) + D_{i_1 i_2 j_1 j_2}^{\sigma\sigma}(0) \right\}
\end{aligned} \tag{4.37}$$

Analogous we proceed for our other channels and end up with

$$\begin{aligned}
\dot{P}_{j_3 j_4 j_1 j_2}^{\sigma \bar{\sigma}}(\Pi) &= T \left\{ \nu(j_3 \sigma, j_4 \bar{\sigma}; i_3 \sigma, i_4 \bar{\sigma}) + P_{j_3 j_4 i_3 i_4}^{\sigma \bar{\sigma}}(\Pi) + X_{j_3 j_4 i_3 i_4}^{\sigma \bar{\sigma}}(0) - \bar{X}_{j_3 j_4 i_4 i_3}^{\sigma \bar{\sigma}}(0) \right\} \\
&\sum_{\omega_n''} S_{i_3 i_1}^{\sigma \Lambda}(\Pi - \omega_n'') \mathcal{G}_{i_4 i_2}^{\bar{\sigma}}(\omega_n'') \\
&\left\{ \nu(i_1 \sigma, i_2 \bar{\sigma}; j_1 \sigma, j_2 \bar{\sigma}) + P_{i_1 i_2 j_1 j_2}^{\sigma \bar{\sigma}}(\Pi) + X_{i_1 i_2 j_1 j_2}^{\sigma \bar{\sigma}}(0) - \bar{X}_{i_1 i_2 j_2 j_1}^{\sigma \bar{\sigma}}(0) \right\} \\
&+ T \left\{ \nu(j_3 \sigma, j_4 \bar{\sigma}; i_3 \bar{\sigma}, i_4 \sigma) - P_{j_3 j_4 i_4 i_3}^{\sigma \bar{\sigma}}(\Pi) + \bar{X}_{j_3 j_4 i_3 i_4}^{\sigma \bar{\sigma}}(0) - X_{j_3 j_4 i_4 i_3}^{\sigma \bar{\sigma}}(0) \right\} \\
&\sum_{\omega_n''} S_{i_3 i_1}^{\sigma \Lambda}(\Pi - \omega_n'') \mathcal{G}_{i_4 i_2}^{\sigma \Lambda}(\omega_n'') \\
&\left\{ \nu(i_1 \bar{\sigma}, i_2 \sigma; j_1 \sigma, j_2 \bar{\sigma}) - P_{i_2 i_1 j_1 j_2}^{\sigma \bar{\sigma}}(\Pi) + \bar{X}_{i_1 i_2 j_1 j_2}^{\sigma \bar{\sigma}}(0) - X_{i_1 i_2 j_2 j_1}^{\sigma \bar{\sigma}}(0) \right\}
\end{aligned} \tag{4.38}$$

$$\begin{aligned}
\dot{X}_{j_3 j_4 j_1 j_2}^{\sigma \bar{\sigma}}(\chi) &= T \left\{ \nu(j_3 \sigma, i_4 \bar{\sigma}; i_1 \sigma, j_2 \bar{\sigma}) + X_{j_3 i_4 i_1 j_2}^{\sigma \bar{\sigma}}(\chi) + P_{j_3 i_4 i_1 j_2}^{\sigma \bar{\sigma}}(0) - \bar{X}_{j_3 i_4 j_2 i_1}^{\sigma \bar{\sigma}}(0) \right\} \\
&\sum_{\omega_n''} \left[S_{i_1 i_3}^{\sigma \Lambda}(\chi + \omega_n'') \mathcal{G}_{i_2 i_4}^{\bar{\sigma} \Lambda}(\omega_n'') + \mathcal{G} \leftrightarrow S \right] \\
&\left\{ \nu(i_3 \sigma, j_4 \bar{\sigma}; j_1 \sigma, i_2 \bar{\sigma}) + X_{i_3 j_4 j_1 i_2}^{\sigma \bar{\sigma}}(\chi) + P_{i_3 j_4 j_1 i_2}^{\sigma \bar{\sigma}}(0) - \bar{X}_{i_3 j_4 i_2 j_1}^{\sigma \bar{\sigma}}(0) \right\}
\end{aligned} \tag{4.39}$$

$$\begin{aligned}
\dot{\bar{X}}_{j_3 j_4 j_1 j_2}^{\sigma \bar{\sigma}}(\chi) &= T \left\{ \nu(j_3 \sigma, i_4 \sigma; i_1 \sigma, j_2 \sigma) - D_{j_3 i_4 j_2 i_1}^{\sigma \sigma}(\chi) + P_{j_3 i_4 i_1 j_2}^{\sigma \sigma}(0) + D_{j_3 i_4 i_1 j_2}^{\sigma \sigma}(0) \right\} \\
&\sum_{\omega_n''} \left[S_{i_1 i_3}^{\sigma \Lambda}(\chi + \omega_n'') \mathcal{G}_{i_2 i_4}^{\sigma \Lambda}(\omega_n'') + \mathcal{G} \leftrightarrow S \right] \\
&\left\{ \nu(i_3 \sigma, j_4 \bar{\sigma}; j_1 \bar{\sigma}, i_2 \sigma) + \bar{X}_{i_3 j_4 j_1 i_2}^{\sigma \bar{\sigma}}(\chi) - P_{i_3 j_4 i_2 j_1}^{\sigma \bar{\sigma}}(0) - X_{i_3 j_4 i_2 j_1}^{\sigma \bar{\sigma}}(0) \right\} \\
&+ T \left\{ \nu(j_3 \sigma, i_4 \bar{\sigma}; i_1 \bar{\sigma}, j_2 \sigma) + \bar{X}_{j_3 i_4 i_1 j_2}^{\sigma \bar{\sigma}}(\chi) - P_{j_3 i_4 j_2 i_1}^{\sigma \bar{\sigma}}(0) - X_{j_3 i_4 j_2 i_1}^{\sigma \bar{\sigma}}(0) \right\} \\
&\sum_{\omega_n''} \left[S_{i_1 i_3}^{\bar{\sigma} \Lambda}(\chi + \omega_n'') \mathcal{G}_{i_2 i_4}^{\bar{\sigma} \Lambda}(\omega_n'') + \mathcal{G} \leftrightarrow S \right] \\
&\left\{ \nu(i_3 \bar{\sigma}, j_4 \bar{\sigma}; j_1 \bar{\sigma}, i_2 \bar{\sigma}) - D_{i_3 j_4 i_2 j_1}^{\bar{\sigma} \bar{\sigma}}(\chi) + P_{i_3 j_4 j_1 i_2}^{\bar{\sigma} \bar{\sigma}}(0) + D_{i_3 j_4 j_1 i_2}^{\bar{\sigma} \bar{\sigma}}(0) \right\}
\end{aligned} \tag{4.40}$$

$$\begin{aligned}
\dot{D}_{j_3 j_4 j_1 j_2}^{\sigma\sigma}(\Delta) &= -T \left\{ \nu(j_3\sigma, i_4\sigma; j_1\sigma, i_2\sigma) + D_{j_3 i_4 j_1 i_2}^{\sigma\sigma}(\Delta) + P_{j_3 i_4 j_1 i_2}^{\sigma\sigma}(0) - D_{j_3 i_4 i_2 j_1}^{\sigma\sigma}(0) \right\} \\
&\sum_{\omega''_n} \left[S_{i_2 i_3}^{\sigma\Lambda}(\Delta + \omega''_n) \mathcal{G}_{i_1 i_4}^{\sigma\Lambda}(\omega''_n) + \mathcal{G} \leftrightarrow S \right] \\
&\left\{ \nu(i_3\sigma, j_4\sigma; i_1\sigma, j_2\sigma) + D_{i_3 j_4 i_1 j_2}^{\sigma\sigma}(\Delta) + P_{i_3 j_4 i_1 j_2}^{\sigma\sigma}(0) - D_{i_3 j_4 j_2 i_1}^{\sigma\sigma}(0) \right\} \\
&- T \left\{ \nu(j_3\sigma, i_4\bar{\sigma}; j_1\sigma, i_2\bar{\sigma}) - \bar{X}_{j_3 i_4 i_2 j_1}^{\sigma\bar{\sigma}}(\Delta) + P_{j_3 i_4 j_1 i_2}^{\sigma\bar{\sigma}}(0) + X_{j_3 i_4 j_1 i_2}^{\sigma\bar{\sigma}}(0) \right\} \\
&\sum_{\omega''_n} \left[S_{i_2 i_3}^{\bar{\sigma}\Lambda}(\Delta + \omega''_n) \mathcal{G}_{i_1 i_4}^{\bar{\sigma}\Lambda}(\omega''_n) + \mathcal{G} \leftrightarrow S \right] \\
&\left\{ \nu(i_3\bar{\sigma}, j_4\sigma; i_1\bar{\sigma}, j_2\sigma) - \bar{X}_{i_3 j_4 j_2 i_1}^{\bar{\sigma}\sigma}(\Delta) + P_{j_4 i_3 j_2 i_1}^{\bar{\sigma}\sigma}(0) + X_{i_3 j_4 i_1 j_2}^{\bar{\sigma}\sigma}(0) \right\}
\end{aligned} \tag{4.41}$$

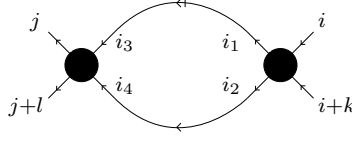
$$\begin{aligned}
\dot{\gamma}_1^\Lambda(j_1\sigma\omega_n; j_2\sigma\omega_n) &= \\
T \sum_{\omega''_n} S_{i_1 i_3}^{\sigma\Lambda}(\omega''_n) &\left\{ \nu(i_3\sigma, j_1\sigma; i_1\sigma, j_2\sigma) + P_{i_3 j_1 i_1 j_2}^{\sigma\sigma}(\omega''_n + \omega_n) - D_{i_3 j_1 j_2 i_1}^{\sigma\sigma}(\omega''_n - \omega_n) + D_{i_3 j_1 i_1 j_2}^{\sigma\sigma}(0) \right\} \\
+ T \sum_{\omega''_n} S_{i_1 i_3}^{\bar{\sigma}\Lambda}(\omega''_n) &\left\{ \nu(i_3\bar{\sigma}, j_1\sigma; i_1\bar{\sigma}, j_2\sigma) + P_{j_1 i_3 j_2 i_1}^{\bar{\sigma}\sigma}(\omega''_n + \omega_n) + X_{i_3 j_1 i_1 j_2}^{\bar{\sigma}\sigma}(\omega''_n - \omega) - \bar{X}_{i_3 j_1 j_2 i_1}^{\bar{\sigma}\sigma}(0) \right\}
\end{aligned} \tag{4.42}$$

4.6. A suitable basis transformation

Having derived the flow equations and the various symmetries for our quantities, we are now in the position to make the transformation to the numerical basis mentioned above. Since we will in the end consider the vertex quantities to be frequency independent, i.e. $\Pi = X = \Delta = 0$, we drop from now on the frequency labels on the vertex quantities for notational convenience. This simplification originates in numerical reasons since the longer ranged feedback introduces a computational factor of $\sim L^3$ compared to the on-site interaction case. Taking also the frequency dependence into account, we would at least need up to a factor of 10^2 frequencies to get a realistic modeling and the computation time would exceed reasonable boundaries. But we want to emphasize that there is no principal difficulty to take also the frequency dependence into account. Now, for the transformation to a numerical basis, we remind our selves of the fact that during the flow we generate only diagrams in which two external legs each are attached to the same bare vertex ν . If we now assume the range of the interaction in (4.1) to be $0 \leq L \leq 2N + 1$, where $2N + 1$ is the number of sites in the interacting region, only two external legs have independent site indices and the other two have to be in the range of the former with a distance smaller or equal to L . According to the different external index structure of the three channels (see (4.3)-(4.3) above), we choose our basis in the following way. For the p-channel set

$$P_{j_3 j_4 j_1 j_2} = P_{j_3 j_1}^{(j_4 - j_3)(j_2 - j_1)} =: P_{j_i}^{lk}, \tag{4.43}$$

where j, i, l, k are given by $j_3 = j, j_4 = j + l, j_1 = i, j_2 = i + k$. In a diagrammatic fashion this is of the form



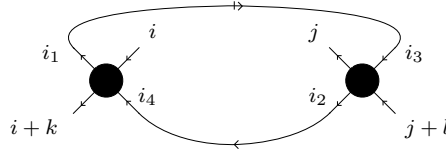
Thus, if we take l, k as the free site indices, running independently from $-L$ to L , j and i will run in the following ranges

$$\left. \begin{array}{l} -N \leq (j+l) \leq N \\ -N \leq j \leq N \end{array} \right\} \Rightarrow \max(-N, -N-l) \leq j \leq \min(N, N-l)$$

$$\left. \begin{array}{l} -N \leq (i+k) \leq N \\ -N \leq i \leq N \end{array} \right\} \Rightarrow \max(-N, -N-k) \leq i \leq \min(N, N-k).$$
(4.44)

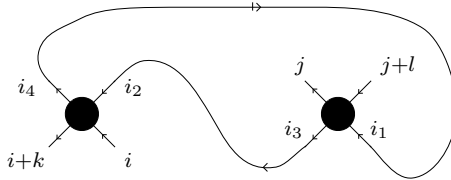
Analogous we proceed for the X-and the D-Channel and write

$$X_{j_3 j_4 j_1 j_2} = X_{j_3 j_1}^{(j_2 - j_3)(j_4 - j_1)} := X_{ji}^{lk} \quad (4.45)$$



and

$$D_{j_3 j_4 j_1 j_2} = D_{j_3 j_2}^{(j_1 - j_3)(j_4 - j_2)} := D_{ji}^{lk}, \quad (4.46)$$



with the same ranges for the indices as above. The new quantities A_{ji}^{lk} can be interpreted as block matrices, with the block structure given by the l, k indices, and the internal structure of each block given by the indices j, i . One has to keep in mind that the range of j, i depends on the value of l and k , respectively. Thus, each of this block matrices will be a quadratic matrix with an odd dimension $2L+1$ in the blocks, where the blocks become smaller when we move from the central block outside. This is illustrated in Figure fig. 4.2 for $L = N = 2$

These block matrices are actually the form of our quantities which is perfectly suited for numerical purposes. By transforming the flow equations into this representation, it

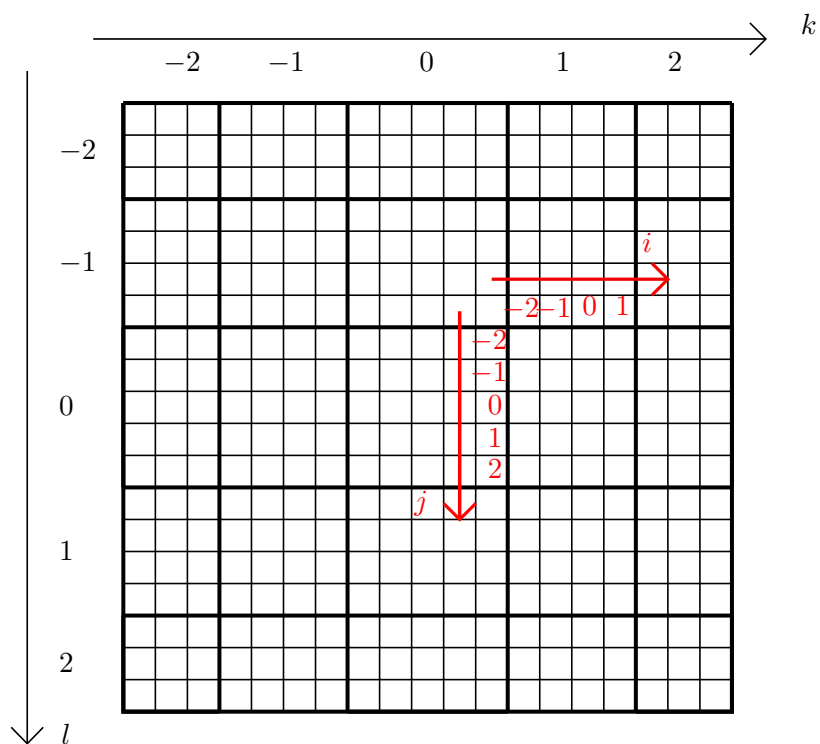


Figure 4.2.: The block matrix structure of the vertex quantities. l and k denote the free block indices, while j and i are the dependent indices within the single blocks. Note that the blocks become smaller the wider their distance to the central block is.

will turn out that their right hand sides reduce to simple matrix products in the block matrices. This actually is a crucial point. For matrix multiplications we can apply the full might of the algorithms in the linear algebra packages BLAS and LAPACK. If we just had arbitrary summations over a tensor quantity with four indices and doing them naively, this would rise the computation time by a tremendous amount.

For further use, we will state here first the vertex symmetries in the new representation, translating into symmetries of the corresponding block matrices.

$$\begin{aligned}
P_{ji}^{\sigma\sigma lk} &= P_{j(j+l)i(i+k)}^{\sigma\sigma} = P_{i(i+k)j(j+l)}^{\sigma\sigma} = P_{i(i+k)j(j+l)}^{\sigma\sigma} = P_{ij}^{\sigma\sigma kl} \\
P_{ji}^{\sigma\sigma lk} &= P_{j(j+l)i(i+k)}^{\sigma\sigma} = -P_{(j+l)ji(i+k)}^{\sigma\sigma} = -P_{(j+l)i}^{(-l)k} \\
P_{ji}^{\sigma\sigma lk} &= P_{j(j+l)i(i+k)}^{\sigma\sigma} = -P_{j(j+l)(i+k)i}^{\sigma\sigma} = -P_{j(i+k)}^{l(-k)} \\
P_{ji}^{\sigma\bar{\sigma} lk} &= P_{j(j+l)i(i+k)}^{\sigma\bar{\sigma}} = P_{i(i+k)j(j+l)}^{\sigma\bar{\sigma}} = P_{ij}^{\sigma\bar{\sigma} kl} \\
P_{ji}^{\sigma\bar{\sigma} lk} &= P_{j(j+l)i(i+k)}^{\sigma\bar{\sigma}} = P_{(j+l)j(i+k)i}^{\sigma\bar{\sigma}} = P_{(j+l)(i+k)}^{\sigma\bar{\sigma}(-l)(-k)} \\
\bar{P}_{ji}^{\sigma\bar{\sigma} lk} &= \bar{P}_{j(j+l)i(i+k)}^{\sigma\bar{\sigma}} = \bar{P}_{i(i+k)j(j+l)}^{\sigma\bar{\sigma}} = \bar{P}_{ij}^{\sigma\bar{\sigma} kl} = \bar{P}_{(i+k)i(j+l)j}^{\sigma\bar{\sigma}} = \bar{P}_{(i+k)(j+l)}^{\sigma\bar{\sigma}(-k)(-l)} \\
\bar{P}_{ji}^{\sigma\bar{\sigma} lk} &= \bar{P}_{j(j+l)i(i+k)}^{\sigma\bar{\sigma}} = \bar{P}_{(j+l)j(i+k)i}^{\sigma\bar{\sigma}} = \bar{P}_{(j+l)(i+k)}^{\sigma\bar{\sigma}(-l)(-k)} \\
P_{ji}^{\sigma\bar{\sigma} lk} &= P_{j(j+l)i(i+k)}^{\sigma\bar{\sigma}} = -\bar{P}_{(j+l)ji(i+k)}^{\sigma\bar{\sigma}} = -\bar{P}_{(j+l)i}^{\sigma\bar{\sigma}(-l)k} \\
\Rightarrow \bar{P}_{ji}^{\sigma\bar{\sigma} lk} &= \bar{P}_{j(j+l)i(i+k)}^{\sigma\bar{\sigma}} = -P_{(j+l)ji(i+k)}^{\sigma\bar{\sigma}} = -P_{(j+l)i}^{\sigma\bar{\sigma}(-l)k} \\
[P_{ji}^{\sigma\sigma lk}]^* &= P_{ji}^{\sigma\sigma lk} \\
[\bar{P}_{ji}^{\sigma\bar{\sigma} lk}]^* &= \bar{P}_{ji}^{\sigma\bar{\sigma} lk} \\
[P_{ji}^{\sigma\bar{\sigma} lk}]^* &= P_{ji}^{\sigma\bar{\sigma} lk}
\end{aligned} \tag{4.47}$$

For the X-channel

$$\begin{aligned}
X_{ji}^{\sigma\sigma lk} &= X_{j(i+k)i(j+l)}^{\sigma\sigma} = X_{i(j+l)j(i+k)}^{\sigma\sigma} = X_{ij}^{\sigma\sigma kl} \\
X_{ji}^{\sigma\bar{\sigma} lk} &= X_{j(i+k)i(j+l)}^{\sigma\bar{\sigma}} = X_{i(j+l)j(i+k)}^{\sigma\bar{\sigma}} = X_{ij}^{\sigma\bar{\sigma} kl} \\
\bar{X}_{ji}^{\sigma\bar{\sigma} lk} &= \bar{X}_{j(i+k)i(j+l)}^{\sigma\bar{\sigma}} = \bar{X}_{i(j+l)j(i+k)}^{\sigma\bar{\sigma}} = \bar{X}_{ij}^{\sigma\bar{\sigma} kl} \\
[X_{ji}^{\sigma\sigma lk}]^* &= X_{ji}^{\sigma\sigma lk} \\
[X_{ji}^{\sigma\bar{\sigma} lk}]^* &= X_{ji}^{\sigma\bar{\sigma} lk} \\
[\bar{X}_{ji}^{\sigma\bar{\sigma} lk}]^* &= \bar{X}_{ji}^{\sigma\bar{\sigma} lk} \\
X_{ji}^{\sigma\bar{\sigma} lk} &= X_{j(i+k)i(j+l)}^{\sigma\bar{\sigma}} = X_{(i+k)j(j+l)i}^{\sigma\bar{\sigma}} = X_{(j+l)(i+k)}^{\sigma\bar{\sigma}(-l)(-k)} \\
\bar{X}_{ji}^{\sigma\bar{\sigma} lk} &= \bar{X}_{j(i+k)i(j+l)}^{\sigma\bar{\sigma}} = \bar{X}_{(j+l)i(i+k)j}^{\sigma\bar{\sigma}} = \bar{X}_{(j+l)(i+k)}^{\sigma\bar{\sigma}(-l)(-k)} \\
X_{ji}^{\sigma\sigma lk} &= X_{j(i+k)i(j+l)}^{\sigma\sigma} = X_{(i+k)j(j+l)i}^{\sigma\sigma} = X_{(j+l)(i+k)}^{\sigma\sigma(-l)(-k)}
\end{aligned} \tag{4.48}$$

Connection to the D channel

$$\begin{aligned}
X_{ji}^{\sigma\sigma lk}(\chi) &= X_{j(i+k)i(j+l)}^{\sigma\sigma} = -D_{j(i+k)(j+l)i}^{\sigma\sigma} = -D_{ji}^{\sigma\sigma lk} \\
X_{ji}^{\sigma\bar{\sigma} lk} &= X_{j(i+k)i(j+l)}^{\sigma\bar{\sigma}} = -\bar{D}_{j(i+k)(j+l)i}^{\sigma\bar{\sigma}} = -\bar{D}_{ji}^{\sigma\bar{\sigma} lk} \\
\bar{X}_{ji}^{\sigma\bar{\sigma} lk} &= \bar{X}_{j(i+k)i(j+l)}^{\sigma\bar{\sigma}} = -D_{j(i+k)(j+l)i}^{\sigma\bar{\sigma}} = -D_{ji}^{\sigma\bar{\sigma} lk}
\end{aligned} \tag{4.49}$$

At the end of this chapter we have depicted these symmetries graphically.

4.7. The flow equations in the new notation

Our flow equations derived above can easily be rewritten in the new representation. The only thing we have now to take care of are the feedback terms which become slightly more complicated. We will explicitly show the transformation for $\dot{P}_{j_3 j_4 j_1 j_2}^{\sigma\sigma}$ and then simply state the results for the other flow equations.

We have

$$\begin{aligned}
\dot{P}_{ji}^{\sigma\sigma lk} &= \dot{P}_{j(j+l)i(i+k)}^{\sigma\sigma} \\
&= T \left\{ \nu(j\sigma, j+l\sigma; i_3\sigma, i_4\sigma) + P_{j(j+l)i_3 i_4}^{\sigma\sigma} - D_{j(j+l)i_4 i_3}^{\sigma\sigma} + D_{j(j+l)i_3 i_4}^{\sigma\sigma} \right\} \\
&\quad \sum_{\omega_n''} S_{i_3 i_1}^{\sigma\Lambda} (\Pi - \omega_n'') \mathcal{G}_{i_4 i_2}^{\sigma\Lambda} (\omega_n'') \\
&\quad \left\{ \nu(i_1\sigma, i_2\sigma; i\sigma, (i+k)\sigma) + P_{i_1 i_2 i(i+k)}^{\sigma\sigma} - D_{i_1 i_2 (i+k)i}^{\sigma\sigma} + D_{i_1 i_2 i(i+k)}^{\sigma\sigma} \right\} \\
&= T \left\{ \nu(j\sigma, j+l\sigma; i_3\sigma, i_4\sigma) + P_{j i_3}^{\sigma\sigma l(i_4-i_3)} - D_{j i_3}^{\sigma\sigma (i_4-j)(j+l-i_3)} + D_{j i_4}^{\sigma\sigma (i_3-j)(j+l-i_4)} \right\} \\
&\quad \sum_{\omega_n''} S_{i_3 i_1}^{\sigma\Lambda} (\Pi - \omega_n'') \mathcal{G}_{i_4 i_2}^{\sigma\Lambda} (\omega_n'') \\
&\quad \left\{ \nu(i_1\sigma, i_2\sigma; i\sigma, (i+k)\sigma) + P_{i_1 i}^{\sigma\sigma (i_2-i_1)k} - D_{i_1 i}^{\sigma\sigma (i+k-i_1)(i_2-i)} + D_{i_1 (i+k)}^{\sigma\sigma (i-i_1)(i_2-(i+k))} \right\} \\
&= T \left\{ \nu(j\sigma, j+l\sigma; i_3\sigma, i_3+p\sigma) + P_{j i_3}^{\sigma\sigma lp} - D_{j i_3}^{\sigma\sigma (i_3+p-j)(j+l-i_3)} + D_{j (i_3+p)}^{\sigma\sigma (i_3-j)(j+l-(i_3+p))} \right\} \\
&\quad \sum_{\omega_n''} [S_{i_3 i_1}^{\sigma\Lambda} (\Pi - \omega_n'') \mathcal{G}_{i_3+p, i_1+q}^{\sigma\Lambda} (\omega_n'')] \\
&\quad \left\{ \nu(i_1\sigma, i_1+q\sigma; i\sigma, (i+k)\sigma) + P_{i_1 i}^{qk} - D_{i_1 i}^{\sigma\sigma (i+k-i_1)(i_1+q-i)} + D_{i_1 (i+k)}^{\sigma\sigma (i-i_1)(i_1+q-(i+k))} \right\}, \tag{4.50}
\end{aligned}$$

where the sums over the internal variables have the ranges

$$\begin{aligned}
-L &\leq p, q \leq L \\
\max(-N, -N-p) &\leq i_3 \leq \min(N, N-p) \\
\max(-N, -N-q) &\leq i_1 \leq \min(N, N-q)
\end{aligned} \tag{4.51}$$

and it is understood implicitly that any quantity A_{ji}^{lk} is zero if any of the indices is out of the appropriate range $-L \leq l, k \leq L$, $\max(-N, -N-l) \leq j \leq \min(N, N-l)$ and $\max(-N, -N-k) \leq i \leq \min(N, N-k)$.

At this point, we note that with the definitions

$$\begin{aligned}
{}_1 P_{ji}^{\sigma\sigma lk} &:= \left\{ \nu(j\sigma, j+l\sigma; i\sigma, i+k\sigma) + P_{ji}^{\sigma\sigma lk} - D_{ji}^{\sigma\sigma (i+k-j)(j+l-i)} \right. \\
&\quad \left. + D^{\sigma\sigma (i-j)(j+l-(i+k))} j(i+k) \right\} \\
W_{ji}^{\sigma\sigma pq} &:= T \sum_{\omega_n''} [S_{ji}^{\sigma\sigma pq} (\Pi - \omega_n'') \mathcal{G}_{i_3+p, i_1+q}^{\sigma\Lambda} (\omega_n'')]
\end{aligned} \tag{4.52}$$

we can write this in the form

$$\dot{P}_{ji}^{\sigma\sigma lk} = {}_1P_{j i_3}^{\sigma\sigma lp} \cdot W_{i_3 i_1}^{pq} \cdot {}_1P_{i_1 i}^{\sigma\sigma qk}. \quad (4.53)$$

That is just the product form in the block matrix space which we mentioned above. Analogously one can proceed for the other flow equations. Here, we need the definitions:

$$\begin{aligned} {}_1P_{ji}^{\sigma\sigma lk} &:= \nu(j\sigma, j+l\sigma; i\sigma, i+k\sigma) + P_{j i_3}^{\sigma\sigma lk} - D_{ji}^{\sigma\sigma(i+k-j)(j+l-i)} + D_{j(i+k)}^{\sigma\sigma(i-j)(j+l-(i+k))} \\ {}_1P_{ji}^{\sigma\bar{\sigma} lk} &:= \nu(j\sigma, j+l\bar{\sigma}; i\sigma(i+k)\bar{\sigma}) + P_{ji}^{\sigma\bar{\sigma} lk} + X_{ji}^{\sigma\bar{\sigma}(i+k-j)(j+l-i)} - \bar{X}_{j(i+k)}^{\sigma\bar{\sigma}(i-j)(j+l-(i+k))} \\ {}_1X_{ji}^{\sigma\bar{\sigma} lk} &:= \nu(j\sigma, (i+k)\bar{\sigma}; i\sigma, (j+l)\bar{\sigma}) + X_{ji}^{\sigma\bar{\sigma} lk} + P_{ji}^{\sigma\bar{\sigma}(i+k-j)(j+l-i)} - \bar{X}_{j(j+l)}^{\sigma\bar{\sigma}(i-j)(i+k-(j+l))} \\ {}_1\bar{X}_{ji}^{\sigma\bar{\sigma} lk} &:= \nu(j\sigma, (i+k)\sigma; i\sigma, (j+l)\sigma) - D_{ji}^{\sigma\sigma lk} + P_{ji}^{\sigma\sigma(i+k-j)(j+l-i)} + D_{j(j+l)}^{\sigma\sigma(i-j)(i+k-(j+l))} \\ {}_2\bar{X}_{ji}^{\sigma\bar{\sigma} lk} &:= \nu(j\sigma, (i+k)\bar{\sigma}; i\bar{\sigma}, (j+l)\sigma) + \bar{X}_{ji}^{\sigma\bar{\sigma} lk} - P_{j(j+l)}^{\sigma\bar{\sigma}(i+k-j)(i-(j+l))} - X_{j(j+l)}^{\sigma\bar{\sigma}(i-j)(i+k-(j+l))} \\ {}_3\bar{X}_{ji}^{\sigma\bar{\sigma} lk} &:= \nu(j\bar{\sigma}, (i+k)\bar{\sigma}; i\bar{\sigma}, (j+l)\bar{\sigma}) - D_{ji}^{\bar{\sigma}\bar{\sigma} lk} + P_{ji}^{\bar{\sigma}\bar{\sigma}(i+k-j)(i-(j+l))} + D_{j(j+l)}^{\bar{\sigma}\bar{\sigma}(i-j)(i+k-(j+l))} \\ {}_1D_{ji}^{\sigma\sigma lk} &:= \nu(j\sigma, (i+k)\sigma; (j+l)\sigma, i\sigma) + D_{ji}^{\sigma\sigma lk} + P_{j(j+l)}^{\sigma\sigma(i+k-j)(i-(j+l))} - D_{j(j+l)}^{\sigma\sigma(i-j)(i+k-(j+l))} \\ {}_2D_{ji}^{\sigma\sigma lk} &:= \nu(j\sigma, (i+k)\bar{\sigma}; (j+l)\sigma, i\bar{\sigma}) - \bar{X}_{ji}^{\sigma\bar{\sigma} lk} + P_{j(j+l)}^{\sigma\bar{\sigma}(i+k-j)(i-(j+l))} + X_{j(j+l)}^{\sigma\bar{\sigma}(j+l-(i+k))(j-i)}. \end{aligned} \quad (4.54)$$

Furthermore, we define the bubbles

$$\begin{aligned} \Pi_{ji}^{\sigma\mu lk} &:= T \sum_{\omega_n''} [\mathcal{S}_{ji}^{\sigma\Lambda} (\Pi - \omega_n'') \mathcal{G}_{(j+l)(i+k)}^{\mu\Lambda}(\omega_n'')] \\ \chi_{ji}^{\sigma\mu lk} &:= T \sum_{\omega_n''} [\mathcal{S}_{ji}^{\sigma\Lambda} (X + \omega_n'') \mathcal{G}_{(j+l)(i+k)}^{\mu\Lambda}(\omega_n'') + \mathcal{S} \leftrightarrow \mathcal{G}] \end{aligned} \quad (4.55)$$

and then we can cast the flow equations into the simple form

$$\begin{aligned} \dot{P}_{ji}^{\sigma\sigma lk} &= {}_1P_{j i_1}^{\sigma\sigma lp} \cdot \Pi_{i_1 i_2}^{\sigma\sigma pq} \cdot {}_1P_{i_2 i}^{\sigma\sigma qk} \\ \dot{P}_{ji}^{\sigma\bar{\sigma} lk} &= {}_2\cdot {}_1P_{j i_1}^{\sigma\bar{\sigma} lp} \cdot \Pi_{i_1 i_2}^{\sigma\bar{\sigma} pq} \cdot {}_1P_{i_2 i}^{\sigma\bar{\sigma} qk} \\ \dot{X}_{ji}^{\sigma\bar{\sigma} lk} &= {}_1X_{j i_1}^{\sigma\bar{\sigma} lp} \cdot \chi_{i_1 i_2}^{\sigma\bar{\sigma} pq} \cdot {}_1X_{i_2 i}^{\sigma\bar{\sigma} qk} \\ \dot{\bar{X}}_{ji}^{\sigma\bar{\sigma} lk} &= {}_1\bar{X}_{j i_1}^{\sigma\bar{\sigma} lp} \cdot \chi_{i_1 i_2}^{\sigma\sigma pq} \cdot {}_2\bar{X}_{i_2 i}^{\sigma\bar{\sigma} qk} + {}_2\bar{X}_{j i_1}^{\sigma\bar{\sigma} lp} \cdot \chi_{i_1 i_2}^{\bar{\sigma}\bar{\sigma} pq} \cdot {}_3\bar{X}_{i_2 i}^{\bar{\sigma}\bar{\sigma} qk} \\ \dot{D}_{ji}^{\sigma\sigma lk} &= -{}_1D_{j i_1}^{\sigma\sigma lp} \cdot \chi_{i_1 i_2}^{\sigma\sigma pq} \cdot {}_1D_{i_2 i}^{\sigma\sigma qk} - {}_2D_{j i_1}^{\sigma\bar{\sigma} lp} \cdot \chi_{i_1 i_2}^{\bar{\sigma}\bar{\sigma} pq} \cdot {}_2D_{i_2 i}^{\sigma\bar{\sigma} qk} \end{aligned} \quad (4.56)$$

and the flow of the self energy reads

$$\begin{aligned} \dot{\gamma}_{ji}^{\Lambda\sigma} &= \Gamma_{(i-p)(j-q)}^{\sigma\Lambda} (\nu((j-q)\sigma, j\sigma; (i-p)\sigma, i\sigma) + P_{(j-q)(i-p)}^{\sigma\sigma qp}) \\ &\quad - \Gamma_{(j-q)(i-p)}^{\sigma\Lambda} D_{(i-p)(j-q)}^{\sigma\sigma pq} \\ &\quad + \Gamma_{i_1(i_1-p)}^{\sigma\Lambda} D_{(i_1-p)i}^{\sigma\sigma p(j-i)} \\ &\quad + \Gamma_{(i+p)(j+q)}^{\bar{\sigma}\Lambda} (\nu((j+q)\bar{\sigma}, j\sigma; (i+p)\bar{\sigma}, i\sigma) + P_{ji}^{\sigma\bar{\sigma} qp}) \\ &\quad + \Gamma_{(j-q)(i-p)}^{\bar{\sigma}\Lambda} X_{ji}^{\bar{\sigma}\bar{\sigma}(-q)(-p)} \\ &\quad - \Gamma_{i_1(i_1-p)}^{\bar{\sigma}\Lambda} \bar{X}_{i(i_1-p)}^{\bar{\sigma}\bar{\sigma}(j-i)p}, \end{aligned} \quad (4.57)$$

where

$$\Gamma_{ij}^{\sigma\Lambda} := T \sum_{\omega_n''} \mathcal{S}_{ij}^{\sigma\Lambda}(\omega_n''). \quad (4.58)$$

After having set up the flow equations, we can tackle the internal frequency summations over ω_n'' . Here we will finally make the transition to the zero temperature limit, i.e the Matsubara frequencies will become dense and we can replace the summation over them by an integral. In this context, we will also have to specify the concrete form of the cutoff in our non interacting propagator which introduces the flow parameter. We will use ²

$$\mathcal{G}(i\omega_n, \Lambda) = \theta_T(|\omega_n| - \Lambda) \mathcal{G}^0(i\omega_n). \quad (4.59)$$

This immediately determines the single scale propagator

$$\begin{aligned} \mathcal{S}(\omega_n, \Lambda) &= \mathcal{G}^\Lambda(\omega_n) \partial_\Lambda [\mathcal{G}^{0\Lambda}(\omega_n)]^{-1} \mathcal{G}^\Lambda(\omega_n) = \\ &= \frac{\mathcal{G}^0 \theta_T (|\omega_n| - \Lambda)}{1 + \mathcal{G}^0 \theta_T (|\omega_n| - \Lambda) \gamma_1} [\mathcal{G}^0 \theta_T]^{-1} \mathcal{G} \delta_T (|\omega_n| - \Lambda) [\mathcal{G}^0 \theta_T]^{-1} \frac{\mathcal{G}^0 \theta_T}{1 + \mathcal{G}^0 \theta_T \gamma_1} = \\ &= \frac{\mathcal{G}^0 \delta_T (|\omega_n| - \Lambda)}{(1 + \mathcal{G}^0 \theta_T \gamma_1)^2} = \\ &= \delta_T \partial_{\theta_T} \left[\frac{\mathcal{G}^0 \theta_T}{1 + \mathcal{G}^0 \theta_T \gamma_1} \right] = \\ &= \delta_T (|\omega_n| - \Lambda) \partial_{\theta_T} \mathcal{G}^\Lambda(\omega_n). \end{aligned} \quad (4.60)$$

At this point, the name "single scale" propagator becomes apparent since due to the δ -function \mathcal{S} depends only on the Λ scale and not on the frequency ω_n . As mentioned above, we will take the zero temperature limit and make therefore the replacement $T \sum_{\omega_n} \rightarrow \frac{1}{2\pi} \int d\omega$. With this we can calculate the bubbles $\Pi_{ji}^{\sigma\mu lk}$, $\chi_{ji}^{\sigma\mu lk}$ as well as $\Gamma_{ij}^{\sigma\Lambda}$. Let's start with

$$\sum_{\omega_n} \Gamma_{ij}^{\sigma\Lambda}(\omega_n) = \sum_{\omega_n} T \mathcal{S}_{ij}^{\sigma\Lambda}(\omega_n) = \frac{1}{2\pi} \int d\omega \delta(|\omega| - \Lambda) \partial_\theta \mathcal{G}^\Lambda(i\omega) \quad (4.61)$$

in the evaluation of the ω integral, the product of the δ -function and the function $\partial_\theta \mathcal{G}^\Lambda(i\omega)$ must be treated carefully. For this purpose, we will exploit Morris' lemma [22] which basically states that

$$\lim_{\epsilon \rightarrow 0} \delta_\epsilon(x - \Lambda) f[\theta_\epsilon(x - \Lambda)] = \delta(x - \Lambda) \int_0^1 f(t) dt, \quad (4.62)$$

where f is a continuous function in θ and the δ - as well as the θ -function are implemented

² $\theta_T(\omega)$ denotes a step function which is broadened on a scale set by T

via a convergent sequences $\delta_\epsilon \rightarrow \delta$ and $\theta_\epsilon \rightarrow \theta$. Thus, we get

$$\begin{aligned}
\sum_{\omega_n} \Gamma_{ij}^{\sigma\Lambda}(\omega_n) &= \frac{1}{2\pi} \int d\omega \delta(|\omega| - \Lambda) \partial_\theta \mathcal{G}_{ij}^\Lambda(i\omega) = \frac{1}{2\pi} \int d\omega \delta(|\omega| - \Lambda) \int_0^1 \partial_t \mathcal{G}_{ij}^\Lambda(i\omega) \\
&= \frac{1}{2\pi} \int d\omega \delta(|\omega| - \Lambda) \int_0^1 \partial_t \left[\frac{\mathcal{G}^0 t}{1 + \mathcal{G}^0 t \gamma_1} \right]_{ij} = \frac{1}{2\pi} \int d\omega \delta(|\omega| - \Lambda) \left[\frac{\mathcal{G}^0}{1 + \mathcal{G}^0 \gamma_1} \right]_{ij} \\
&= \frac{1}{2\pi} \sum_{\omega=\pm\Lambda} \tilde{\mathcal{G}}_{ij}^\Lambda(i\omega),
\end{aligned} \tag{4.63}$$

where we have defined

$$\tilde{\mathcal{G}}(\Lambda) =: \frac{1}{[\mathcal{G}^0]^{-1}(\Lambda) + \gamma_1^\Lambda(\Lambda)}. \tag{4.64}$$

According to the symmetries $\mathcal{G}^0(i\omega) = \mathcal{G}^0(-i\omega)^*$ and $\gamma_1^\Lambda(\Lambda) = \gamma_1^\Lambda(-\Lambda)^*$ (see (4.33)), we end up with

$$\sum_{\omega_n} \Gamma_{ij}^{\sigma\Lambda}(\omega_n) = \frac{1}{\pi} \text{Re} \tilde{\mathcal{G}}^\Lambda(i\Lambda). \tag{4.65}$$

We can do an analogous calculation to evaluate the ω_n'' sum in the bubble-terms. For this we first notice that due to the symmetries of $P_{ji}^{\sigma\sigma lk}$ we have

$$\begin{aligned}
\dot{P}_{ji}^{\sigma\sigma lk} &= {}_1P_{ji_1}^{\sigma\sigma lp} \cdot \Pi_{i_1 i_2}^{\sigma\sigma pq} \cdot {}_1P_{i_2 i}^{\sigma\sigma qk} \\
&= \frac{1}{2} {}_1P_{ji_1}^{\sigma\sigma lp} \cdot \Pi_{i_1 i_2}^{\sigma\sigma pq} \cdot {}_1P_{i_2 i}^{\sigma\sigma qk} + \frac{1}{2} {}_1P_{j(i_1+p)}^{l(-p)} \Pi_{(i_1+p)(i_2+q)}^{(-p)(-q)} {}_1P_{(i_2+q)i}^{(-q)k} \\
&= {}_1P_{ji_1}^{\sigma\sigma lp} \frac{1}{2} [\Pi_{i_1 i_2}^{\sigma\sigma pq} + \Pi_{(i_1+p)(i_2+q)}^{(-p)(-q)}] {}_1P_{i_2 i}^{qk}.
\end{aligned} \tag{4.66}$$

Thus, we see that we can actually make the replacement

$$\Pi_{ji}^{\sigma\mu lk} \rightarrow \tilde{\Pi}_{ji}^{\sigma\mu lk} := \frac{1}{2} [\Pi_{i_1 i_2}^{\sigma\sigma pq} + \Pi_{(i_1+p)(i_2+q)}^{(-p)(-q)}] \tag{4.67}$$

in the flow equations for the p-channel. Therefore, if we evaluate the frequency sum over ω_n'' in (4.56), we get

$$\sum_{\omega_n} \tilde{\Pi}_{ji}^{\sigma\mu lk} = T \sum_{\omega_n} \frac{1}{2} [\mathcal{S}_{ji}^\sigma(-\omega_n'') \mathcal{G}_{(j+l)(i+k)}^\mu(\omega_n'') + \mathcal{S}_{(j+l)(i+k)}^\sigma(-\omega_n'') \mathcal{G}_{ji}^\mu(\omega_n'')], \tag{4.68}$$

which then can again be evaluated via Morris' lemma:

$$\begin{aligned}
\sum_{i\omega_n} \tilde{\Pi}_{ji}^{\sigma\mu lk} &= \frac{1}{4\pi} \int d\omega \delta(|\omega| - \Lambda) \int_0^1 dt \left\{ \partial_t [\mathcal{G}_{ji}^{\sigma\Lambda}(-i\omega)] \mathcal{G}_{(j+l)(i+k)}(i\omega) \right. \\
&\quad \left. + \partial_t [\mathcal{G}_{(j+l)(i+k)}^{\sigma\Lambda}(-i\omega)] \mathcal{G}_{ji}^{\mu\Lambda}(i\omega) \right\} = \\
&= \frac{1}{4\pi} \int d\omega \delta(|\omega| - \Lambda) \int_0^1 dt \partial_t [\mathcal{G}_{ji}^{\sigma\Lambda}(i\omega) \mathcal{G}_{(j+l)(i+k)}^{\sigma\Lambda}(-i\omega)] = \\
&= \frac{1}{4\pi} \int d\omega \delta(|\omega| - \Lambda) \tilde{\mathcal{G}}_{ji}^{\sigma\Lambda}(i\omega) \tilde{\mathcal{G}}_{(j+l)(i+k)}^{\mu\Lambda}(-i\omega) = \\
&= \frac{1}{4\pi} \sum_{\omega=\pm\Lambda} \tilde{\mathcal{G}}_{ji}^{\sigma\Lambda}(i\omega) \tilde{\mathcal{G}}_{(j+l)(i+k)}^{\mu\Lambda}(-i\omega) = \\
&= \frac{1}{2\pi} \operatorname{Re} \left[\tilde{\mathcal{G}}_{ji}^{\sigma\Lambda}(i\Lambda) \tilde{\mathcal{G}}_{(j+l)(i+k)}^{\mu\Lambda}(-i\Lambda) \right].
\end{aligned} \tag{4.69}$$

Completely analogous we can proceed for the second bubble

$$\sum_{\omega_n} \chi_{ji}^{\sigma\mu lk} = T[\mathcal{S}_{ji}^{\sigma\Lambda}(\omega_n'') \mathcal{G}_{(j+l)(i+k)}^{\mu\Lambda}(\omega_n'') + \mathcal{S}_{(j+l)(i+k)}^{\mu\Lambda}(\omega_n'') \mathcal{G}_{ji}^{\sigma\Lambda}(\omega_n'')] \tag{4.70}$$

which yields

$$\sum_{i\omega_n} \chi_{ji}^{\sigma\mu lk} = \frac{1}{\pi} \operatorname{Re} \left[\tilde{\mathcal{G}}_{ji}^{\sigma\Lambda}(i\Lambda) \tilde{\mathcal{G}}_{(j+l)(i+k)}^{\mu\Lambda}(i\Lambda) \right]. \tag{4.71}$$

With these statements plugged in (4.56), we have reached the final form of our flow equations which is simply a system of ordinary differential equations.

The last part in this rather technical section concerns the numerical initial conditions of the flow. In our analytical considerations, the initial conditions were simple, namely $\gamma_1^{\Lambda_{init}=\infty} = 0$ and $\gamma_2^{\Lambda_{init}=\infty} = \nu$. However, when we implement the flow on a computer, $\Lambda_{init} = \infty$ is not accessible and is morally replaced by $\Lambda_{init} = \Lambda_0$, where Λ_0 is chosen to be large in terms of our energy unit τ . This replacement will give rise to a change in the initial conditions in the flow of γ_1^Λ . To compute this contribution, it is convenient to use not our numerical form 4.57 but the more compact form 4.42. If we express the latter in the notation introduced above, we have

$$\dot{\gamma}_{1ji}^{\Lambda\sigma} = \frac{1}{\pi} \operatorname{Re} [\tilde{\mathcal{G}}(i\Lambda)]_{kl} \gamma_2^\Lambda(l\mu, j\sigma; k\mu, i\sigma). \tag{4.72}$$

Now one can integrate this equation from Λ_0 to ∞ and consider the limit $\Lambda_0 \rightarrow \infty$

$$\begin{aligned}
\lim_{\Lambda_0 \rightarrow \infty} \int_{\Lambda_0}^{\infty} \dot{\gamma}_{1ji}^{\Lambda_0 \sigma} &= \frac{1}{\pi} \lim_{\Lambda_0 \rightarrow \infty} \int_{\Lambda_0}^{\infty} \operatorname{Re}[e^{i\Lambda_0^+} \tilde{\mathcal{G}}(i\Lambda)]_{kl} \gamma_2^{\Lambda}(l\mu, j\sigma; k\mu, i\sigma) \\
\Rightarrow \underbrace{\gamma_{1ji}^{\infty \sigma}}_{=0} - \gamma_{1ji}^{\Lambda_0 \sigma} &= \frac{1}{\pi} \lim_{\Lambda_0 \rightarrow \infty} \int_{\Lambda_0}^{\infty} \operatorname{Re} \left[e^{i\Lambda_0^+} \frac{\delta_{lk}}{i\Lambda} \right] \nu(l\mu, j\sigma; k\mu, i\sigma) \\
&= \frac{1}{\pi} \lim_{\Lambda_0 \rightarrow \infty} \int_{\Lambda_0}^{\infty} \left[\frac{\sin(\Lambda 0^+)}{\Lambda} \right] \nu(l\mu, j\sigma; l\mu, i\sigma) \\
&= \frac{1}{\pi} \lim_{\Lambda_0 \rightarrow \infty} \left[\underbrace{\int_0^{\infty} d\Lambda \left[\frac{\sin(\Lambda 0^+)}{\Lambda} \right]}_{=\frac{\pi}{2}} - \underbrace{\int_0^{\Lambda_0} d\Lambda \left[\frac{\sin(\Lambda 0^+)}{\Lambda} \right]}_{=0} \right] \nu(l\mu, j\sigma; k\mu, i\sigma) \\
&= \frac{1}{\pi} \lim_{\Lambda_0 \rightarrow \infty} \frac{\pi}{2} \nu(l\mu, j\sigma; l\mu, i\sigma).
\end{aligned} \tag{4.73}$$

In the second line we used $\lim_{\Lambda \rightarrow \infty} \gamma_2^{\Lambda} \rightarrow \nu$ and that for large Λ the leading order of Λ in $\tilde{\mathcal{G}}_{lk}^{\mu}(i\Lambda)$ is proportional to $\frac{\delta_{lk}}{i\Lambda}$. Thus, we end up with the numerical initial conditions for our flow equations:

$$\begin{aligned}
\gamma_{1ji}^{\Lambda_0 \sigma} &= -\frac{1}{2} \nu(l\mu, j\sigma; l\mu, i\sigma) \\
\gamma_2^{\Lambda_0}(j_3\sigma_3, j_4\sigma_4; j_1\sigma_1, j_2\sigma_2) &= \nu(j_3\sigma_3, j_4\sigma_4; j_1\sigma_1, j_2\sigma_2).
\end{aligned} \tag{4.74}$$

For the concrete solution of these differential equations, we apply a fourth order Runge Kutta method with adaptive step size using the Dormand-Prince Butchers tableau [23]. Again, we emphasize that the r.h.s. in the differential equation is given by a matrix product in block matrix space.

Note that in our actual calculations we will always use a potential which is parity symmetric, i.e. $V_i = V_{-i}$ for all sites i . This leads to the fact that our whole system is invariant under parity, i.e. we cannot distinguish between left and right. Therefore, we have for our propagators

$$\mathcal{G}_{ij} = \mathcal{G}_{(-i)(-j)}, \quad \mathcal{S}_{ij} = \mathcal{S}_{(-i)(-j)} \tag{4.75}$$

and for an arbitrary of our vertex quantities A_{ji}^{lk} :

$$A_{ji}^{lk} = A_{(-j)(-i)}^{(-l)(-k)} \text{ or } A_{j_3 j_4 j_1 j_2} = A_{(-j_3)(-j_4)(-j_1)(-j_2)}, \tag{4.76}$$

respectively. Using this together with the symmetries established earlier, we can reduce our needed memory significantly by only saving the independent quantities. Furthermore, we can also reduce computation time by transforming A_{ji}^{lk} into an odd-even representation according to

$$\tilde{A} := W^T \cdot A \cdot W, \tag{4.77}$$

goes like $2 \cdot \left(\frac{N_{ges}}{2}\right)^3 = \frac{1}{4}N_{ges}^3$.

Thus, by exploiting parity symmetry we can reduce the leading order term in computation time to a quarter.

As completion of this chapter, we will graphically depict the independent elements in the block matrices of our channels, using all the previous stated symmetries as well as parity. Here we consider the $L = 2$, $N = 2$ case. Then the seven independent vertex quantities $P^{\sigma\sigma}$, $P^{\uparrow\downarrow}$, $X^{\uparrow\downarrow}$, $\bar{X}^{\uparrow\downarrow}$, $D^{\sigma\sigma}$ are of the forms depicted in the subsequent figures.

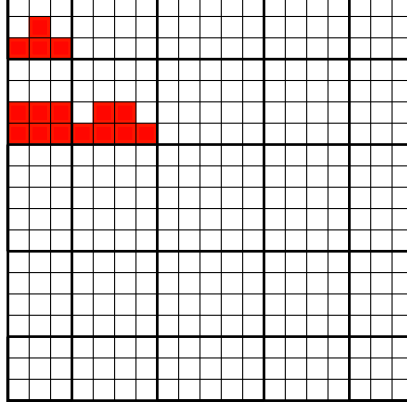


Figure 4.3.: The independent elements of the $P^{\sigma\sigma}$ channel. The relevant symmetries are here: $P_{ji}^{\sigma\sigma lk} = P_{(-j)(-i)}^{\sigma\sigma(-l)(-k)}$, $P_{ji}^{\sigma\sigma lk} = P_{ij}^{\sigma\sigma kl}$, $P_{ji}^{\sigma\sigma lk} = P_{(j+l)(i+k)}^{\sigma\sigma(-l)(-k)}$, $P_{ji}^{\sigma\sigma lk} = -P_{(j+l)i}^{\sigma\sigma(-l)k}$, and $P_{ji}^{\sigma\sigma lk} = -P_{j(i+k)}^{\sigma\sigma lk}$.

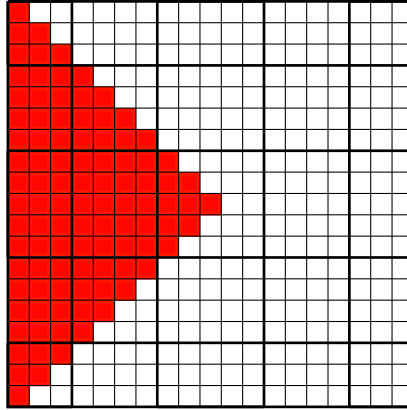


Figure 4.4.: The independent elements of the $P^{\uparrow\downarrow}$ and $X^{\uparrow\downarrow}$ channels. The relevant symmetries are here ($A = X, P$): $A_{ji}^{\uparrow\downarrow lk} = A_{(-j)(-i)}^{\uparrow\downarrow(-l)(-k)}$ and $A_{ji}^{\uparrow\downarrow lk} = A_{ij}^{\uparrow\downarrow kl}$.

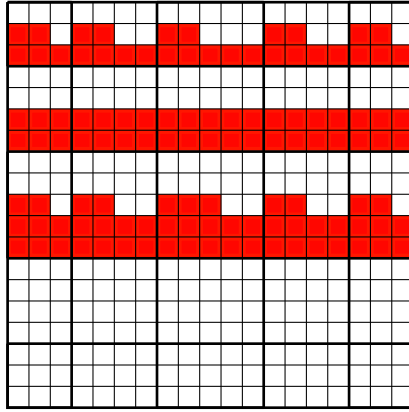


Figure 4.5.: The independent elements of the $\bar{X}^{\uparrow\downarrow}$ channel. The relevant symmetries are here: $\bar{X}_{ji}^{\uparrow\downarrow lk} = \bar{X}_{(-j)(-i)}^{\uparrow\downarrow(-l)(-k)}$ and $\bar{X}_{ji}^{\uparrow\downarrow lk} = \bar{X}_{(j+l)(i+k)}^{\uparrow\downarrow(-l)(-k)}$.

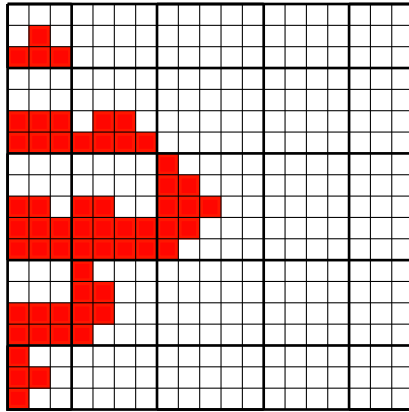


Figure 4.6.: The independent elements of the $D^{\sigma\sigma}$ channel. The relevant symmetries are here: $D_{ji}^{\sigma\sigma lk} = D_{(-j)(-i)}^{\sigma\sigma(-l)(-k)}$, $D_{ji}^{\sigma\sigma lk} = D_{ij}^{\sigma\sigma kl}$, and $D_{ji}^{\sigma\sigma lk} = D_{(j+l)(i+k)}^{\sigma\sigma(-l)(-k)}$.

In the next chapters, we will use our developed machinery to study various problems around QPCs and Quantum Dots (QDs).

5. A brief revision of the physics in quantum point contacts

In this chapter, we will continue with the explanation of physics in QPCs. In our second chapter on the experimental realization of QPCs, we have already commented on the general conductance quantization that occurs when varying the gate voltage and therefore the barrier structure of the QPC. In the following, we will just study the behavior of the lowest sub-band, i.e. the transition from a closed QPC to an open one with $G = 1 \cdot G_Q$ in terms of the conductance quantum $G_Q = \frac{2e^2}{h}$. Thus, let us look again at our model (3.8).

First, we will have to specify our potential $E_j = (V_j - \mu - \frac{\sigma B}{2})$ as well as the interaction $U(k, l)$. In this section we summarize the results Bauer et al. have obtained, using a potential barrier parabolic around the QPC's maximum

$$V(x) \simeq V_g + \mu + 2\tau - \frac{m}{2\hbar^2} \Omega_x^2 x^2 \quad (5.1)$$

or in a discrete version

$$V_j \simeq V_g + \mu + 2\tau - \frac{\Omega_x^2}{4\tau} j^2. \quad (5.2)$$

For our actual computations we used a barrier of the form below which satisfies these requirements:

$$V(j) = (\mu + V_g + 2\tau) \exp\left(-\frac{\left(\frac{j}{N}\right)^2}{\left(1 - \left(\frac{j}{N}\right)^2\right)}\right). \quad (5.3)$$

In order to determine the curvature we use

$$V(j) \approx (\mu + V_g + 2\tau) \left(1 - \left(\frac{j}{N}\right)^2\right) \quad (5.4)$$

and by comparing this with (5.2) and assuming $(V_g + \mu + 2\tau) \approx 2\tau + \mu$, we immediately obtain for the approximate curvature

$$\Omega_x = \tau \cdot \frac{2\sqrt{2}}{N}, \quad (5.5)$$

where $2N + 1$ gives the length of the interacting region. For $U(k, l)$ we will assume here a simple on-site interaction $U(k, l) \sim U_k \delta_{kl}$. To get a grasp of the physics, let us study the non interacting behavior first. We begin with determining the characteristic scales of

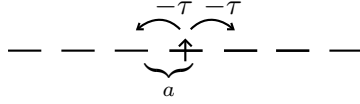


Figure 5.1.: Tight binding chain with hopping amplitude $-\tau$ and lattice spacing a

our problem. The time independent Schrödinger equation of the non-interacting single particle system is

$$\left(-\frac{\hbar^2}{2m} \frac{d^2}{dx^2} + V_g + 2\tau + \mu - \frac{m}{2\hbar^2} \Omega_x^2 x^2 \right) \psi(x) = E\psi(x). \quad (5.6)$$

In order to end up with a dimensionless equation we have to rescale x , via $\chi := \frac{x}{l_x}$. Then we obtain

$$\begin{aligned} & \left(-\frac{\hbar^2}{2m} \frac{1}{l_x^2} \frac{d^2}{d\chi^2} + V_g + \mu + 2\tau - \frac{m}{2\hbar^2} \Omega_x^2 l_x^2 \chi^2 \right) \underbrace{\psi(l_x \chi)}_{=:\tilde{\psi}(\chi)} = E\psi(l_x \cdot \chi) \\ \Rightarrow & \left(-\frac{d}{d\chi^2} + (V_g + \mu + 2\tau) \cdot \frac{2m}{\hbar^2} l_x^2 - \frac{m^2}{\hbar^4} \Omega_x^2 l_x^4 \chi^2 \right) \tilde{\psi}(\chi) = \frac{E}{\hbar^2} \tilde{\psi}(\chi) \end{aligned} \quad (5.7)$$

Now we demand $\frac{m^2}{\hbar^4} \Omega_x^2 l_x^4 \stackrel{!}{=} 1$ and thus $l_x = \frac{\hbar}{\sqrt{m\Omega_x}} = \sqrt{2} \cdot a \cdot \sqrt{\frac{\tau}{\Omega_x}}$, with the mass $m = \frac{\hbar^2}{2\tau a^2}$ (see (3.5)) and

$$\left(-\frac{d}{d\chi^2} - \chi^2 + (V_g + \mu + 2\tau) \cdot \frac{2}{\Omega_x} \right) \tilde{\psi}(\chi) = 2 \frac{E}{\Omega_x} \tilde{\psi}(\chi). \quad (5.8)$$

Thus, the natural scale of energy is given by the curvature Ω_x and the natural scale of length by $l_x \sim a \sqrt{\frac{\tau}{\Omega_x}}$. Let us now analyze our model by recreating it step by step, starting from a tight binding chain (see Figure 5.1).

The local density of states (LDOS) can easily be calculated

$$\mathcal{A}(\omega) = -\frac{1}{a\pi} \text{Im} \mathcal{G}_{jj}(\omega + i0^+) = \frac{1}{\pi a \sqrt{\omega(4\tau - \omega)}} \stackrel{\omega \ll \tau}{\approx} \frac{1}{2\pi a \sqrt{\tau\omega}} \propto \frac{1}{v_{clas}}, \quad (5.9)$$

where the last proportionality to the inverse of the electron velocity is understood in semiclassical terms via

$$\omega = \frac{1}{2} m v^2 = \frac{1}{2} \frac{\hbar^2}{2\tau a^2} v^2 \Rightarrow v^2 = \frac{4\omega\tau a^2}{\hbar^2} \quad (5.10)$$

and therefore $v \sim a \sqrt{\tau\omega}$. This LDOS has the form depicted in Figure fig. 5.2 with an $\sim \frac{1}{\sqrt{\omega}}$ van Hove singularity at the band edges. These are just determined by the usual dispersion relation of a tight binding chain

$$\epsilon_k = -2\tau \cos(ka) \quad (5.11)$$

to be -2τ , 2τ , respectively. Our total band width is thus 4τ . In the following, we will often look at the LDOS $\mathcal{A}_j(\omega)$ in a 2d color plot like the one in fig. 5.3.

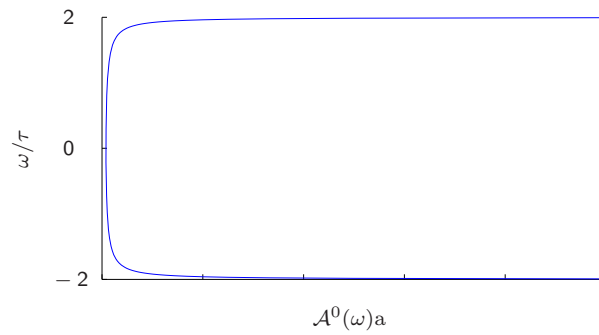


Figure 5.2.: LDOS of a tight binding chain. Near the lower and upper band edges at -2τ and 2τ we have a van Hove singularity $\sim \frac{1}{\sqrt{\omega}}$.

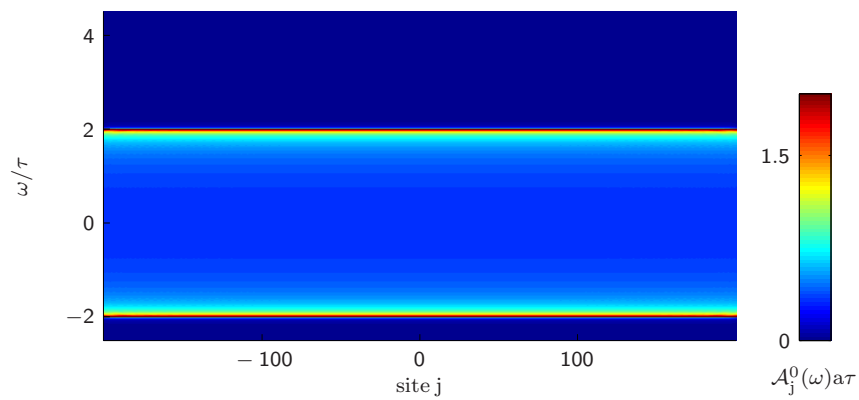


Figure 5.3.: LDOS of a tight binding chain in a color plot.

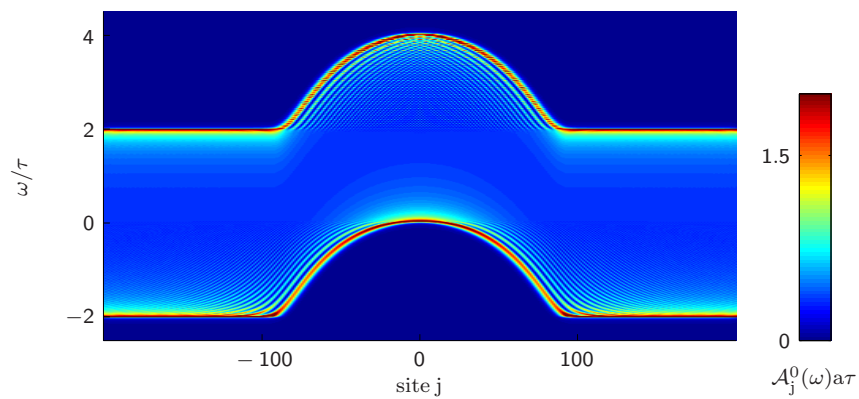


Figure 5.4.: LDOS of a chain with hopping $-\tau$ and a potential barrier with quadratic top. The band of the tight binding chain is deformed by the quadratic potential. The length of the central region was here $2N + 1 = 201$ sites.

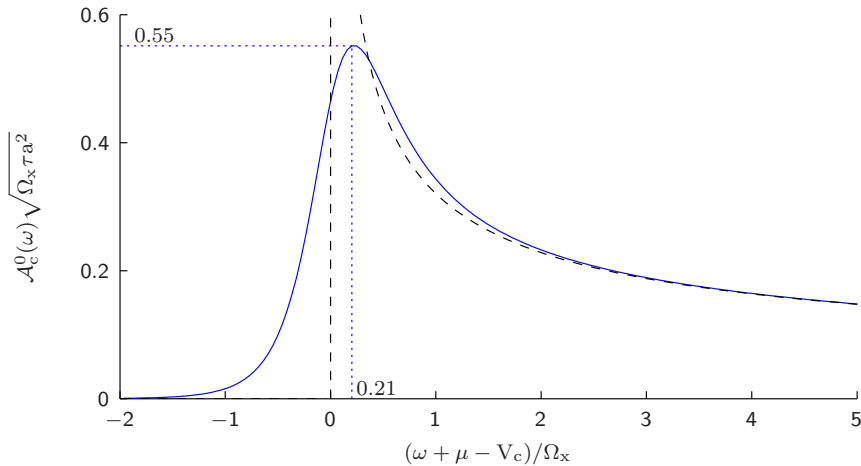


Figure 5.5.: Dependence of the LDOS at the center of the QPC on the frequency ω , at an gate voltage $V_c/\Omega_x = 0.025$. The upper and lower band edges are at -2τ and 2τ as above. The blue solid curve is the LDOS for the QPC, the black dashed curve is the LDOS for a tight binding chain with no potential. We see that the deviation of the peak in the LDOS with potential from the one without potential is given by $0.21\Omega_x$, and the width of the peak is also smeared out on a energy scale given by Ω_x . In this plot, the length of the central region is $2N + 1 = 101$ sites, implying a curvature $\Omega_x = 0.0566\tau$.

The next step in the development of our model is to switch on the parabolic potential. Again we evaluate $\mathcal{A}_j(\omega)$ and see that the band bottom (and the upper band edge, which is not relevant in our considerations) are lifted and mainly follow the form of the applied potential (see fig. 5.4)¹. Thereby, the van Hove singularity is smeared out on a scale $\sim \Omega_x$ and ceases to diverge, becoming a finite peak of magnitude $\frac{1}{\sqrt{\tau\Omega_x}}$ in the LDOS. This scale dependence will become clear from our plot below, see fig. 5.5. Keeping in mind the peaks origin, we will refer to this structure as the van Hove ridge. The apex of this ridge, which contains the most weight, lies just in the center of the QPC. The fringes at the flanks of the QPC near the lower and upper band edges are Friedel oscillations caused by the formation of standing waves due to reflection of electrons on the barrier.

In fig. 5.5, one sees that the smearing scale is indeed $\sim \Omega_x$, in the $j = 0$ case the peak of $\mathcal{A}_c^0(\omega)$ differs from the band bottom by the value $0.21\Omega_x$ and has the height of $0.55(\omega)a\sqrt{\tau\Omega_x}$. Furthermore, $\mathcal{A}_c^0(\omega) \rightarrow \mathcal{A}_{\text{tight binding}}(\omega)$ if ω becomes much larger than the band bottom ω_{min} . This corresponds to the case when electrons start to be able to move freely above the barrier².

The conductance behavior is dominated by the effect that we have already seen in the beginning. The QPC is closed if $\omega_{min} > \mu$ and opens up if $\omega_{min} \lesssim \mu$. In the non

¹For all actual calculations in this chapter, we have set $\mu = 0$

²To reduce the computational cost, we will use for the remainder of this work always $2N + 1 = 81$ as length of the central region if not explicitly stated otherwise. This implies a curvature $\Omega_x = 0.0707\tau$.

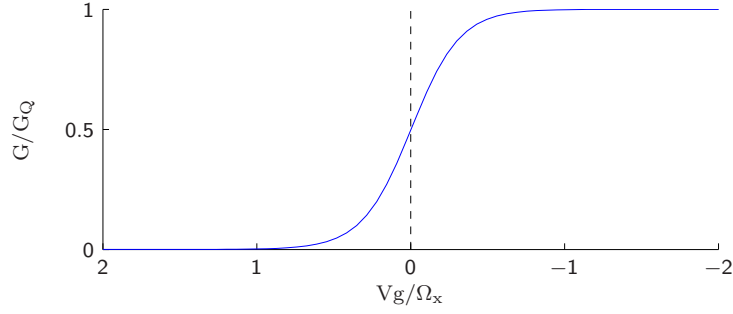


Figure 5.6.: The non-interacting conductance G/G_Q as a function of the gate voltage V_g/Ω_x . Note that the non-interacting conductance is antisymmetric with respect to the point $(0, 0.5)$. On this we will further elaborate below.

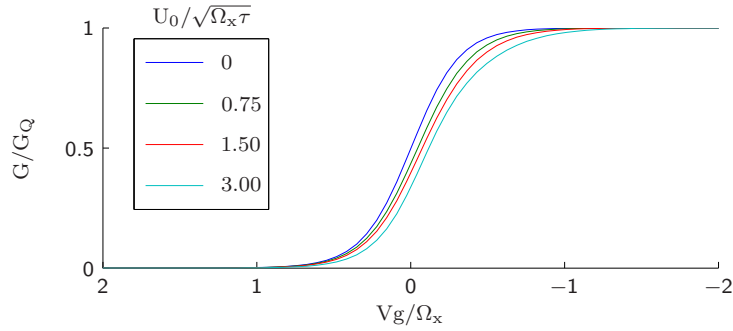


Figure 5.7.: Conductance G/G_Q for different on-site interaction strengths U_0 plotted against the gate voltage V_g/Ω_x . Note the slow development of the 0.7 shoulder.

interacting case ($U = 0$) the linear conductance looks then like shown in fig. 5.6.

Turning on the interaction U , things become more interesting (cf. fig. 5.7) and we see that with increasing U the conductance develops a shoulder at roughly $g = 0.7$, therefore known as the 0.7-anomaly. As explained by Bauer et al., this behavior arises essentially due to the shape of our van Hove ridge. In the sub-open regime, i.e. when we are in the area around $g \approx 0.7$, the apex of the van Hove ridge crosses the chemical potential. This has a major effect on our observables. For example, we have for the density

$$n_j = \int_{-\infty}^{\infty} d\omega \mathcal{A}_j(\omega) f(\omega) \stackrel{T=0}{=} \int_{-\infty}^{\mu} d\omega \mathcal{A}_j(\omega). \quad (5.12)$$

Now, since $\mathcal{A}_j(\omega)$ is not constant, $n_j(\mu)$ is obviously not linear in μ (we have $\partial_{\mu} n_i \propto \mathcal{A}_i(\mu)$). The most non linear behavior will occur when the apex of the LDOS, which is quite sharply localized and has a huge weight, crosses the chemical potential. In first order in the interaction, our self energy is just

$$\Sigma_{ii} = U_i \cdot n_i, \quad (5.13)$$

to which we will refer as the Hartree barrier. In the case $U = 0$, the on-site energy in the Hamiltonian grows linearly in the gate voltage V_g . If $U \neq 0$, this linear growth will be disturbed by the Hartree barrier since $n_i(V_g)$ is not linear, especially in the sub-open regime around $g \approx 0.7$. There, the density grows by a huge amount due to the passing of the LDOS apex through the chemical potential. Thus, the conductance will in this region be suppressed by the Hartree barrier. That is essentially the cause for the 0.7 shoulder and this effect increases the bigger the interaction strength U becomes. The effect can be further amplified by introducing an external magnetic field B . To explain this, let us first look again at the case where $U = 0$. If we switch on B , the on-site energy for electrons will be shifted by $-\frac{\sigma}{2}B$, causing the barrier for spin up electrons to decrease and for spin down electrons to increase. Thus, the spin resolved conductances will be merely shifted in V_g , see fig. 5.8.

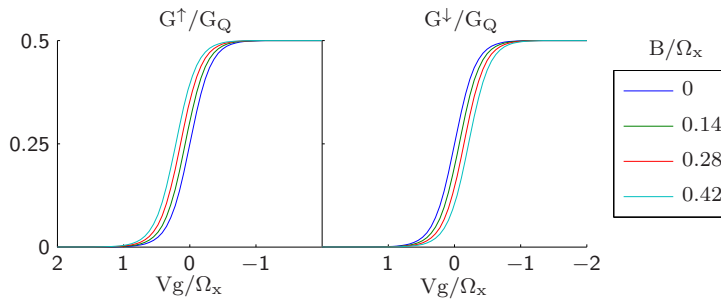


Figure 5.8.: The spin resolved, non-interacting conductances G^\uparrow/G_Q and G^\downarrow/G_Q for increasing magnetic fields, plotted against the gate voltage V_g .

Likewise, this shift will be visible in our other observables, the density and the susceptibility. But the whole conductance $g = g^\uparrow + g^\downarrow$ should stay symmetric to the point $V_g = \mu = 0$. (In fact, one can show for a pure quadratic barrier [24] that $g_\sigma^0 = \mathcal{T}_\sigma^0(0)$ with the bare transmission probability

$$\mathcal{T}_\sigma^0(\omega) \simeq \frac{1}{e^{-2\pi(\omega - \tilde{V}_c)/\Omega_x} + 1} \quad (5.14)$$

and thus $\mathcal{T}_\sigma^0(\tilde{V}_c, 0) = 1 - \mathcal{T}_\sigma^0(-\tilde{V}_c, 0)$.

If we now switch on U , we get a Hartree barrier which is much stronger for spin-down than spin-up electrons since it is determined in 1st order by the density of the opposite spin species:

$$\Sigma_{ii}^\sigma = n_i^{\bar{\sigma}} U_{ii}. \quad (5.15)$$

In this case, a lowering of V_g will induce the following behavior. At first, the spin-up electrons can pass the barrier and behave almost as if no interaction U is present because the density of the spin-down electrons is still low. If V_g is then small enough that also the spin-down electrons are energetically above the chemical potential, the density of the spin-up electrons in the QPC is already high. Therefore, the Hartree barrier for the spin-down electrons is much bigger than for the spin-up ones and thus their conductance is much more suppressed (cf. fig. 5.9).

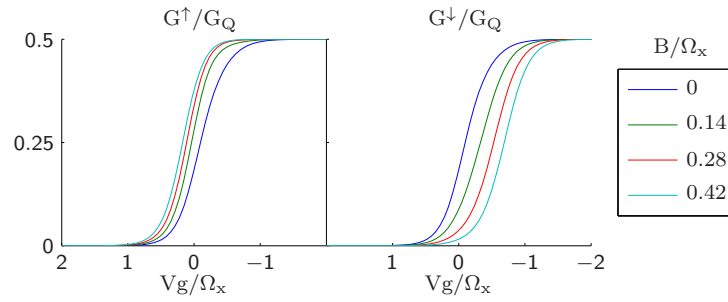


Figure 5.9.: The on-site interacting, spin resolved conductances G^\uparrow/G_Q and G^\downarrow/G_Q for increasing magnetic fields, plotted against the gate voltage V_g . The on-site interaction strength was here set to $U_0 = 0.6\tau$ which is in characteristic units $U_0\sqrt{\tau\Omega_x} = 2.26$.

This effect causes the whole conductance to develop from the 0.7 shoulder in a spin split plateau, see fig. 5.10.

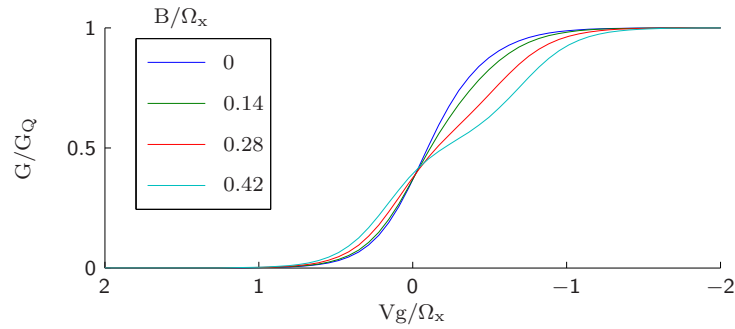


Figure 5.10.: The on-site interacting conductance G/G_Q plotted against gate voltage for different values of the magnetic field B .

To conclude our brief summary of the low energy QPC physics, we just take a short look at our other main observables. The density looks essentially like shown in fig. 5.11 for the transition of the closed to the open QPC.

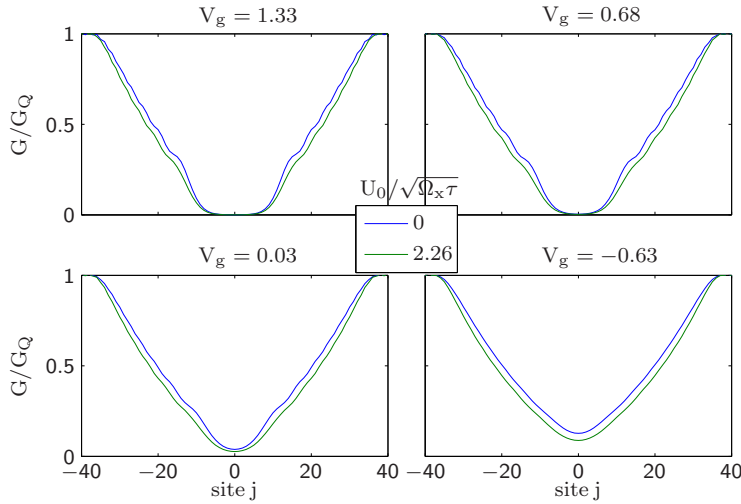


Figure 5.11.: The local density for decreasing values of V_g for the non-interacting case and for on-site interaction strength $U_0\sqrt{\tau\Omega_x} = 2.26$.

This is the behavior one would intuitively expect: The density is smallest where the barrier height is biggest and in the open case we have a higher density in the center as in the closed case, for which the center of the QPC is depleted.

Our third observable is the susceptibility. As mentioned before, we can compare the Kubo and the numerical susceptibility. However, for clarity we will just look at the numerical one first and comment on the use of the Kubo susceptibility in the next chapter. In general, the susceptibility (3.89) is given by

$$\chi_i = \frac{1}{2} \partial_B (n_i^\uparrow - n_i^\downarrow) \Big|_{B=0} \stackrel{T=0}{=} \frac{1}{2} \partial_B \int_{-\infty}^{\mu} (\mathcal{A}_i^\uparrow(\omega) - \mathcal{A}_i^\downarrow(\omega)) \Big|_{B=0}, \quad (5.16)$$

where $\mathcal{A}_i^\sigma = -\frac{1}{\pi} \text{Im} \mathcal{G}_{ii}^{R\sigma}(\omega + i0^+)$ (3.82). Since we have in the non-interacting case

$$\mathcal{G}_{ii}^\sigma(\omega) = \frac{1}{\omega - H} = \frac{1}{\omega - H_{\text{diag}} - H_{\text{non-diag}}} = \frac{1}{\omega - (V_j - \mu - \frac{\sigma}{2}B) - H_{\text{non-diag}}} \quad (5.17)$$

we get $\partial_B \mathcal{A}_i^\sigma = \frac{\sigma}{2} \partial_\mu \mathcal{A}_i^\sigma$ and thus end up with

$$\chi_i = \frac{1}{4} \int_{-\infty}^{\mu} d\omega \partial_\mu (\mathcal{A}_i^\uparrow + \mathcal{A}_i^\downarrow) = \frac{1}{2} \mathcal{A}_i(\mu), \quad (5.18)$$

where $\mathcal{A}_i(\mu) = \mathcal{A}_i^\uparrow = \mathcal{A}_i^\downarrow$ for $B = 0$. Thus, in the bare, i.e. $U = 0$ case, the magnetic susceptibility is largest when the apex of the van Hove ridge passes the chemical potential. If we now turn on interactions, $\partial_B (\mathcal{A}_i^\uparrow(\omega) - \mathcal{A}_i^\downarrow(\omega))$ is increased by the same mechanism as above, namely the different rise in the Hartree barriers which leads to an imbalance of the spins in favor for spin up. We can either consider the total susceptibility, i.e. summed over all sites (see fig. 5.12)

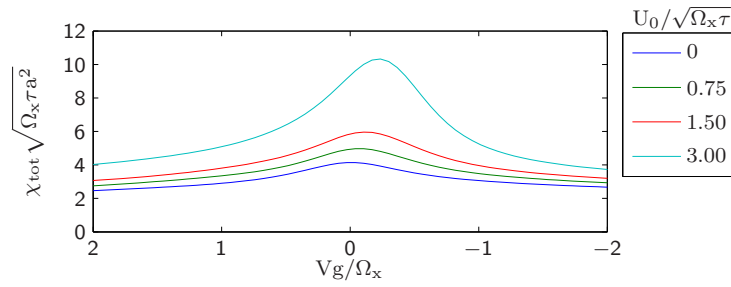


Figure 5.12.: The total susceptibility as a function of the gate voltage V_g for several on-site interaction strengths U_0 .

or we can also look at the site resolved susceptibility, which is plotted in fig. 5.13 for the gate voltage V_{gmax} at which χ_{tot} is maximal in the above plot at the moderate interaction strength $U_0 \sqrt{\Omega_x \tau} = 1.5$.

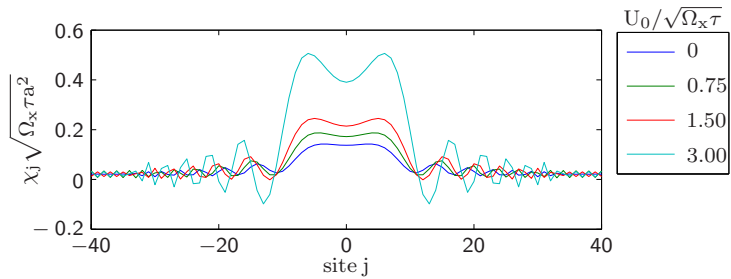


Figure 5.13.: The local susceptibility for the gate voltage $V_g = -0.1697 / \Omega_x$ with increasing interaction strength

With this considerations, we have the $T = 0$ temperature physics of a QPC with short ranged interactions pretty much at hand.

In the next chapter, we will compare the numerical results of an on-site model computed first with the old algorithm with feedback length $L = 0$ and then with our new algorithm for feedback lengths $L > 0$.

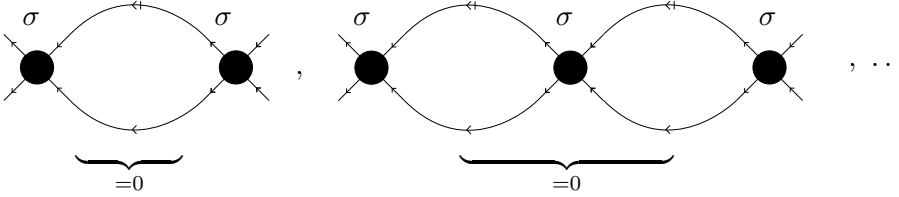
6. Numerical results

6.1. Test of the new method on the on-site model

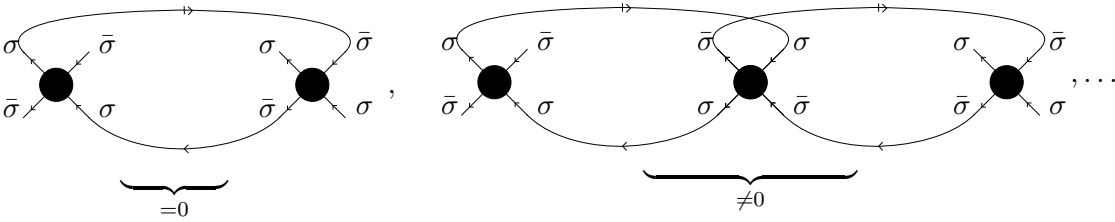
In this section, we will take a look on the results we get with our derived method. The first model we will try to solve with the new method is the previously described QPC, where we assume the interaction in (4.1) to be point like

$$U_{ij} \sim U_i \delta_{ij}. \quad (6.1)$$

This case has been studied extensively by Bauer et al. and provides us with a starting ground to check if our algorithm produces in this case the known results. In a perturbative picture, we should basically get the same up to second order in the interaction and then differ in higher order terms. However, there is a subtlety. If one derives the flow equations having in mind from the start that the interaction will be point like, there is no need to include the flow of the quantities $P_{ji}^{\sigma\sigma 00}$ and $\bar{X}_{ji}^{\sigma\bar{\sigma} 00}$ since these quantities are zero in second order. $P_{ji}^{\sigma\sigma 00}$ will in fact remain zero in every order thus it also vanishes in our method, as can be seen in the figure below:



The quantity $\bar{X}_{ji}^{\sigma\bar{\sigma} 00}$, however, is different. If we use our method with an arbitrary interaction, this quantity is in general generated in second order in the interaction. In the on-site case, one sees that the second order vanishes



but higher orders still exist. Our algorithm takes these higher orders always into account, even if we are in the on-site case. Therefore, our results should deviate slightly from the previous ones by Bauer et al. In a recent paper by Goulko et al. [25], this contributions were taken into account in the framework of studying QPCs with spin-orbit coupling. Here, one has a similar situation: $\bar{X}_{ij}^{\sigma\bar{\sigma} 00}$ is generated in 2^{nd} order for finite spin orbit interaction (SOI) and therefore is taken into account in Goulko's work, also

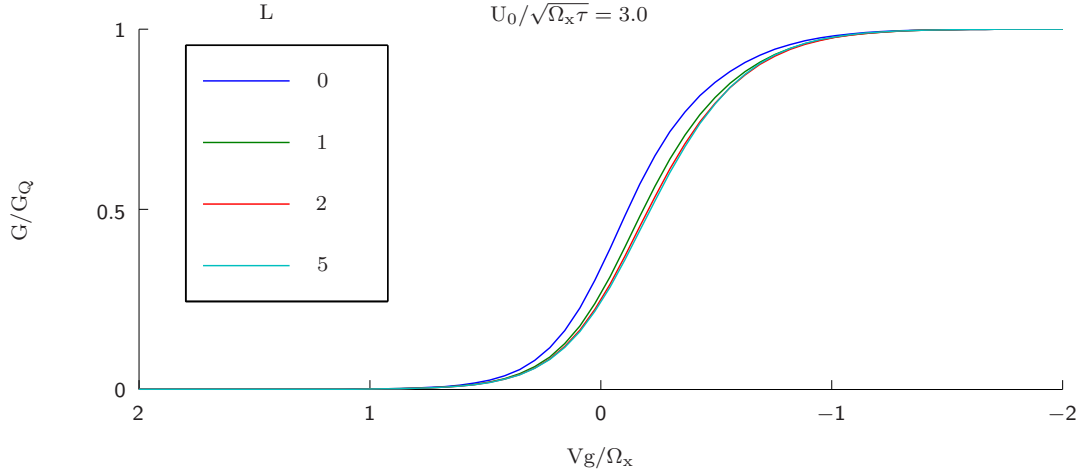


Figure 6.1.: The conductance for on-site interaction strength $U_0 = 2.26/\sqrt{\Omega_x\tau}$ plotted against gate voltage for increasing values of the feedback length L .

in the limit of the SOI going to zero. Thus, our special case of "pure on-site interaction" should correspond to Goulko's special case of "non spin-orbit coupling". Indeed, we compared here results for the self-energies with different parameters of our model and obtained that we have a good numerical agreement with an maximal relative error of approximately 10^{-6} . Next, we study how our observables depend on the feedback length L using various parameters for the magnetic field and the interaction strength U , while the chemical potential is set to zero, implying half filled leads. To begin with, let us look again on same plots for the conductance, see fig. 6.1.

We first notice that independently of the shape of the conductance curves our method for longer ranged feedback seems to converge in the limit of large L , which certainly is reassuring. In the chosen parameter regime, there is actually no point to increase $L \gtrsim 5$. Comparing the conductance curves for different L , we first clearly observe a shift in the gate voltage V_s which marks the onset point of the conductance. The higher the value of L the larger is the shift of the pinch-off voltage V_s to lower conductance values. This shift arises due to the different types of diagrams which are involved when we increase L . Therefore, the comparison of those curves is not as straight forward as the one, e.g., for different values of the interaction strength U at the same value of L . Nevertheless, we will later trace back this shift in V_g to the off-central blocks in our vertex quantities which arise when L becomes bigger than zero. At this point, however, we remark that in actual experimental implementations the onset point in the conductance can be observed but it depends on many details and therefore is often not the quantity of primary interest. Instead, it is the shape of the conductance curves that is usually measured to great accuracy. Thus, at this point we shift our conductance curves to have the same onset point V_s in order to compare there shapes modulo the shift in V_g . For clarity, we plot in fig. 6.2 only the curves for $L = 0$ and $L = 5$ for which the shape of the conductance

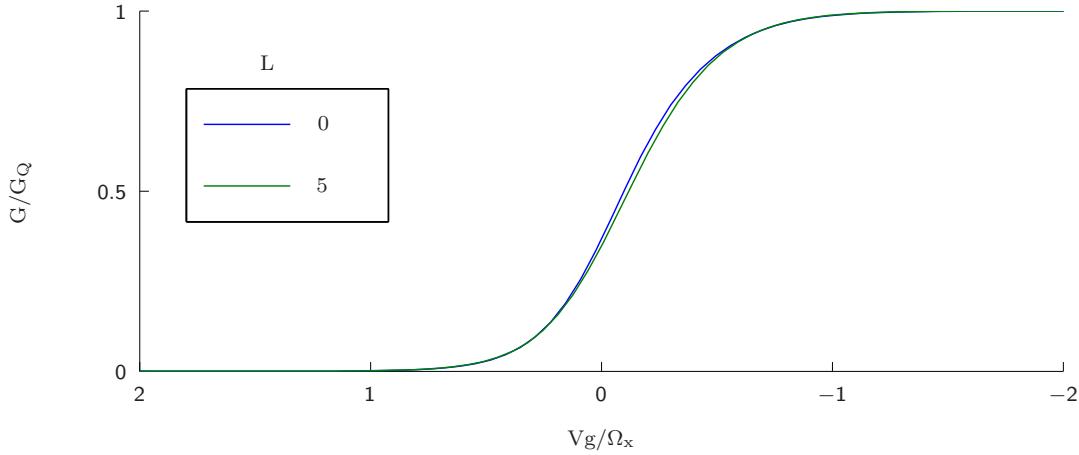


Figure 6.2.: The on-site interaction conductance curves for $L = 0$ and $L = 5$ plotted as above but with the latter curve shifted to a more positive V_g value, such that the pinch-off of the two curves becomes equal.

differs most.

We notice further that this development from small to larger L looks in fact somewhat similar to the dependence of the conductance on U (cf. fig. 5.7). With increasing L the curve becomes less steep in the onset and the 0.7 shoulder seems to be weakened. Thus, we get a first hint that the method with longer ranged feedback L and some interaction U_L may be compared to the method with $L = 0$ and some interaction $U_0 > U_L$. Let's look if this tendency can be supported by the comparison of different susceptibility values. We get here for different L in a moderate parameter regime the total susceptibility shown in fig. 6.3 or the site resolved susceptibility at the gate voltage $V_g/\Omega_x = -0.23$ (that is the position of the maximum of the $L = 0$ curve in fig. 6.3) which is depicted in fig. 6.4.

Keeping in mind the shift in V_g , the behavior with increasing L is again similar to that in fig. 5.12 and fig. 5.13 which is obtained by decreasing the interaction strength U . We emphasize that this results were obtained in a parameter regime where both methods are convergent. If we now raise the interaction strength U , we observe the following behavior. In the on-site case, using the algorithm without l.r. (longer ranged) feedback the point up to which fRG is convergent is around $U = 4\sqrt{\Omega_x\tau}$. However, with our new method using longer ranged feedback we can increase the on-site interaction strength much farther, see fig. 6.5 and fig. 6.6. At this point, a technical comment may be in order. In the derivation of the fRG equations, we assumed U to be small compared to the energy τ . Nevertheless, in fig. 6.5 and fig. 6.6 we have increased the interaction strength to values $U > \tau$ and obtain still convergent (and apparently physical meaningful) results. This astonishing feature of fRG has been noted before, cf. [13] and is known to give for various applications the right results. Therefore, we will at this point not worry too

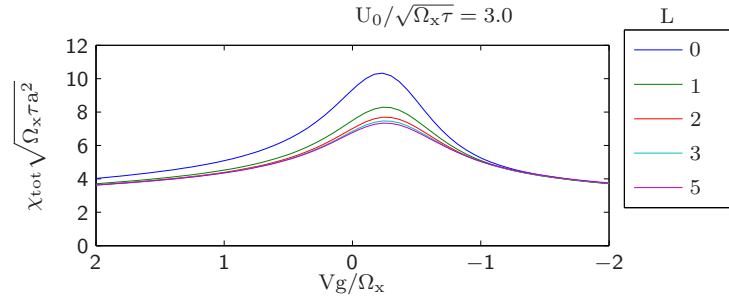


Figure 6.3.: The total susceptibility plotted as a function of gate voltage for increasing feedback length L . We first notice that the susceptibility becomes weaker for increasing L . Furthermore, we have again the same shift of the maximum of χ_{tot} to more negative values of V_g with increasing L which was already observed in the conductance.

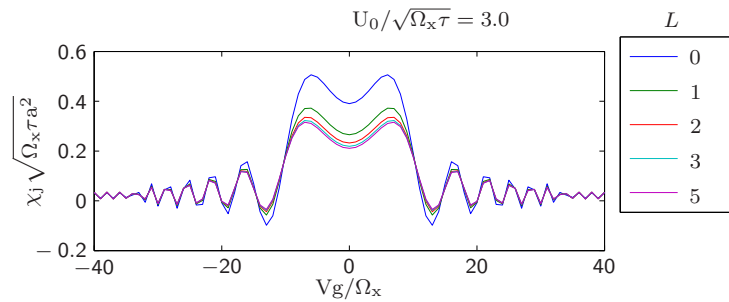


Figure 6.4.: The local susceptibility, again plotted for increasing values of L

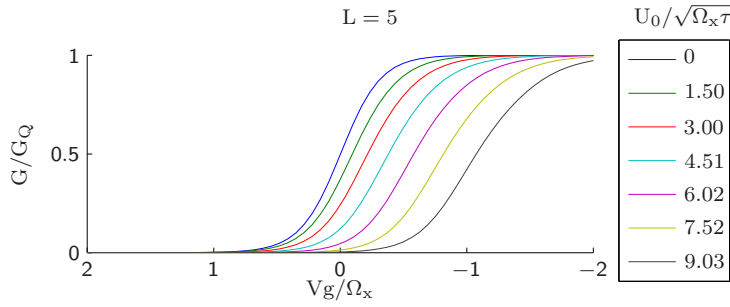


Figure 6.5.: The conductance as a function of gate voltage plotted for increasing on-site interaction strength U_0 for a feedback length $L = 5$. Note that we can by far exceed the point $U_0/\sqrt{\Omega_x\tau} \approx 3.5$ at which the method without longer ranged feedback begins to diverge.

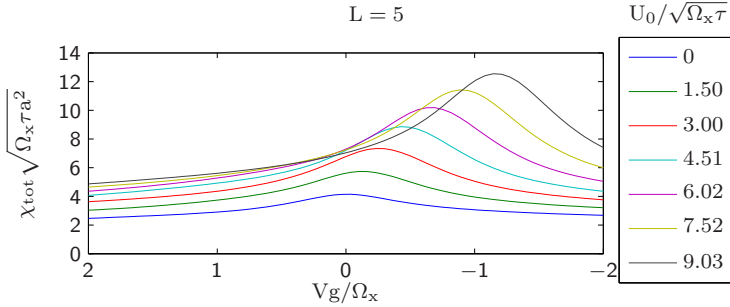


Figure 6.6.: The total susceptibility as a function of gate voltage plotted for the same parameters as the conductance above.

much about this, and continue to use bare interaction strengths $U \gtrsim \tau$ ¹.

As conclusion we state here that the longer ranged feedback seems to admit a much higher interaction strength U before our fRG flow begins to diverge. This alone would not be remarkable since we have seen that for physical comparison of the two methods we would have needed in any case a higher U . The astonishing fact is that with the l.r. technique we can in fact go beyond the correspondence point where the old technique already diverges. Thus, we can really reach a new physical parameter regime. A first indication for this can be seen by comparing fig. 6.6 with fig. 5.12. The height of the susceptibility χ , which is a real measurable physical quantity, can in the longer ranged feedback case increased beyond the height which was previously possible within the well behaved regime of our old algorithm. Here, this argumentation may seem a bit far fetched, but we will see stronger evidence for this at a later point, namely when

¹Of course, we could also hold the bare interaction strength $U < \tau$ and obtain nevertheless a high effective interaction strength by reducing the curvature Ω_x . However, we would then have to use a longer central region, i.e. increase N and would have to increase the computation time significantly since it scales like $(2N + 1)^3$.

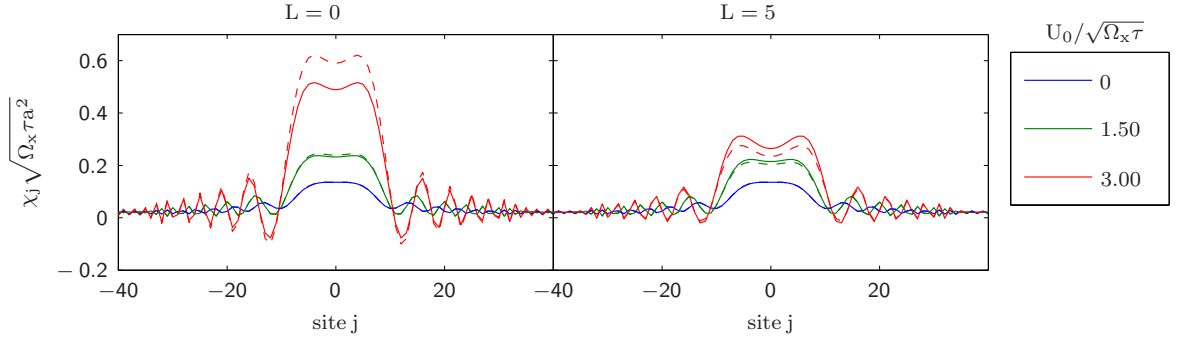


Figure 6.7.: The two different site resolved susceptibilities (numerical: solid lines, kubo: dashed lines) are plotted for $L = 0$ and $L = 5$ for several values of the on-site interaction strength U_0 . Note that both susceptibilities are reduced when the longer ranged feedback is used. For large interaction strengths the relative error between the numerical- and Kubo susceptibility in the $L = 5$ case is slightly reduced.

studying the transition from a QPC to a quantum dot (QD).

At this point, we also comment on the Kubo susceptibility we have defined earlier. Of course, one can also study the behavior of this susceptibility with increasing feedback length L . We didn't dwell too deep into this but took only a short look, see fig. 6.7. Reassuringly, the relative error at larger interaction strengths between the two susceptibilities (which stems from our approximative treatments) seems to be slightly reduced for the longer ranged feedback case. Concretely, if we compare the susceptibility values for $U_0/\sqrt{\Omega_x\tau} = 3.00$ at the center $j = 0$, we get in the $L = 0$ case a relative error of $(\chi_{kubo} - \chi_{num})/\chi_{num} = 0.21$ whereas it is in the $L = 5$ case only -0.11 .

Now let us look into the reasons for the behavior we have observed so far and try to determine its mechanisms. Our starting point will be the resulting self energies, calculated at $L = 0$ and $L = 5$. By looking at fig. 6.8, we see that the self energies are dominated by the diagonal parts and have relatively weak off-diagonal structures. Thus, let us first compare the two diagonals of our different methods, see fig. 6.9. In the self energy for the bigger L , the barrier in the middle of the constriction is slightly lower, causing a shift in V_g . Nevertheless, this resulting shift is actually over a magnitude weaker than the one observed in the conductance (cf. fig. 6.1) and additionally goes in the wrong direction. Thus, in order to determine the difference between our methods we have to study the weak off-diagonal parts of the self-energies. In the following diagram in fig. 6.10 we have plotted the first and the second off-diagonals. The striking observation is here that the self-energies deviate by a substantial amount in the center region of the off-diagonal terms. We observe here for $L > 0$ a visible upward shift, which is, for example, in the first off-diagonal of a value around $2.5 \cdot 10^{-3}\tau$.

Before we try to use this observation in order to explain the V_g shift in the conductance, we first comment on how the conductance curves evolve by taking different numbers of

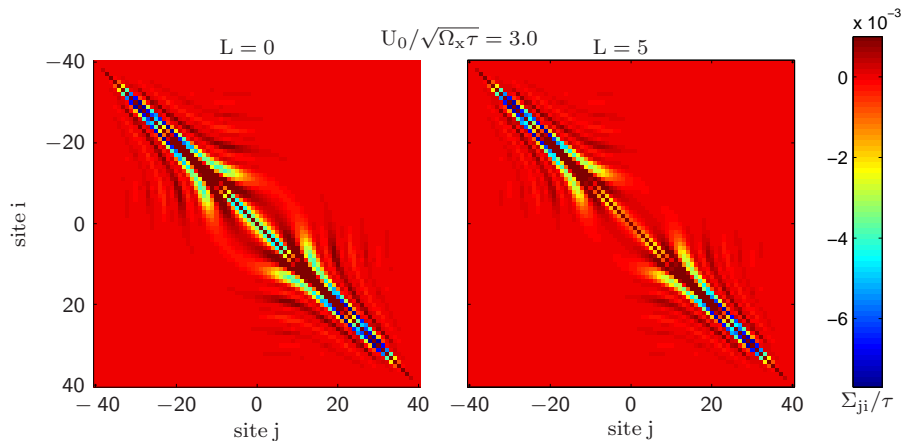


Figure 6.8.: The self-energies for the on-site interacting case with feedback lengths $L = 0$ and $L = 5$ at $V_g/\Omega_x = -0.36$ (which lies in the 0.7-shoulder of the $L = 0$ case). In order to render the off-diagonal structures visible, we have used a colorscale between $-8 \cdot 10^{-3}$ and $1 \cdot 10^{-3}$ for Σ_{ji}/τ . Note that the main difference of the two selfenergies lies in the central region of the first few off-diagonals.

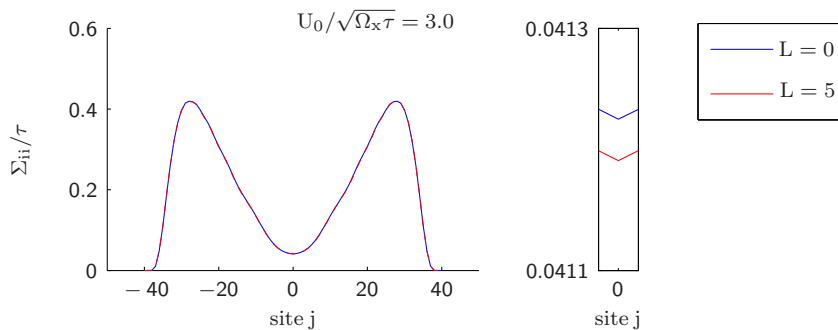


Figure 6.9.: Left: the diagonal of the self-energy is plotted for $L = 0$ and $L = 5$ at $V_g/\Omega_x = -0.36$. Notice that the relative deviation of the two diagonals is practically zero. Right: The absolute deviation of the two self-energies at site 0. Note that this difference is of magnitude 10^{-4} which is much too small to give the observed $V_g/\tau \approx 5 \cdot 10^{-3}$ (this quantity can be extracted from figure 6.1) shift in the conductance.

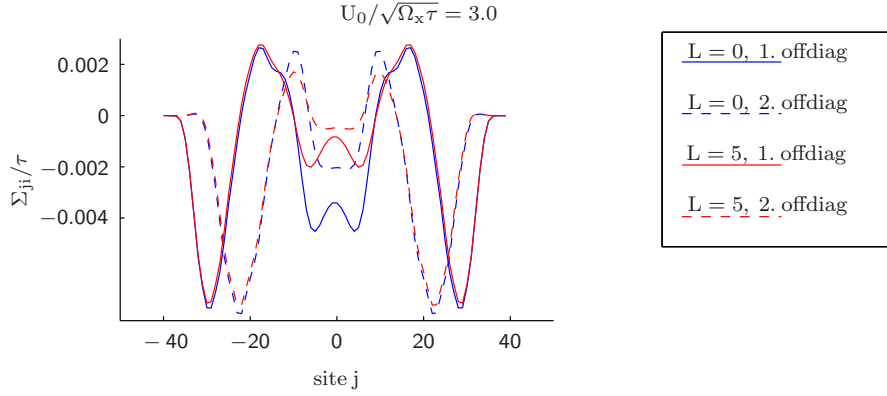


Figure 6.10.: The first and second off-diagonals of the self-energies for feedback ranges $L = 0$ and $L = 5$. The applied gate voltage was again $V_g/\Omega_x = -0.36$. Note that the main difference occurs in the central region, approximately given by the site interval $[-7a, 7a]$ which is on the scale of the characteristic length $l_x \approx 3.76a$ of our quadratic potential.

off-diagonals in the self-energy into account. We found that in principal one has to take a large number of off-diagonals to get the conductance quantitatively right.

However, to observe the main effect, namely the shift of the conductance to smaller V_g values and a smaller effective interaction strength it suffices to take only the first off-diagonal into account, see fig. 6.11. By including the upwards shift in the first off-diagonal, we can explain shift in the gate voltage V_g . To realize this, let us assume we start from the $L = 5$ case. Since the self-energy is in our approximation frequency independent, we can define an effective Hamiltonian $H_{eff} = H + \Sigma$. Thus, the first off-diagonal of the self-energy will merely change the hopping $-\tau$ to an effective hopping $-\tau_{eff} := -\tau + \Sigma_{jj+1}$. The upward shift in the first off-diagonal -compared to the $L = 0$ case- of the self-energy by $2.5 \cdot 10^{-3} > 0$ leads to a reduced hopping amplitude in the center of the QPC: $\Delta\tau_{eff} = \Delta\Sigma_{jj+1}$ with j taken to be in the central region. This reduced hopping leads to a narrowing of the band in the center, see fig. 6.12. Since the band edges are given by -2τ and 2τ , the effective barrier in the center of the QPC is shifted upwards by an amount $\sim 2\Delta\tau_{eff} \approx 5 \cdot 10^{-3}$. In our above case, this fits perfectly with the observed shift in the conductance which is also around $5 \cdot 10^{-3}$. On the other hand, this central upward shift also leads to a slightly larger curvature at the center of the QPC, see fig. 6.13. Since the width of the conductance step is determined by Ω_x , this leads to a less steep conductance step $L = 5$ compared to the $L = 0$ case. However, the lesser effective interaction strength at $L = 5$ seems to arise mainly from the better coupling between the channels. Concretely, if we look at the maxima of the different channels, plotted in fig. 6.16 we see that in the convergent regime of the $L = 0$ case the positive contribution from the $X^{\uparrow\downarrow}$ channel is compensated by the negative contribution of the $P^{\uparrow\downarrow}$ channel. When we then rise the bare interaction strength $U_0/\sqrt{\Omega_x\tau}$ from 3.0

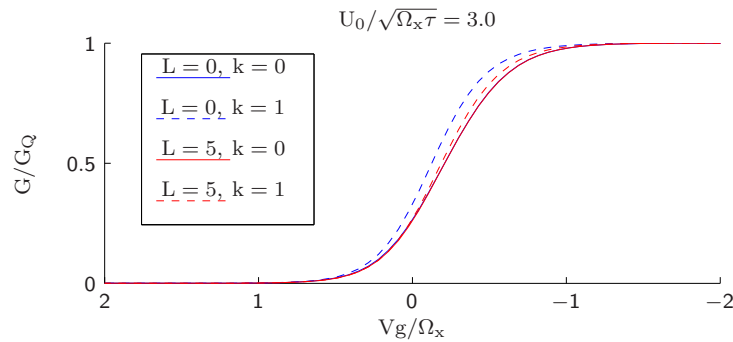


Figure 6.11.: The conductances which result from taking only the main-diagonal (solid lines) and from taking the main- and the first off-diagonal (dashed lines) of the self-energy into account. Note that the shift to positive V_g -values is in the $L = 0$ case much stronger than for $L = 5$.

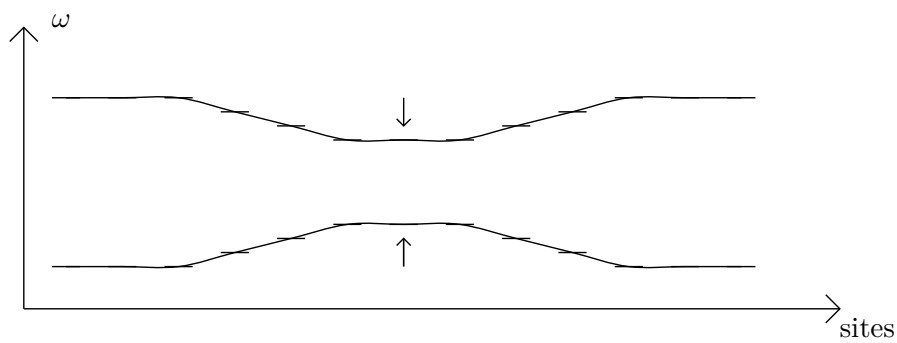


Figure 6.12.: The effectively reduced hopping in the center for the $L = 5$ case leads to a reduced bandwidth compared to the $L = 0$ case. The physical relevant behavior is the resulting upwards shift of the band bottom causing a changed height and shape of the potential.

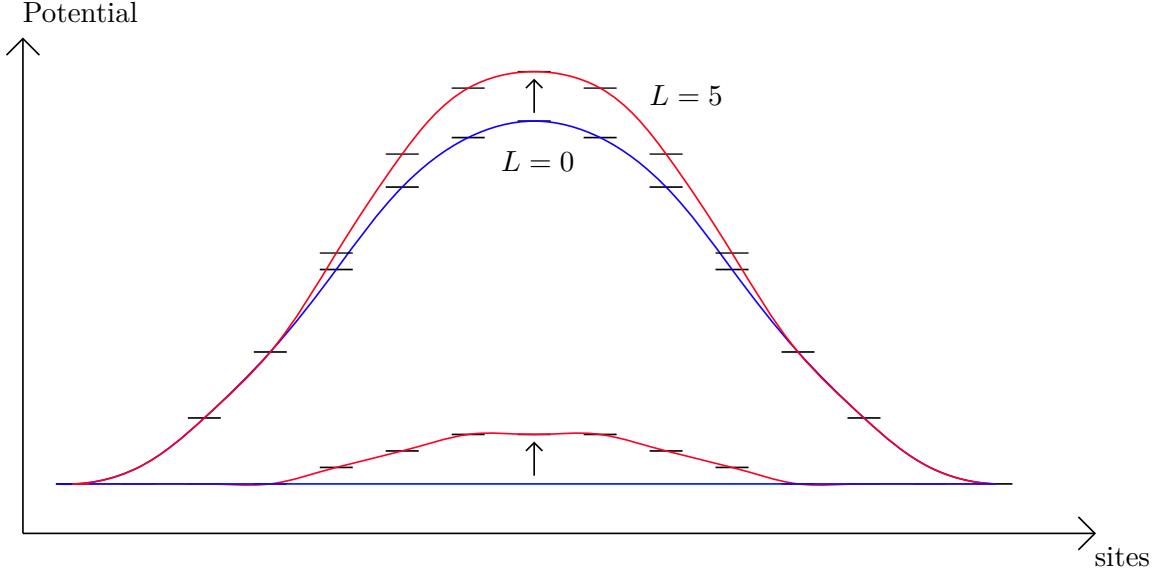


Figure 6.13.: Sketch of the change in the potential shape due to the effectively reduced hopping in the $L = 5$ case. As usual, the blue line denotes the $L = 0$ potential, and the red line the $L = 5$ potential. Note that aside from the upwards shift, the curvature for the $L = 5$ case becomes slightly smaller than for the $L = 0$ case.

to 4.51, the $X^{\uparrow\downarrow}$ contribution starts to diverge to $+\infty$ while $P^{\uparrow\downarrow}$ roughly stays the same. In the $L = 5$ case, however, we see that due to the improved feedback the increase of $X^{\uparrow\downarrow}$ is compensated by $P^{\uparrow\downarrow}$ and the flow still converges without problems. Thus, the effective interaction strength gets weaker, when the same bare interaction strength U enters in both methods. This lesser effective interaction strength then leads to a much larger bare interaction U which is needed to reproduce the 0.7 shoulder in the $L > 0$ case.

Let's now see if we can relate this shift in the first off-diagonal of the self-energy closer to the off-center terms in the constituents of our two-particle vertex γ_2 . For this purpose, we use a relation which connects the self-energy Σ with the two-particle vertex (cf. [26]):

$$\begin{aligned} \Sigma(q_1, q_8) = & \sum_{q_2, q_3} \nu(q_2, q_1; q_3, q_8) \mathcal{G}_{q_3, q_2} \\ & - \frac{1}{2} \sum_{q_2, q_3, q_4, q_5, q_6, q_7} \nu(q_2, q_1; q_3, q_4) \mathcal{G}_{q_4, q_6} \mathcal{G}_{q_3, q_5} \gamma_2(q_5, q_6; q_7, q_8) \mathcal{G}_{q_7, q_2}. \end{aligned} \quad (6.2)$$

In a diagrammatic language this could be expressed as in fig. 6.14:

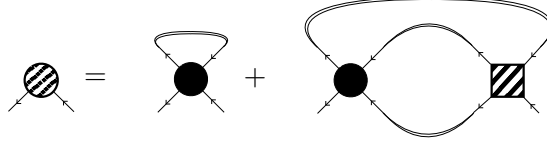


Figure 6.14.: Diagrammatic relation between the selfenergy and the two particle vertex. The double lines denote here the full Green's functions \mathcal{G} , round black dots the bare vertices, and the dashed dot and the dashed square the self-energy and the two-particle vertex, respectively.

Using this relation we could now study what effects we get if we only insert certain parts of the two-particle vertex at the right hand site, namely the term arising from the central blocks or the off-site blocks, respectively. However, since the numerical evaluation of the second diagram term on the r.h.s. tends to be tedious due to the convolution in frequency space, we notice that there is in fact a nice way to compute the corresponding quantities in our fRG-scheme. For this purpose, we simply introduce in our flow two additional self-energy quantities, to be called Σ_c^Λ and Σ_{off}^Λ and define them by splitting the flow (4.9) for the self-energy in two terms

$$\frac{d}{d\Lambda} \Sigma^\Lambda = \frac{d}{d\Lambda} \Sigma_c^\Lambda + \frac{d}{d\Lambda} \Sigma_{off}^\Lambda \quad (6.3)$$

where

$$\frac{d}{d\Lambda} \Sigma_{c/off}^\Lambda(q'_1, q_1) = -T \sum_{q'_2, q_2} \mathcal{S}_{q'_2, q'_2}^\Lambda \gamma_{2c/off}^\Lambda(q'_2, q'_1; q_2, q_1). \quad (6.4)$$

Here, $\gamma_{2c/off}^\Lambda(q'_2, q'_1; q_2, q_1)$ refers to the central or off-site constituents of the two-particle vertex, which arise naturally from the equations (4.7)

$$\begin{aligned} \gamma_2(j'_1 \sigma, j'_2 \sigma; j_1 \sigma, j_2 \sigma) = & \nu(j'_1 \sigma, j'_2 \sigma; j_1 \sigma, j_2 \sigma) + P_{j'_1 j_1}^{\sigma\sigma(j'_2 - j'_1)(j_2 - j_1)} \\ & - D_{j'_1 j_1}^{\sigma\sigma(j_2 - j'_1)(j'_2 - j_1)} + D_{j'_1 j_2}^{\sigma\sigma(j_1 - j'_1)(j'_2 - j_2)} \end{aligned} \quad (6.5)$$

and

$$\begin{aligned} \gamma_2(j'_1 \sigma, j'_2 \bar{\sigma}; j_1 \sigma, j_2 \bar{\sigma}) = & \nu(j'_1 \sigma, j'_2 \bar{\sigma}; j_1 \sigma, j_2 \bar{\sigma}) + P_{j'_1 j_1}^{\sigma\bar{\sigma}(j'_2 - j'_1)(j_2 - j_1)} \\ & + X_{j'_1 j_1}^{\sigma\bar{\sigma}(j_2 - j'_1)(j'_2 - j_1)} - \bar{X}_{j'_1 j_2}^{\sigma\bar{\sigma}(j_1 - j'_1)(j'_2 - j_2)}, \end{aligned} \quad (6.6)$$

when we set on the r.h.s. all off-site or all central terms to zero. In this manner we actually produce something similar to the diagrammatic equation fig. 6.14 and split the self energy in two parts, one corresponding to the central terms in γ_2 and one corresponding to the off-site blocks. Of course, this splitting in the two contributions is far from complete. Since we use the whole single scale propagators (or the whole Green's functions in diagram fig. 6.14) in our flow, we actually have nevertheless a mixing of the two contributions. However, as a first estimate this should give us at least the right tendency in the first order of the interaction. If we compare the predictions for the first

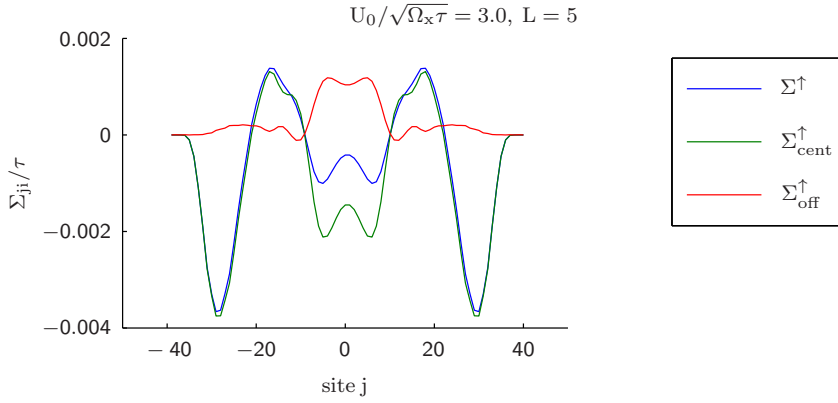


Figure 6.15.: The different vertex contributions to the first off-diagonal of the self-energy, again evaluated at a gate voltage $V_g/\Omega_x = -0.36$. Note that the main effect of the off-site contribution is indeed to cause an upwards shift in the central region, thus effectively reducing the hopping.

off-diagonal in the self-energy, see fig. 6.15, we indeed observe that the off-site terms cause a upward shift. Of course, this shift is somewhat mediated in comparison to the one observed in fig. 6.10 by about an factor of 2 due to the reasons mentioned above, but we can qualitatively see the right behavior.

Concluding this section, let us briefly comment on the better convergence of our longer ranged feedback algorithm compared to the $L = 0$ case. For this we take first a look at the maximum values of the different channels during a sweep of the gate voltage V_g over the conductance step, cf. fig. 6.16.

We see that the quantities with the largest contributions are the $X^{\sigma\bar{\sigma}}$ and $\bar{X}^{\sigma\bar{\sigma}}$ channels. In fig. 6.17 and fig. 6.18 we have explicitly plotted the $X^{\sigma\bar{\sigma}}$ channel for our default gate voltage $V_g/\Omega_x = -0.36$.

We observe that the peaks in the center block get damped when we increase L from zero to larger feedback lengths which effectively causes the better numerical convergence of the flow equations. Again, this alone is not remarkable, since we have to compare different bare interaction strengths U for our methods to obtain the same physical results. However, for our algorithm with longer ranged feedback the interplay between off-site and central blocks seems to stabilize each other far over the point where the simpler $L = 0$ algorithm tends to diverge. In intuitive terms, it seems as if the effective additional degrees of freedom which are represented by the off-site blocks can take some weight of the interaction which would otherwise be concentrated simply in the central block. For a more thorough analysis, one could study the interplay between the central- and off-site terms using the flow equations (4.7) much in the same way as in (6.4) where we studied the influence of the offsite blocks on the self-energy. However, at the moment we will simply accept the better convergence of the longer ranged feedback as a fact and see if we can use this to explore new parameter regimes in the onsite-model. Explicitly, our

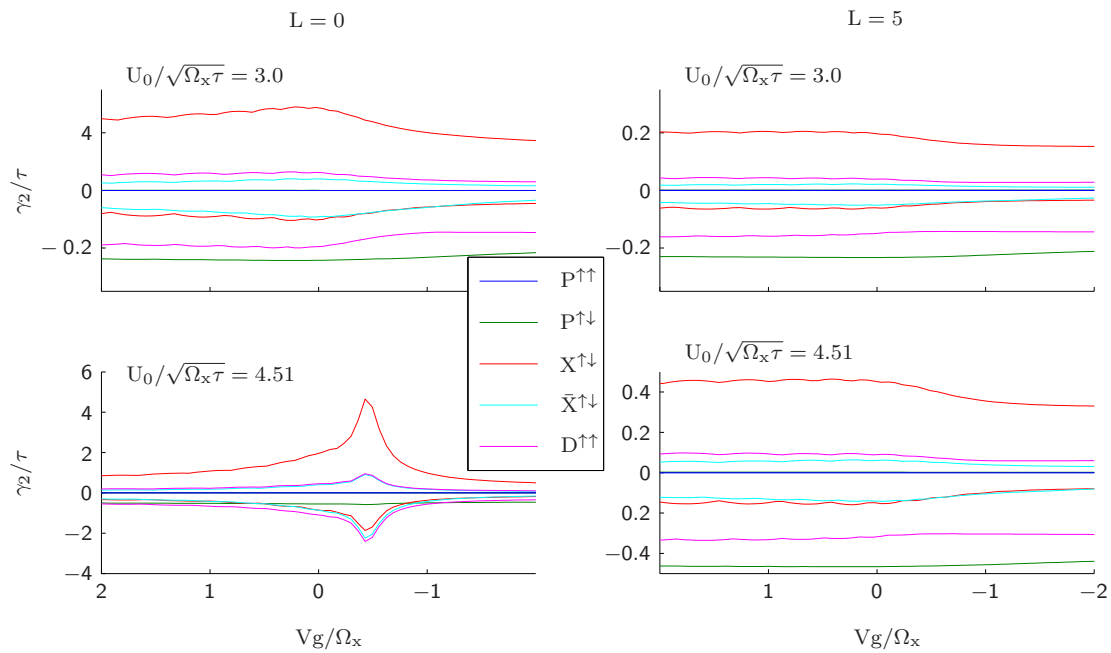


Figure 6.16.: The magnitude of the different channels plotted against gate voltage for the interaction strengths $U_0/\sqrt{\Omega_x\tau} = 3.0$ and $U_0/\sqrt{\Omega_x\tau} = 4.5$ for both feedback lengths $L = 0$ and $L = 5$. Note that for the minor interaction strength the results for different feedback do not differ much. However, in the second row of plots U_0 is raised into the regime where the $L = 0$ method is close to divergence, which results in large peaks in it's channels. On the contrary, the channels of the $L = 5$ method are still well behaved and, in fact, converge without problems.

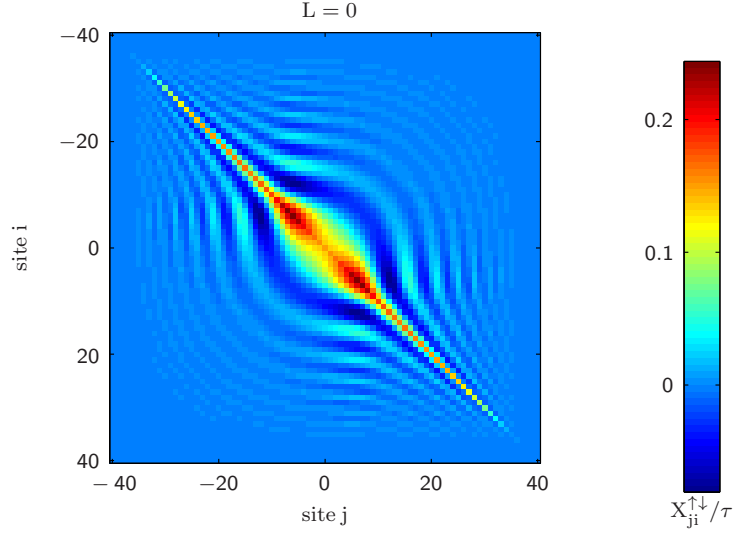


Figure 6.17.: Graphical depiction of the $X_{ji}^{\sigma\bar{\sigma}00}$ channel plotted for $L = 0$, i.e. it consists only of the central block.

point of interest will be to study systems with a relative small curvature and a large maximum of the LDOS close to the chemical potential. Prominent examples for this are QPCs with non parabolic potential, i.e. quartic, sextic, etc. potentials as well as the transition between a QPC and a quantum dot (QD), where the crossover occurs in the sub-open regime of the nano structure. We will further pursue this in the last two sections. At this point, we will at last introduce the actual longer ranged interactions which where the driving cause to establish the whole new formalism in the first place.

6.2. Introduction of longer ranged interactions

Here, finally we comment on the role of off-site interactions in our system. In order to do this, we first explain the formation of the bare interaction in the QPC. Naively, one would assume to take a one dimensional coulomb interaction, since we have an effectively one dimensional system. However, this would be not correct, since in order to get to this model we have to integrate out the other two spacial dimensions and therefore have to modify the interaction accordingly. To get a somewhat more realistic estimate on the structure of longer ranged interactions, we follow an approach by Lunde et al. [27] and try to integrate out the y - and the z -direction explicitly. For the latter, we assume here first a simple δ -function, corresponding to a perfect two dimensional electron gas. In the y -direction we assume quadratic potential barriers much in the same way as in the x -direction, but with a much greater curvature $\Omega_y \gg \Omega_x$, see fig. 1.3. We begin with the Hamiltonian in the continuous form $H = H_0 + H_1$, with

$$H_0 = \sum_{\sigma} \int d^3x (U(x) + T) \psi_{\sigma}^{\dagger}(x) \psi_{\sigma}(x) \quad (6.7)$$

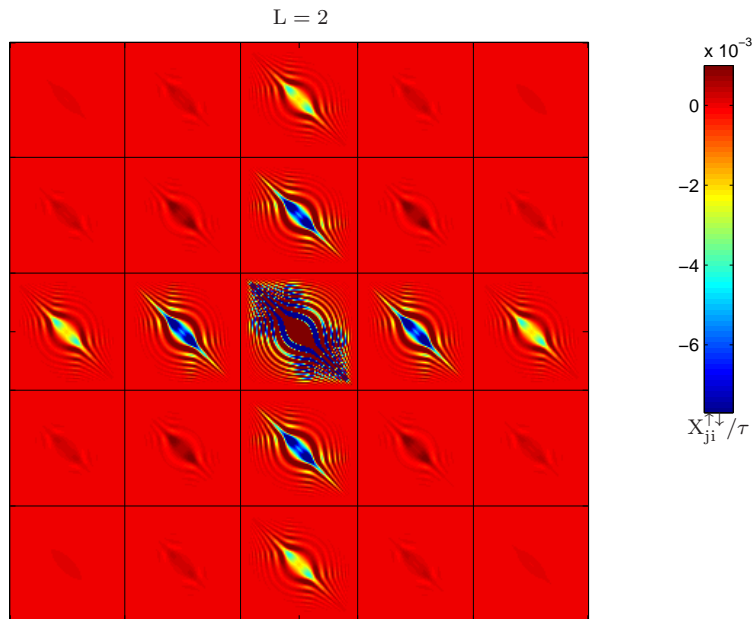


Figure 6.18.: The $X_{ji}^{\sigma\bar{\sigma}lk}$ channel for the $L = 2$ case. In order to render the small non central blocks more visible, we used a color scale in the range $[-8 \cdot 10^{-3}\tau, 1 \cdot 10^{-3}\tau]$. We have plotted the channel in it's block matrix representation which we derived above. The central block is clearly dominant, the off-blocks become weaker with increasing block indices l, k . Note that the largest off-blocks are the ones where either $l = 0$ or $k = 0$, i.e. the ones where during the effective interaction only one of the two particles is scattered.

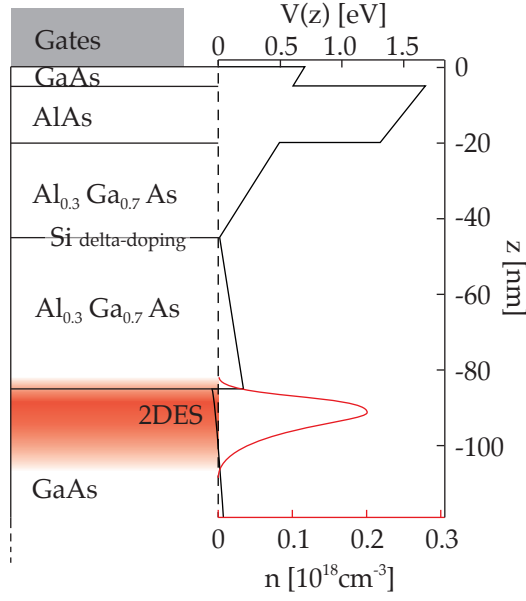


Figure 6.19.: The electron density distribution in the z -direction of a 2DEG. This plot was taken from [28].

and

$$H_1 = \frac{1}{2} \sum_{\sigma_1, \sigma_2} \int d^3x d^3y V(x-y) \psi_{\sigma_1}^\dagger(x) \psi_{\sigma_2}^\dagger(y) \psi_{\sigma_2}(y) \psi_{\sigma_1}(x), \quad (6.8)$$

where T is the matrix element of the kinetic and $U(x)$ the matrix element of the potential energy, while $V(x-y)$ denotes the matrix elements of the interaction. In our case, we take the potential $U(x, y)$ in the x, y -plane to be

$$U(x, y) = U_0 - \frac{1}{2} m \omega_x^2 x^2 + \frac{1}{2} m \omega_y^2 y^2, \quad (6.9)$$

which is of the saddle point form mentioned above and we further assume a very narrow constriction in z -direction. Of course, this is a simplification and in a realistic material the density profile is of a form like depicted in fig. 6.19.

For the eigenfunctions of the non-interacting Hamiltonian we can make the separation of variable ansatz

$$\Psi(x_1, x_2, x_3) = \psi(x_1) \phi_n(x_2) \tilde{\phi}_m(x_3), \quad (6.10)$$

where we assume to have quantized eigenfunctions $\phi_n(x_2)$ and $\tilde{\phi}_m(x_3)$ in y - and z -direction. If we now make a basis transformation by changing the y - and z -components from the spatial- into the eigenbasis

$$|x_1\rangle \otimes |x_2\rangle \otimes |x_3\rangle \rightarrow |x_1\rangle \otimes |\phi_n\rangle \otimes |\tilde{\phi}_m\rangle, \quad (6.11)$$

we can transform the interaction term H_1 accordingly:

$$\begin{aligned}
H_1 = & \frac{1}{2} \sum_{\sigma_1 \sigma_2} \int dx_1 dx_2 dx_3 \int dy_1 dy_2 dy_3 \langle x_1, x_2, x_3 | V | y_1, y_2, y_3 \rangle \\
& \times \left[\sum_{m,n} (\langle x_1 | \otimes \langle \phi_n | \otimes \langle \tilde{\phi}_m |) (|x_1\rangle \otimes |x_2\rangle \otimes |x_3\rangle) a_{\sigma_1}^\dagger(x_1, \phi_n, \tilde{\phi}_m) \right] \\
& \times \left[\sum_{m,n} (\langle y_1 | \otimes \langle \phi_n | \otimes \langle \tilde{\phi}_m |) (|y_1\rangle \otimes |y_2\rangle \otimes |y_3\rangle) a_{\sigma_2}^\dagger(y_1, \phi_n, \tilde{\phi}_m) \right] \\
& \times \left[\sum_{m,n} (\langle y_1 | \otimes \langle y_2 | \otimes \langle y_3 |) (|y_1\rangle \otimes |\phi_n\rangle \otimes |\tilde{\phi}_m\rangle) a_{\sigma_2}(y_1, \phi_n, \tilde{\phi}_m) \right] \\
& \times \left[\sum_{m,n} (\langle x_1 | \otimes \langle x_2 | \otimes \langle x_3 |) (|x_1\rangle \otimes |\phi_n\rangle \otimes |\tilde{\phi}_m\rangle) a_{\sigma_1}(x_1, \phi_n, \tilde{\phi}_m) \right].
\end{aligned} \tag{6.12}$$

Since we are only interested in the low energy physics, we can take in all of the summations above only the eigenfunctions of the lowest energy. This would be $\phi_0(y)$ in y -direction:

$$\phi_0(y) = \langle y | \phi_0 \rangle = \frac{1}{\pi^{1/4} \sqrt{l_2}} e^{-y^2/2l_2^2}, \tag{6.13}$$

which is simply the ground state wavefunction of a harmonic oscillator with characteristic length l_2 and and in z -direction

$$\langle z | \tilde{\phi}_0 \rangle = \tilde{\phi}_0(z) = \delta(z). \tag{6.14}$$

As we have said above, we take here a δ -function for $\tilde{\phi}_0$ according to the assumption of a very thin 2DEG, only having a small extent in the z -direction. We end up with

$$\begin{aligned}
H_1 = & \frac{1}{2} \sum_{\sigma_1 \sigma_2} \int dx_1 dx_2 dx_3 \int dy_1 dy_2 dy_3 \langle x_1, x_2, x_3 | V | y_1, y_2, y_3 \rangle \\
& \times |\langle \phi_0 | x_2 \rangle|^2 \cdot |\langle \tilde{\phi}_0 | x_3 \rangle|^2 \cdot |\langle \phi_0 | y_2 \rangle|^2 \cdot |\langle \tilde{\phi}_0 | y_3 \rangle|^2 \\
& \times \underbrace{a_{\sigma_1}^\dagger(x_1, \phi_0, \tilde{\phi}_0)}_{=:\psi_{\sigma_1}^\dagger(x_1)} \underbrace{a_{\sigma_2}^\dagger(y_1, \phi_0, \tilde{\phi}_0)}_{=:\psi_{\sigma_2}^\dagger(y_1)} \underbrace{a_{\sigma_2}(y_1, \phi_0, \tilde{\phi}_0)}_{=:\psi_{\sigma_2}(y_1)} \underbrace{a_{\sigma_1}(x_1, \phi_0, \tilde{\phi}_0)}_{=:\psi_{\sigma_1}(x_1)}
\end{aligned} \tag{6.15}$$

and thus finally arrive at an effective one-dimensional model

$$\begin{aligned}
H_1 = & \frac{1}{2} \sum_{\sigma_1 \sigma_2} \int dx_1 \int dy_1 \left[\int dx_2 dx_3 \int dy_2 dy_3 \langle x_1, x_2, x_3 | V | y_1, y_2, y_3 \rangle \right. \\
& \left. |\langle \phi_0 | x_2 \rangle|^2 \cdot |\langle \tilde{\phi}_0 | x_3 \rangle|^2 \cdot |\langle \phi_0 | y_2 \rangle|^2 \cdot |\langle \tilde{\phi}_0 | y_3 \rangle|^2 \right] \\
& \psi_{\sigma_1}^\dagger(x_1) \psi_{\sigma_2}^\dagger(y_1) \psi_{\sigma_2}(y_1) \psi_{\sigma_1}(x_1) \\
= & \frac{1}{2} \sum_{\sigma_1 \sigma_2} W(x_1, y_1) \psi_{\sigma_1}^\dagger(x_1) \psi_{\sigma_2}^\dagger(y_1) \psi_{\sigma_2}(y_1) \psi_{\sigma_1}(x_1).
\end{aligned} \tag{6.16}$$

Within our above approximation for the lowest eigenfunctions $\phi_0(y) = \frac{1}{\pi^{1/4}\sqrt{l_2}}e^{-y^2/2l_2^2}$ and $\tilde{\phi}_0(z) = \delta(z)$, the expression for $W(x_1, y_1)$ can be calculated analytically:

$$\begin{aligned}
W(x_1, y_1) &= \int dx_2 dx_3 \int dy_2 dy_3 \\
&\quad \times \frac{1}{\sqrt{(x_1 - y_1)^2 + (x_2 - y_2)^2 + (x_3 - y_3)^2}} \cdot \delta(x_3)\delta(y_3) \cdot \left(\frac{e^{-x_2^2/2l_2^2}}{\pi^{1/4}\sqrt{l_2}}\right)^2 \left(\frac{e^{-y_2^2/2l_2^2}}{\pi^{1/4}\sqrt{l_2}}\right)^2 \\
&= \frac{e^2}{\pi l_2^2} \int_{-\infty}^{\infty} dx_2 dy_2 \frac{e^{-(x_2^2+y_2^2)/l_2^2}}{\sqrt{(x_1 - y_1)^2 + (x_2 - y_2)^2}} \\
&= \frac{e^2}{2\pi l_2^2} \int_{-\infty}^{\infty} dr dR \frac{e^{-(r^2+R^2)/2l_2^2}}{\sqrt{(x_1 - y_1)^2 + r^2}} \\
&= \frac{e^2}{\pi l_2^2} \left(\int_{-\infty}^{\infty} dR e^{-R^2/2l_2^2} \right) \cdot \int_0^{\infty} dr \frac{e^{-r^2/2l_2^2}}{\sqrt{(x_1 - y_1)^2 + r^2}}.
\end{aligned} \tag{6.17}$$

The first integral is of gaussian form and yields a factor of $\sqrt{2\pi}l_2$. The second one is also elementary and yields (see [29])

$$\int_0^{\infty} dr \frac{e^{-r^2/2l_2^2}}{\sqrt{(x_1 - y_1)^2 + r^2}} = \frac{1}{2} e^{(x_1 - y_1)^2/4l_2^2} K_0 \left(\frac{(x_1 - y_1)^2}{4l_2^2} \right), \tag{6.18}$$

where K_0 denotes the 0-th order modified Bessel function of the second kind. Thus, we end up with

$$W(x_1, y_1) = \frac{e^2}{\sqrt{2\pi}l_2} e^{(x_1 - y_1)^2/4l_2^2} K_0 \left(\frac{(x_1 - y_1)^2}{4l_2^2} \right). \tag{6.19}$$

Since we measure in our one dimensional system the distances x_1 and y_1 in units of the characteristic length $l_x = \frac{\hbar}{\sqrt{m\Omega_x}}$, it is actually the ratio l_2/l_x that defines the amplitude of the interaction modification due to l_2 . To illustrate this further, we have compared in fig. 6.20 the functional dependence of the off-site interaction for several values of l_2 with the pure Coulomb interaction which one would obtain by setting in our earlier derivation $\phi_0(y) = \delta(y)$. We see that for $l_2 \rightarrow 0$ the l_2 -dependent curves converge against the Coulomb interaction, as it should be. Furthermore, we notice that the main difference between the two interactions lies in the central region around $x = 0$, whereas the outer tails become quickly the same. In our modeling, this will cause the differences in U to be mainly in the nearest neighbour interaction. Here, it may be a good time to make a final comment on the choice of the eigenfunction $\tilde{\phi}_0(z)$ in z -direction. Till this point, we have assumed this function to be δ -like, but of course the 2DEG is not entirely two dimensional but has also some small extent in z -direction, compare fig. 6.19. Of course, one can also try to model this, for example with an infinite square well of length l_3 . In principle all we have to do, is to set in formula (6.15)

$$|\langle \tilde{\phi}_0 | x_3 \rangle|^2 = \frac{2}{l_3} \sin^2 \left(\frac{x_3}{l_3} \right), \quad |\langle \tilde{\phi}_0 | y_3 \rangle|^2 = \frac{2}{l_3} \sin^2 \left(\frac{y_3}{l_3} \right), \tag{6.20}$$

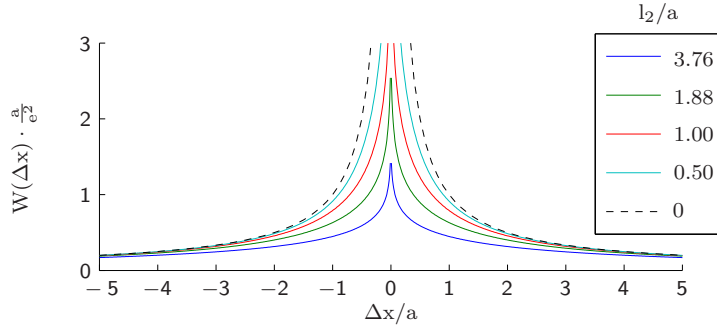


Figure 6.20.: The interaction strength $W_{l_2}(x_1 - y_1) =: W_{l_2}(\Delta x)$ plotted for several values of the characteristic length in y -direction l_2 . Note that the curves differ in their divergence at $\Delta x = 0$ but that they have asymptotically the same tail, namely the Coulomb one. Furthermore, for decreasing l_2 the curves converge against the case $l_2 = 0$ which is a pure Coulomb interaction.

which are just the groundstate probability densities of the infinite square well. Then we can do the same calculation as above and end up with

$$\begin{aligned} \tilde{W}(x_1, y_1) &= \frac{e^2}{\sqrt{2\pi}} \int dx_3 \int dy_3 \frac{1}{l_2} \frac{4}{l_3^2} \sin^2\left(\frac{x_3}{l_3}\right) \sin^2\left(\frac{y_3}{l_3}\right) \\ &\quad \times e^{[(x_1 - y_1)^2 + (x_3 - y_3)^2]/4l_2^2} K_0 \left[\frac{(x_1 - y_1)^2 + (x_3 - y_3)^2}{4l_2^2} \right]. \end{aligned} \quad (6.21)$$

This integral could now be calculated numerically. We won't do this here, but just notice that this would lead to a further decrease in our interaction strength since $M(x) := e^x K_0(x)$ is monotone decreasing in x :

$$M \left[\frac{(x_1 - y_1)^2 + (x_3 - y_3)^2}{4l_2^2} \right] < M \left[\frac{(x_1 - y_1)^2}{4l_2^2} \right]. \quad (6.22)$$

Due to the form of $M(x)$ (see fig. 6.20), this decrease will be again most significant in the central region.

Last but not least, we have to take into account the screening effect of the surrounding gates. This stems from the fact that in an experimental environment we have to induce our desired potentials by charging electrodes in the structure. The electrons which occupy these gates will then redistribute themselves in order to screen the interaction of the electrons in our effective one dimensional system. The main effect of this screening will be to cut the tail of the effective interaction calculated above.

For the practical purpose of modeling our system, we have chosen to condense our above results in the following way: In our discretized interaction, we can choose first the interaction strength on the central site ($\Delta x = 0$) U_0 and the first off-site ($\Delta x = 1$) U_1 , see fig. 6.21. The rest of the interaction is then given by the form derived above:

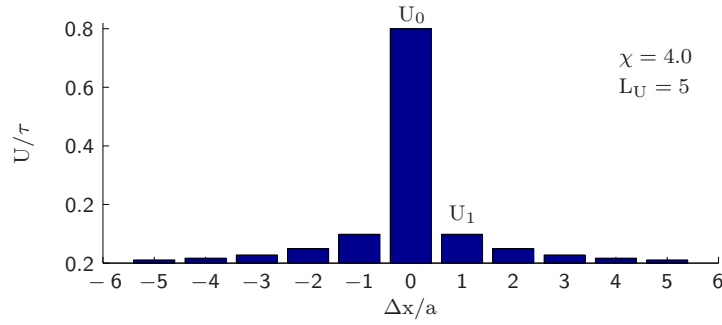


Figure 6.21.: The discretized interaction as used in our calculations. The values of the on- and first off-site interaction where here $U_0 = 0.8\tau$ and $U_1 = 0.2\tau$. At this point, we use units of τ for the interaction instead of $\sqrt{\Omega_x\tau}$ since we have not yet specified the curvature of our QPC.

$$U_1 \cdot \frac{1}{\sqrt{2\pi}l_2} e^{x^2/4l_2^2} K_0\left(\frac{x^2}{4l_2^2}\right) \cdot e^{-x/\chi}, \quad (6.23)$$

i.e. an interaction of the form $M_{l_2}(x) = \frac{1}{\sqrt{2\pi}l_2} e^{x^2/4l_2^2} K_0\left(\frac{x^2}{4l_2^2}\right)$, with an cutoff $e^{-x/\chi}$ to model the screening of the surrounding gates. In the following, we will refer to this interaction as the M -type. Furthermore, we introduce another parameter L_U with which we can regulate the range of the bare interaction. L_U just gives the maximal interaction range, i.e. $U(i, j) = 0$ for all i, j with $|i - j| > L_U$. The influence of these scales can be seen in fig. 6.21. An ideal realization of the scales should be in a range according to $\chi \ll L_U \ll L \ll 2N + 1$. The limiting quantities in our implementation are clearly the feedback range L and the number of sites $2N + 1$, since the computation time scales in leading order like $L^3 \cdot (2N + 1)^3$. In our usual setup of a central region consisting of $2N + 1 = 81$ sites, our maximal achieved L was 30 sites. In this regime, the integration of the fRG-flow, for moderate parameters took up computation time in the range of $\sim 8h - 10h$.

6.2.1. Results for longer ranged interactions

Let us now look at the results we obtained here. First, we choose a moderate screening $\chi \sim 5$ and look at the development of the conductance with the interaction strength U and with varying our parameter l_2 from a Coulomb- to a M -type form with an larger l_2 , see fig. 6.22

We observe that there are mainly two parameter regimes, determined by the strength of the off-site interaction U_1 . In the first regime where $U_1/\Omega_x \lesssim 0.37 - 0.75$ which are essentially the first 3-4 curves in fig. 6.22, changing l_2 will only slightly modify the shape of the conductance, but in sensible bounds it does not affect the physics too much. This indeed justifies *a posteriori* in this parameter regime the previous modeling of the QPC by using just a pure Onsite interaction: The specific form of the interaction on the first

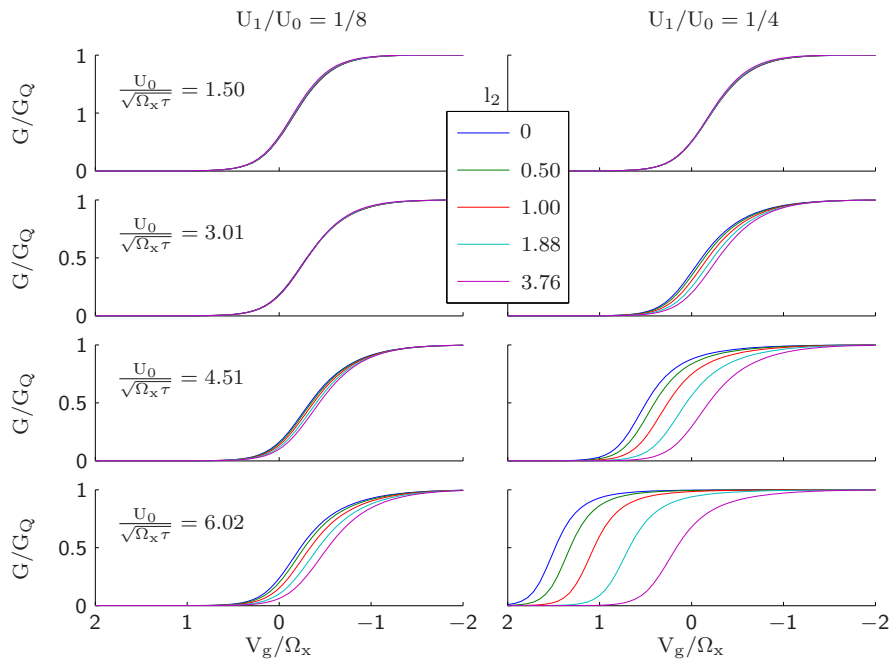


Figure 6.22.: Conductance curves for longer ranged interactions, using the parameters $L = 15$, $\chi = 5.0$, $L_U = 10$, as well as different values for U_0 and l_2 . We have plotted curves for the two ratios of $U_1/U_0 = 1/8$ and $U_1/U_0 = 1/4$. Note that in the first three plots the conductance curves for different l_2 are essentially the same while in the latter plots they considerably differ. Also the conductance itself, independent of which value of l_2 we choose shows a peculiar behavior in dependence of the off-site interaction strength, as it is shifted to larger V_g values when $U_1/\sqrt{\Omega_x\tau}$ is increased over $\approx 0.37 - 0.75$.

few neighbouring sites is not too important. The agreement of the onsite results with the experimental data (cf. [1]) is clear evidence for that.

We will not concern us further with this regime, but look at the entirely different behavior which manifests itself when we increase U_1 beyond the mentioned limit. Here, we get large shifts for the conductance curves when we change U_1 . Also, irrespectively what exact value of U_1 we take, we get huge deviations between the curves for the same interaction strength U_1 but with different l_2 . This is actually consistent since the effect of changing l_2 lies mainly in an effective change of the interaction strength U_1 on the first few off-sites. In the last three of the above diagrams, we can see a somewhat strange development in the conductance with increasing the interaction strength U : The pinch-off V_s of the conductance curve is shifted to larger V_g values, i.e. in this regime the increase in interaction strength improves the conductance of our system. In the last plot of fig. 6.22 this shift becomes very large, actually the pinch-off of the conductance is increased beyond the non interacting one.

This behavior looks of course enormously strange, since from a physical point of view interactions should naturally increase the effective barrier height, i.e. the barrier height the electrons would see in an effective system when the interactions are integrated out. Before studying this behavior further (in the following we will refer to this as "the effect"), let us first take a look at the other observables.

For the susceptibility we show the results for the Coulomb case $l_2 = 0$ and the case $l_2 = 1.88$, see fig. 6.23. This $l_2 = \frac{1}{2}l_x$ may seem still a bit large but was chosen to make the difference to the Coulomb case clearly visible, even if this might in physical terms not be the most appropriate choice. We see that the susceptibility reflects the same behavior observed in the conductance. At an off-site interaction strength $U_1/\sqrt{\Omega_x\tau} \approx 0.37 - 0.75$, the susceptibility starts to decrease with increasing offsite interaction strength. This is consistent with the effect we have seen in the conductance since the susceptibility is always largest in the sub-open regime (cf. fig. 5.12 and fig. 6.3) and this regime is shifted with increasing U_1 to larger V_g values. Independent of the amplitude of χ this is also reflected in the form of the susceptibility. If we look, e.g. at the plot with $U_1/U_0 = 1/4$ and $l_2 = 0$, we see that we start at $U_0/\sqrt{\Omega_x\tau} = 1.5 \Rightarrow U_1/\sqrt{\Omega_x\tau} = 0.375$ with the characteristic double peak of the sub-open regime (due to the form of the LDOS). With increasing U_1 this structure develops into the single peak of the open regime.

And for completeness we also show here the dependence of the conductance on the external magnetic field, see fig. 6.24. This seems to depict pretty much the same behavior as we had already known: the 0.7 shoulder develops into a spin split plateau with increasing the magnetic field strength B . We note here, however, the following interesting property. As before, an increase in $U_1/\sqrt{\Omega_x\tau}$ around 0.75 seems to shift the onset point for the spin up species to slightly higher V_g values. However, the down species shows the behavior one would intuitively expect, namely a shift to lower V_g values with increasing interaction strength. We will further comment on this below when we have introduced a possible explanation for this strange effect.

Now, we take a closer look at how this effect works. Since we have already seen that it seems to depend mainly on the strength of U_1 , we set in the following analysis for

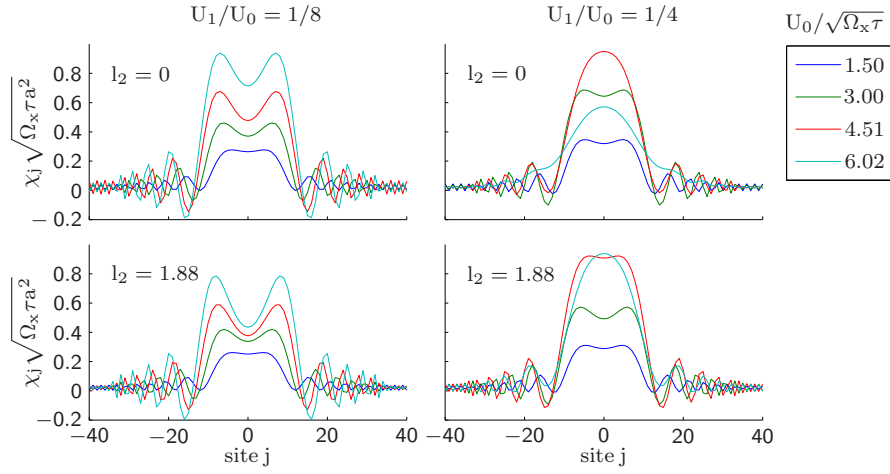


Figure 6.23.: The local susceptibilities for $l_2 = 0$ and $l_2 = 1.88$ at a value of $V_g/\Omega_x = -0.36$ plotted for the same values of U_0 and U_1 as above. Note that the susceptibility reflects the same behavior as the conductance above: around the point $U_1/\sqrt{\Omega_x\tau} \approx 0.75$ the susceptibility starts to decrease with increasing the off-site interaction strength due to a shift of the sub-open regime in the gate voltage V_g .

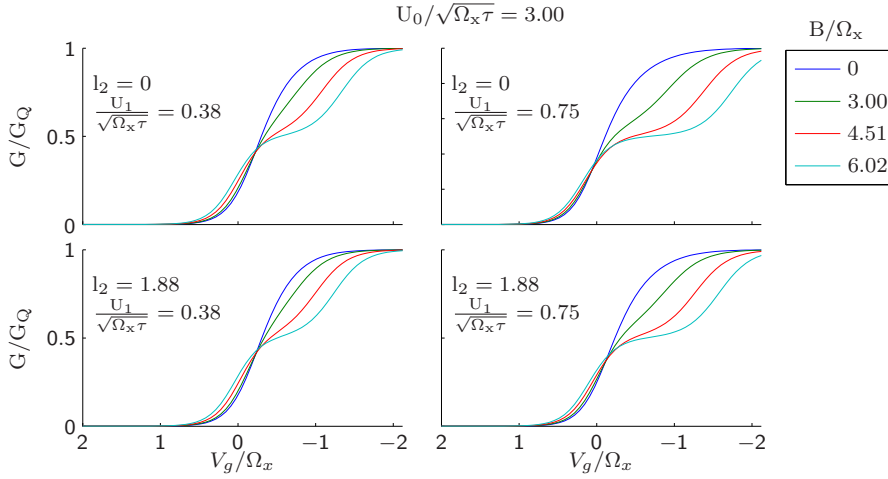


Figure 6.24.: The conductance plotted against gate voltage for several values of B in the Coulomb and the case where $l_2 = 1.88$, as above. We applied here a mediocre on-site interaction strength $U_0/\sqrt{\Omega_x\tau} = 3.00$ and off-site strengths $U_1/\sqrt{\Omega_x\tau} = 0.1/0.2$.

simplicity $l_2 = 0$, therefore setting the effective one dimensional interaction to a pure Coulomb one. Furthermore, we choose $\chi = 10^5$, rendering the screening to be essentially inexistent and thus giving the off-site interaction the most weight, increasing the effect. At this point, we will first make a technical comment on our method. Using static fRG we have obtained an effective system where we have mapped $H_0 + H_{int} \rightarrow H_{eff} = H_0 + \Sigma$, assuming the 1PI two-particle vertices and thus also the selfenergy to be frequency independent and the higher order vertices to be zero. In order to determine the cause of the effect, we will study this effective system more closely. However, we should mention that, at this point, it is not completely clear how this effect can arise physically although we will take an educated guess on this later. Provided we made no mistake in our calculations, it could of course be that this strange behavior is an artifact of the approximations we have made. This type of shift in the conductance pinch-off to larger V_g values was for example observed also in the so called "fRG1-scheme", where one neglected the flow of the two particle vertex entirely. In our case we applied static fRG and thus the two particle vertex and the self energy are frequency independent. Due to this frequency independence of the self energy we in fact map here the interacting system to a effective non-interacting one, as mentioned above. This approximation works fine when pure on-site interactions are used (see [19]). In fact, it was shown there that the dynamical fRG-scheme had no real advantage over the static one. Now, a system with longer ranged interactions could be classified as somewhat "more interacting" and thus one could suspect to loose more of the original behavior by mapping it onto a effective non-interacting system.

For the moment, we will put this technical considerations aside and just study the different physical observables in this parameter regime a bit closer. First we look again at the conductance, but now we specifically study the transition point of the two U_1 regimes, see fig. 6.25. By increasing U_1 beginning from very small values of the gate voltage, we see that the conductance follows at first the behavior one would expect from the first order Hartree term: the larger U_1 becomes the more is the pinch-off shifted to lower V_g values and the 0.7 shoulder becomes more pronounced. However, at the point $U_1/\sqrt{\Omega_x\tau} \approx 0.56$ the conductance begins suddenly to shift to larger V_g values. By looking at the self energy, cf. fig. 6.26, one can clearly see where the mysterious shift in the conductance stems from. Compared to the on-site interacting case, the self-energy in the central region is slightly smaller. Thus, in our effective system with off-site interaction it is for an electron more attractive to sit in the center of the QPC than in the pure on-site interacting system. In the last plot of fig. 6.26 the self-energy in the central region even becomes slightly negative, implying that the barrier top becomes even more attractive than in a non interacting system.

Let us look if this behavior can be supported by studying the density in the sub-open region, see fig. 6.27. Generally, the longer ranged interactions seem to massively deplete the flanks of the QPC, but in the right parameter regime they (more or less) slightly increase the density in the central region. For some physical insight, it might be instructive to think of our QPC to be first interaction free and than imagine that we can turn on our interactions on demand. If we look again at the density in the non

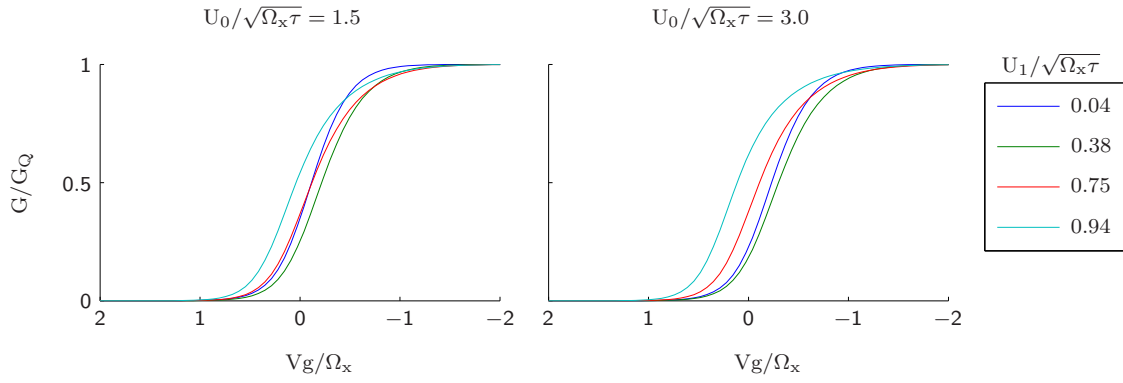


Figure 6.25.: The conductance curves for the on-site interaction strengths $U_0/\sqrt{\Omega_x\tau} = 1.5$ and $U_0/\sqrt{\Omega_x\tau} = 3.0$ for increasing the off-site interaction U_1 beginning from very small values. Note that by increasing U_1 the conductance behaves up to a certain point as if we would simply increase the on-site interaction: it shifts to lower V_g -values and develops the 0.7-shoulder. However, when $U_1/\sqrt{\Omega_x\tau}$ is raised above approximately 0.56 the conductance begins to shift to larger V_g -values. This is different from the on-site case, where increasing the interaction always leads to a shift to lower V_g -values.

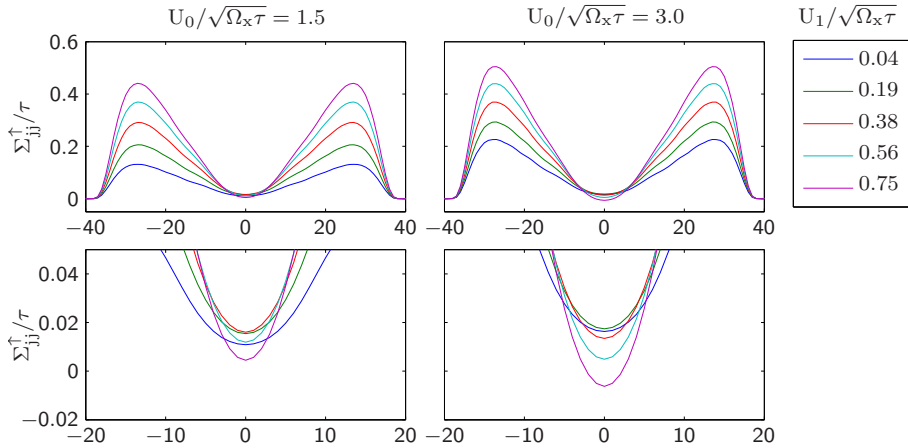


Figure 6.26.: First row: The main diagonals of the self-energies, plotted for the same parameters as the conductance curves above. We used here a gate voltage of $V_g/\Omega_x = -0.17$ which lies in the conductance step of our above curves. Second row: The same curves but only the central region. Note that in the parameter regime where we observe the strange shift in the conductance, the diagonal part of the self-energy becomes smaller in the center with increasing off-site interaction strength. In the curve for $U_0/\sqrt{\Omega_x\tau} = 3.0$ and $U_1/\sqrt{\Omega_x\tau} = 0.75$ this central part even becomes negative (!)

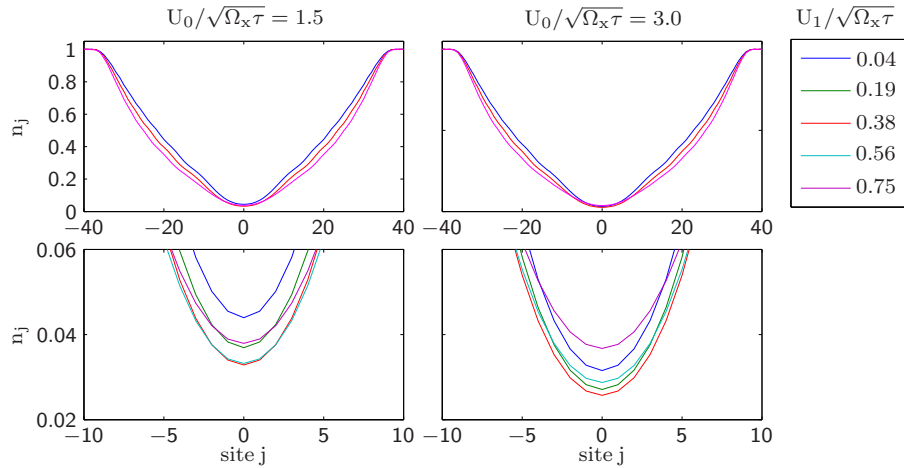


Figure 6.27.: First row: The electron density n_j plotted for our usual parameters and again a gate voltage of $V_g/\Omega_x = -0.17$. For clarity, we plotted here only the curves for $U_1/\sqrt{\Omega_x\tau}$ equal to 0.04, 0.38 and 0.75. Second row: The same curves again but only the central region. Here, in the density we note a effect which is consistent with the one observed in the self-energy and conductance: For $U_1/\sqrt{\Omega_x\tau} \gtrsim 0.56$ the electron density in the central region starts to become larger with rising the off-site interaction strength.

interacting case, cf. fig. 5.11, we see that the density in the flanks is significantly higher than in the center. It makes sense that turning on interactions, especially ones with longer ranges, should here increase the selfenergy to a large amount. This is, indeed, visible in the above plots and leads to a massive depletion of the density in the flanks of the QPC. Most of the electrons will, of course, simply leave the interacting region and escape in the leads. But according to the plots of the density there seem to be some electrons which instead increase the density in the center of the QPC. An attempt to think about this would be to assume that at a certain value of the off-site interaction a electron can enter the center of the QPC, since it is energetically more favorable to actually sit on the barrier top and escape thus the interaction with the other electrons, giving rise to a Wigner like crystallization effect (cf. [30]). We have illustrated this effect in the sketch below, see fig. 6.28.

This picture is somewhat supported, when one looks at the development of the density minimum in the center of the QPC as a function of gate voltage, see fig. 6.29. As a comparison, we have plotted the same curves for the longer ranged and the on-site interaction case. We see that at a certain gate voltage the density minimum rises very fast up to a certain point and then continues to increase almost linearly in gate voltage. In contrast, for the on-site interaction the rise of the density minimum is more or less linearly all the time. This indicates that in the case of longer ranged interactions there is indeed a gate voltage where a certain amount of charge can enter the QPC at once leading to the steep increase in density. By further lowering the gate voltage, the density

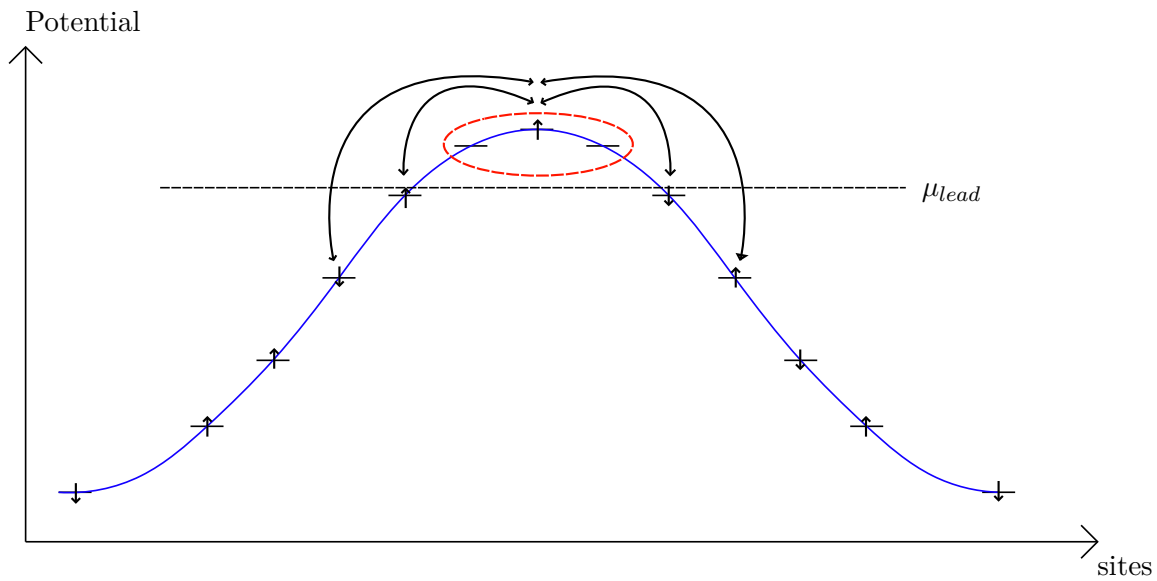


Figure 6.28.: Graphical depiction of our speculation: due to longer ranged interactions with the bulk a single electron is able to enter the central region (here depicted in red) of the QPC at a much higher gate voltage than in the pure onsite interacting case.

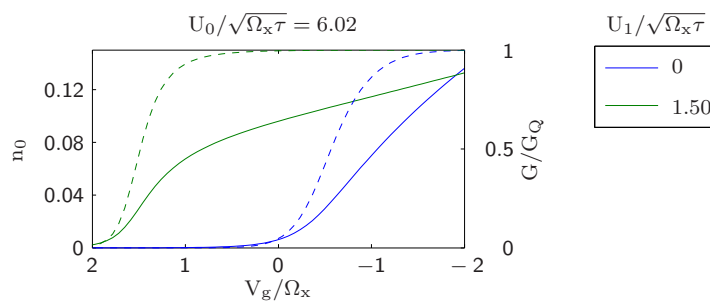


Figure 6.29.: The density n_0 at the center of the QPC (solid lines) and the corresponding conductance (dashed lines) as a function of gate voltage. We plotted here the curves for a pure onsite interaction $U_0/\sqrt{\Omega_x\tau} = 6.02$, and a curve with the same onsite interaction and an rather strong off-site interaction $U_1/\sqrt{\Omega_x\tau} = 1.5$. First, notice that we observe the same shift to lower gate voltage in the density as in the conductance. Furthermore, note that in the pure on-site case the slope of the density curve increases up to a certain point and stays then almost constant. In contrast, the density curve with off-site interaction increases rather steep up to a certain point (here ≈ 0.07) and then continues to grow in a much slower pace.

minimum develops then the almost linear dependence which is also seen in the other case.

To study this further, we have additionally summed the density over different "inner areas" of the QPC: $n_{\text{Int}} = \sum_{j=-k}^k n_j$, where the extent of this inner region is determined by k . If we then study this summed density as a function of gate voltage, we can see essentially the same behavior as in the minimum of the conductance. The hope was, of course, to see some sort of real discretization in the number of electrons which enter the QPC. However, such a statement is hard to make since it is not really clear how the size of the inner area, i.e the extent of the barrier top of the QPC should be defined. For our above plot fig. 6.29, we would have to choose the number of central sites equal to $2k + 1 = 13$ such that we would obtain by integration over that area a curve for n_{Int} in V_g which has it's kink exactly at one electron. In principle, the size of the central region of the QPC should be given by the characteristic length of our system as well as the range scale of the interactions. In our case, both those scales where of the order of the diameter $k = 6$ of the inner region: the characteristic length of our system was here, as always, $l_x = 3.76$ sites and the range scale of the interaction could be determined approximately by the screening length $\chi = 5.0$. Of course, we didn't scale here the interactions between the different cases and we didn't try to define some weight in the interaction. This would be a interesting topic of further study.

In the next two sections, we will study again the on-site model for QPCs with higher order potentials and the transition between a QPC and a QD.

6.3. Higher order potentials for QPCs

At the end of this chapter, we show some results which we have obtained using the pure on-site interaction. Our previous comparison between the two algorithms suggested that the new method with longer ranged feedback is more stable in regimes where the older algorithm did not converge. Thus, we looked here especially on phenomena which occur in difficult regions of parameter space. One particular of this situations arises if one considers potentials which are not purely parabolic. In this case, one encounters in the non-interacting case Fabry-Perot like resonances (see Heyder et al. [31]) and is in the case of on-site interactions in general very fast at the divergence point of fRG. We will here successively show results for quartic, sextic, and octic potential barriers. As far as we know, the tunneling problem through those non quadratic barriers is not solved analytically, yet there are various approximation schemes like WKB or instanton approximations. However, we will here simply accept the form of the non-interacting conductance as it is obtained by our numerical approach and just look at it's development when we turn on interactions. Nevertheless, to plot the quantities in their respectively natural units one can make again a nondimensionalization as done in chapter 5 for the quadratic barrier. Completely analogous, we end here up with the natural parametrization of the potential

$$V^{(n)} = V_g + 2\tau + \mu - \Omega_x \left(\frac{x}{2l_x} \right)^n, \quad l_x = \sqrt{\frac{\hbar^2}{2m\Omega_x}}. \quad (6.24)$$

where again l_x gives the characteristic length scale and Ω_x determines the natural energy scale.

For our concrete potential barrier we have chosen the form

$$V(j) = (\mu + V_g + 2\tau) \exp\left(-\frac{\left(\frac{j}{N}\right)^n}{\left(1 - \left(\frac{j}{N}\right)^2\right)}\right), \quad (6.25)$$

which leads by comparison with (6.24) using the same approximations as in chapter 5 to a approximate curvature of

$$\Omega_x = \left(\frac{2^{n+1}}{N^n}\right)^{\frac{2}{2+n}} \tau. \quad (6.26)$$

Below we have plotted our results for some potential forms, see fig. 6.30 - fig. 6.32.

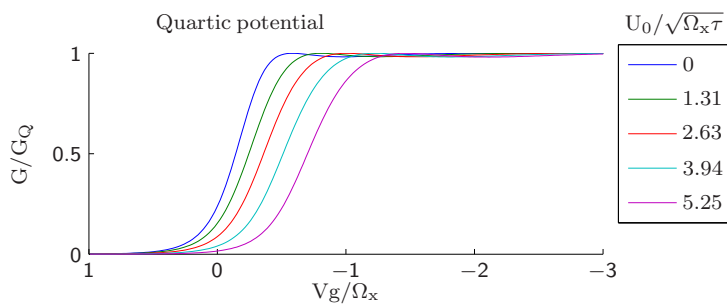


Figure 6.30.: The conductance curves of a quartic barrier QPC plotted against gate voltage for increasing on-site interaction strength $U_0/\sqrt{\Omega_x\tau}$. Note that there are -in contrast to the pure parabolic case- some "wiggles" in the conductance plateau. As the interaction is increased, the conductance is shifted to lower gate voltages and becomes less steep, while the qualitative behavior seems to stay the same.

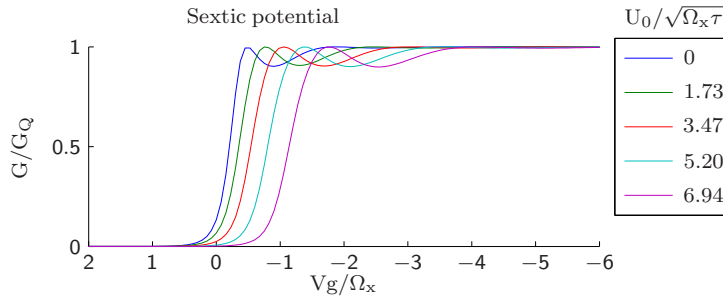


Figure 6.31.: Same plot as above but for an sextic barrier top. Note that the "wiggles" to which we refer as Fabry-Perot like resonances become more pronounced while the behavior that occurs when we increase the interaction strength $U_0/\sqrt{\Omega_x\tau}$ seems to stay the same: the conductance step is broadened, as is the structure of the Fabry-Perot resonances.

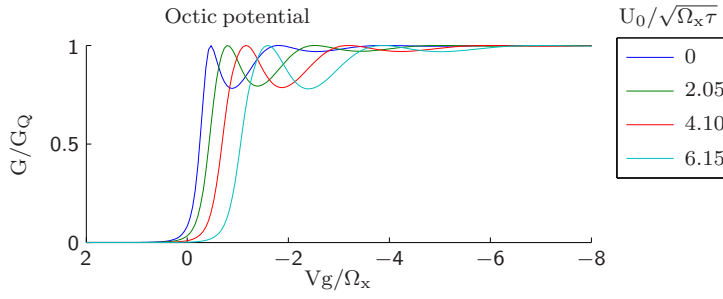


Figure 6.32.: At last the plot for an octic barrier top. We observe again the qualitative behavior as in the last two plots.

We observe that the conductance develops some "wiggles", following the first reach of the conductance maximum $1 \cdot G_Q$. As in [31] by Heyder et. al, we shall refer to them as Fabry-Perot like resonances. With increasing the interaction strength U_0 the conductance step and the structure of the Fabry-Perot like resonances broadens up and gets shifted to lower gate voltage.

A more detailed study of these phenomena, however, is beyond the scope of this work.

6.4. Transition between QPC and quantum dot

At the very end of this master thesis, we consider once more a situation which was point of earlier research, namely the transition between a quantum point contact and a quantum dot. During this transition we deform the QPC by indenting the barrier top till it becomes a valley, see the figure below. This potential structure leads to an entirely different non-interacting LDOS than the one observed before in the QPC case, cf. fig. 5.4.

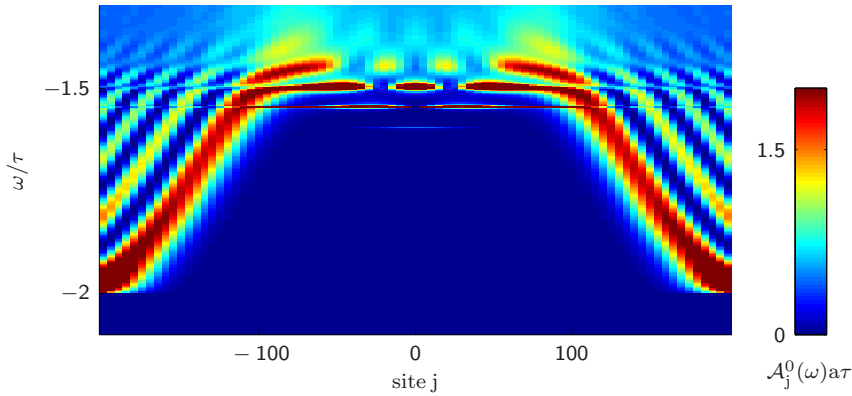


Figure 6.33.: The non-interacting LDOS for a quantum dot potential. As explained later, the chemical potential was here chosen to be $\mu = -1.5\tau$. Note that in difference to the previous QPC we have discrete levels representing bound states inside the QD. The potential was here chosen as the green one from fig. 6.35.

Instead of the ridge like structure with the large apex seen in our plot in fig. 5.4, we get additionally to the continuous part of the spectrum discrete levels, corresponding to bound states in the dot. In a non-interacting picture, we will get a conductance peak whenever an effective level of a bound state in the LDOS crosses the chemical potential, i.e. whenever the occupation of the dot changes by two electrons (each bound state can host two electrons with opposite spins). However, when interactions are turned on, these levels split up due to the energy difference between a single occupied and a double occupied state. When we lower now the gate voltage, the dot will be filled up one by one with electrons. As in the non-interacting case one gets a conductance peak whenever one of those levels crosses the chemical potential and the occupation number changes by one. However, there arises an additional feature: between each of those levels where the occupation of the dot is an odd number of electrons, i.e. if there is a single occupied level in the quantum dot ("odd valley") we get also conductance, whereas in the even valleys the conductance stays zero. This behavior is known as the Kondo effect in quantum dots and is in fact closely related to the "original" Kondo effect, described by Kondo in [32]. The main reason for this effect was identified as the spin degeneracy in the single occupied level in the dot. This degeneracy enables resonant spin-flip electron scattering and leads to conductance $G = G_Q$ in the odd valleys between the peaks. A sort of "toy model" for this is the single impurity Anderson model (SIAM), where one can observe a very "clean" Kondo effect. In the fRG framework this was done, e.g., by C. Karrasch in [13]. However, Kondo physics will also appear in our model introduced above. Recently, Heyder et al. [31] used our above chain model to study the transition between a quantum dot and a QPC, by applying the deformation of the potential described above. Since fRG suffers from convergence problems when the barrier top of the used potential becomes too flat, their transition was done in the following way. First they observed the QPC

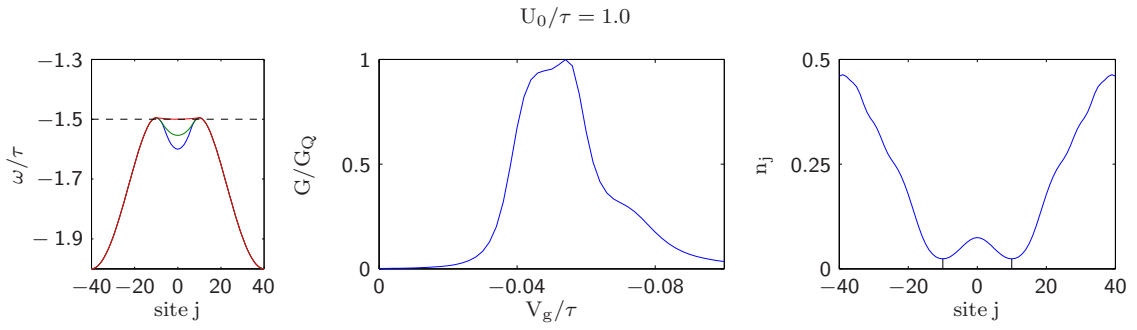


Figure 6.34.: The transition from a QPC to a QD hosting one electron. We have here chosen a width $w_d = 20$ sites of the dot and a side gate voltage of 0.007. Left: The actual development of the potential shape with gate voltage V_g . The blue and the red curve indicate the final and the initial potential form, respectively, while the green curve indicates the potential at the gate voltage in the middle of the Kondo plateau (see the plot in the middle). Note that the chemical potential was here set to -1.5τ . This was done in order to enable us to have a relative long and flat barrier top without making the flanks of the QD to steep, causing a non adiabatic change in the barrier. Middle: The conductance plotted against gate voltage, sweeping over the first Kondo plateau. Right: Plot of the density in the QD at the same gate voltage as the green curve in the potential plot. As guide for the eye, black lines indicate the position of the minima in the density.

in the sub-open regime. Then changing the potential form they applied a simultaneous shift in the gate voltage V_g tuning the QPC in the open regime when the transition is in the state of the flat barrier top and ending up at a QD which may or may not be open, depending on its actual filling with electrons. In our case we will not change the site gate voltage during the transition thus always staying in the region where the flat barrier top is close to the chemical potential. This transition could not be tackled via fRG in the old method, since due to the flat potential at the center of the interacting region during the crossover the convergence was not given. Furthermore, Heyder et al. used very large dots containing up to ~ 49 electrons which again improves the convergence of fRG. In our case, we were able to really observe the transition between a QPC to a QD with only one electron, while the flat barrier top stayed close to the chemical potential, see fig. 6.34. For this plot, we have used a feedback range of $L = 20$ in order to render our fRG flow convergent. Note that this value is on the scale of the dot width, which was here chosen to be also 20 sites. Looking at the conductance plot, we indeed see the development of the Kondo plateau, predicted by general theoretic considerations. By summing over the density in the inner region of the dot, naturally defined by the two minima in the density, we can get the occupation number of the dot. If we carry this out for the density profile in our right plot in fig. 6.34, we obtain a occupation of 0.9952 electrons, which is in astonishing good agreement with theory. Note that additionally to the predictions

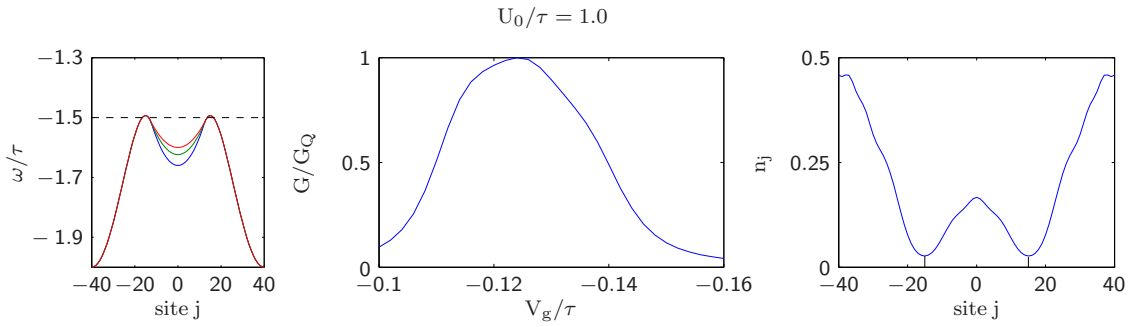


Figure 6.35.: The same plots as in fig. 6.34 but with a dot width $w_d = 30$ sites, $V_s = 0.007$ and a slightly lower gate voltage interval, enabling us to observe the 3 electron Kondo plateau. Again, the actual electron number 2.9854 was very close to the ideal theoretical prediction. Note that the Kondo plateau is somewhat broader than in our plot above and we observe again the shoulder at the flank of the conductance leading to lower gate voltage.

of the simpler SIAM, we observe here another interesting feature, namely a shoulder in the conductance on the flank of the conductance leading to lower gate voltage. We will look at this particular behavior further below.

In the next two plots fig. 6.35 and fig. 6.36, we have studied the same observables, but for the Kondo plateaus where the filling of the dot were 3 and 7 electrons, respectively.

Let us now take a look at the dependence of the conductance on the magnetic field, see fig. 6.37. Switching on such an external magnetic field lifts the spin degeneracy for the single occupied levels since the Zeeman term leads to a higher energy for the spin down electrons and favors the spin up ones. Theory predicts that with lifting this degeneracy, the Kondo effect should be suppressed, since scattering processes which flip the spin of the electron of the bound state become more and more unlikely. In fact, this is exactly what we observe in fig. 6.37: The larger the external magnetic field strength becomes, the more gets the conductance on the Kondo plateau suppressed and eventually develops into the two peak structure we have mentioned above. At this point, we want to finally comment on the shoulder that we have observed above in the flank of the conductance leading to lower gate voltage. For this purpose, we tracked the position of the effective level position ω_{eff} in our QD during a sweep over the gate voltage. The relevant effective level position ω_{eff} we evaluated here by simply keeping track of the corresponding peak in the LDOS, cf. fig. 6.33. In order to make the very sharp peak visible, we have added a small imaginary part to the real frequency argument of the LDOS which broadens the peak a bit and makes it numerically traceable. Concretely, we studied here again the Kondo plateau with 3 electrons, see fig. 6.38. We see that during the conductance sweep, coming from higher V_g values, the effective level position shows the following behavior. First, it decreases linearly with V_g , then it enters a region in which it stays almost constant and then begins again to decrease linearly in V_g . In an ideal SIAM as was for example studied in [13] and [33], in this region where its drop is reduced the effective

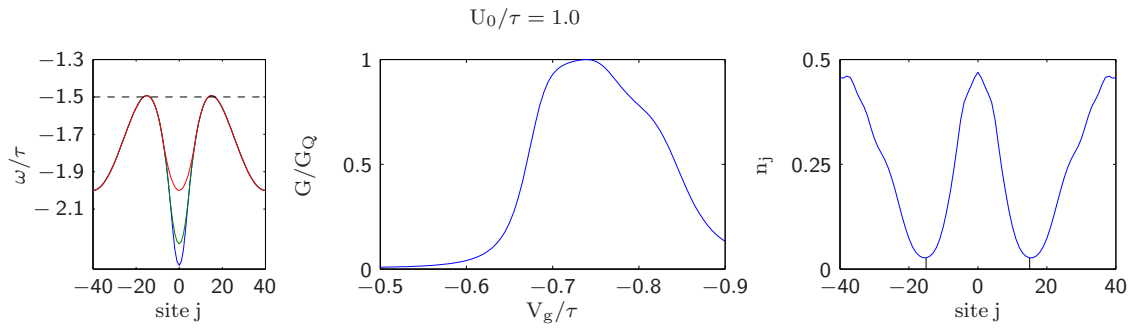


Figure 6.36.: Again, the same plots as in fig. 6.34, now with a dot width $w_d = 30$ sites and a site gate voltage of $V_s = 0.007$. The gate voltage interval was now chosen to cover the Kondo plateau with 7 electrons. Note that this time the left flank of the conductance is steeper than in the 3 electron case, becoming more of the form one would expect in an idealized model as the SIAM (cf. [13]). However, the shoulder in the other flank is still there, in fact, becoming once again slightly more prominent than in the 3 electron case. The actual electron number in the QD was here evaluated to 6.9504.

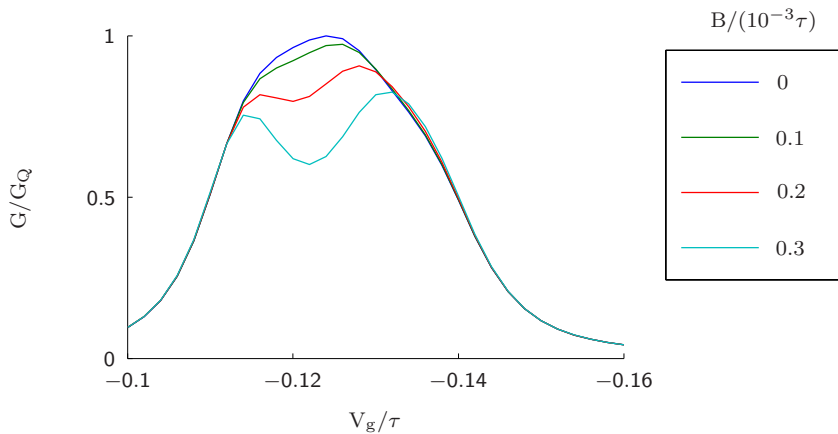


Figure 6.37.: The conductance plotted against gate voltage for the 3 electron dot, used in fig. 6.35 and different magnetic fields B . When the strength of the magnetic field is increased, the conductance at the Kondo plateau becomes suppressed and eventually develops into a two peak structure. Note that this behavior seems not to effect the shoulder on the "right" conductance flank. In fact, the conductance is there slightly increased with rising magnetic field strength.

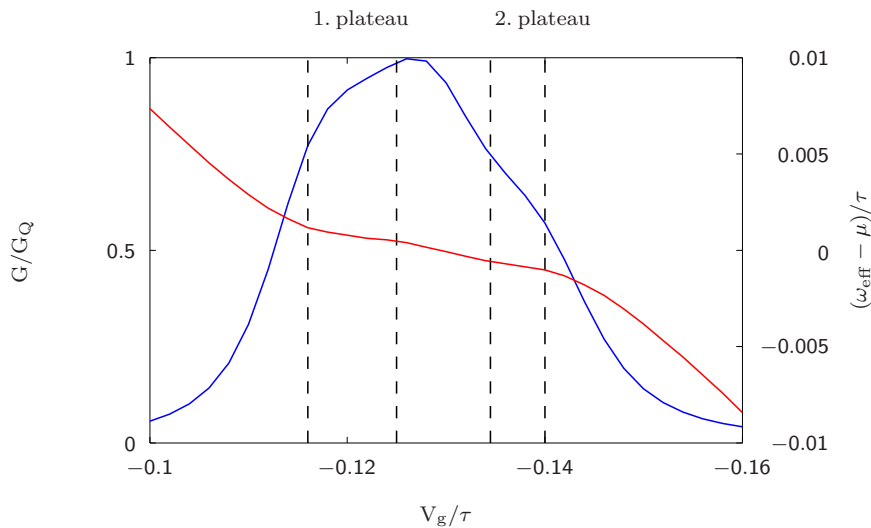


Figure 6.38.: Study of a quantum dot with width $d_w = 30$ and a site gate voltage of $V_s = 0.001$, in which case the shoulder in the conductance is slightly more pronounced than in the case studied in fig. 6.35. Blue curve: The conductance plotted against gate voltage. Red curve: the effective level position plotted against gate voltage. We remark here that for numerical reasons we had to insert a small imaginary part in the calculation of the LDOS in order to render the very sharp peak of the level visible. Note that the effective level position develops two plateaus, one at the Kondo plateau in the conductance and one at the position of our shoulder.

level position stays pinned exactly at the chemical potential μ . In our case, however, we note a slightly different behavior, since we seem to have two plateau like regions. The first lies at the same gate voltage as the Kondo plateau in the conductance and slightly above the chemical potential, while the second one corresponds to the shoulder we have observed earlier and lies slightly under the chemical potential. Thus, we see that the behavior in the conductance is consistent with the one observed in the LDOS. However, the physical origin for this shoulder is still unknown to us and could be a topic for further research.

7. Summary and outlook

Here, we will briefly summarize our work and give an outlook on possible future research topics.

The intent of this thesis was to try to understand the influence of longer ranged interactions in QPCs. For this purpose, we employed the functional renormalization group (fRG) which is known from previous works (cf. [13, 33]) to be a flexible and relatively cheap tool in computation time. We used the fRG-flow equations in the typical fRG-approximation, namely setting all vertices γ_n involving more than $n = 2$ particles to zero. The next step was to split the vertex flow into three different channels which then were treated by a coupled ladder approximation (CLA). This scheme was introduced in [20] and [21] to study the frequency dependence of the single impurity Anderson model (SIAM) and has been extended in [19] to spacial inhomogeneous models. From a diagrammatic point of view, the idea is closely related to summing up RPA-diagrams for the individual channels but taking a controlled feedback between the channels into account. By controlled we mean in this context that the index structure of the individual channels should be conserved under this feedback. Eventually, we ended up with a set of ordinary differential equations which we tackled numerically, employing the Dormand-Prince Runge Kutta method [23]. Furthermore, in the actual solution of the equations we assumed the two-particle vertex as frequency independent, causing the self-energy to be frequency independent, too. This approximation, called "static fRG" was seen to produce the results of the on-site interaction case reasonable well. (For a comparison between static fRG and a dynamic one, i.e. one with frequency dependent two particle vertex see [19]). By doing a comparison on the on-site model between our new algorithm with the previous one, i.e. the one without longer ranged feedback, we saw that our new algorithm tends to be somewhat more convergent. Due to this fact, we applied it to two situations which tend to be difficult for fRG for essentially the same reason: The effective interaction strength in our systems is measured in units of $\sqrt{\Omega_x \tau}$ where Ω_x is the curvature of the potential barrier at the top. Thus in simple words: the flatter the barrier, so much the worse becomes the convergence of the fRG flow. Our particular cases at hand were, firstly, the transition from a quantum point contact to a quantum dot, while the barrier top stays near the chemical potential during this transition. This essentially leads to a point where one has a almost horizontal barrier top, implying very small curvature and therefore a high effective interaction strength. The second case was to look at the behavior of a QPC with a non-parabolic potential when turning on interactions. For this purpose, we used quartic, sextic and octic potential barriers. Each of this barriers leads to a non monotonic increase -showing Fabry-Perot like resonances- of the conductance, see [31]. Since higher order potentials are flatter around their extrema, the fRG convergence is again challenging.

Finally we proceeded to apply our new method to QPCs with longer ranged interactions. To get a grasp at a physical reasonable model of this interactions, we used the approach of [27] and first integrated out the z - and y -direction to arrive at an effective one dimensional model. Of course, there are still some parameters which have to be fixed manually, like the ratio of the on-site and the off-site interactions or the screening caused by the surrounding gates. We used different values for this parameters and tried to determine the different regimes which can be observed in the observables. Most noticeable, we encountered the fact that in the right regime an increase in the off-site interaction can lead to an increase in the conductance. By examining this effect in more detail, in particular the electron density in the center of the QPC we tried to give an physical explanation of this strange behavior. In fact, we speculated that the effect in this regime is caused by the relatively strong off-site repulsion making it possible for a single electron to enter the center of the barrier at a far higher gate voltage than in the on-site case and thus giving rise to a Wigner like crystallization effect [30].

So far, we have summarized our methods and results which we have obtained until now. Additionally, we want to give some outlook on interesting questions that could be studied further. At first, we will mention here again our Wigner like crystallization effect in the QPC for longer ranged interactions. In this context, it would be an interesting task to define some weight with which one could compare the strength of the on- and off-site interactions. If one succeeded in this, the next step could be to try to understand the behavior that electrons can enter the barrier top due to longer ranged interactions in a more quantitative way and estimate the resulting pinch-off in the conductance. To achieve this, one would have to develop an understanding of the connection between interaction strength and range and the characteristic length l_x of the potential in order to give a precise definition of the "inner region" of the QPC.

Another interesting behavior which would need further investigation, is the shoulder in the conductance flank to lower V_g values that we have observed in our study of the QPC-QD transition. We could trace this behavior back to a second plateau in the dependence of the effective level position on the gate voltage but weren't able to identify it's physical origin.

A more technical task would be to actually implement our algorithm with longer ranged feedback without neglecting the frequency dependence of the two-particle vertices and thus also in the self-energy. Since in our algorithm the self-energy was frequency independent, we effectively mapped our interacting model to a non-interacting one. In the on-site case this procedure is known (cf. [19]) to give quite accurate results. In the case of longer ranged feedback, however, it remains an open task to use a "dynamical" longer ranged fRG scheme to see if this approximation is indeed justified. If such a dynamical method led to significant discrepancies, it would be very interesting to see how the spacial structure of the interaction is exactly connected to the frequency structure of the self-energy.

We end with an final remark on the treatment of the non-equilibrium physics in QPCs. In [1], Bauer et al. used second order perturbation theory in the Keldysh formalism to get a grasp on the behavior of the QPC when a finite source-drain voltage V_{sd} is applied. Additionally to this non-equilibrium quantity, the Keldysh technique also fa-

culated calculations for finite temperature which turned out to be quite tedious using the Matsubara formalism. These second order calculations were able to give the right qualitative behavior but give in the zero temperature case not quantitatively the same as the fRG approach. Therefore, our group is currently working on the development of an Keldysh fRG scheme for spatially inhomogeneous systems in order to combine the advantages of both methods.

A. Concrete form of the Kubo susceptibility

In this appendix, we will supply for the interested reader the explicit form of the equation for the Kubo susceptibility in the notation introduced in chapter 4. We recall the formula (3.97) from section 3.6

$$\begin{aligned}
X_j = & -\frac{T}{4} \sum_{\sigma, \omega_n} \mathcal{G}_{jk}^{R\sigma}(\omega_n) \mathcal{G}_{kj}^{R\sigma}(\omega_n) - \frac{T}{4} \sum_{\sigma, \omega_n} \mathcal{G}_{j\alpha_1}^{R\sigma}(\omega_n) \mathcal{G}_{\alpha_1 j}^{R\sigma}(i\omega_n) \\
& - \frac{1}{2\beta} \sum_{\sigma, \omega_n} \sigma \mathcal{G}_{jk}^{R\sigma}(\omega_n) \frac{T}{2} \sum_{n', j_1, j_2, j_3, \sigma'} \sigma' \mathcal{G}_{j_1 j_2}^{\sigma'}(\omega'_n) \mathcal{G}_{j_2 j_3}^{\sigma'}(\omega'_n) \\
& \times \gamma_2(j_3 \sigma' \omega'_n, k \sigma \omega_n; j_1 \sigma' \omega'_n, l \sigma \omega_n) \mathcal{G}_{lj}^{R\sigma}(\omega_n),
\end{aligned} \tag{A.1}$$

where we assume summation over all repeated indices, except j . We have already commented on the evaluation of the first two terms, thus we will here focus on the last term. Splitting the γ_2 vertex into the different channels we obtain

$$\begin{aligned}
& -\frac{1}{4} T^2 \sum_{\sigma, \sigma', \omega_n, \omega'_n} \sigma \sigma' \mathcal{G}_{jk}^{R\sigma}(\omega_n) \mathcal{G}_{j_1 j_2}^{R\sigma'}(\omega'_n) \mathcal{G}_{j_2 j_3}^{R\sigma'}(\omega'_n) \mathcal{G}_{lj}^{R\sigma}(\omega_n) \\
& \times \left[P_{j_3 k j_1 l}^{\sigma' \sigma} + X_{j_3 k j_1 l}^{\sigma' \sigma} + D_{j_3 k j_1 l}^{\sigma' \sigma} + \nu(j_3 \sigma', k \sigma; j_1 \sigma', l \sigma) \right].
\end{aligned} \tag{A.2}$$

Since $B = 0$, we can drop the spin labels on the propagators and obtain after performing the spin summation

$$\begin{aligned}
& -\frac{1}{2} T^2 \sum_{\omega_n, \omega'_n} \mathcal{G}_{jk}^R(\omega_n) \mathcal{G}_{j_1 j_2}^R(\omega'_n) \mathcal{G}_{j_2 j_3}^R(\omega'_n) \mathcal{G}_{lj}^R(\omega_n) \\
& \times \left[P_{j_3 j_1}^{\uparrow \uparrow (k-j_3)(l-j_1)} + X_{j_3 j_1}^{\uparrow \uparrow (l-j_3)(k-j_1)} + D_{j_3 l}^{\uparrow \uparrow (j_1-j_3)(k-l)} + \nu(j_3 \uparrow, k \uparrow; j_1 \uparrow, l \uparrow) \right. \\
& \left. - \left(P_{j_3 j_1}^{\uparrow \downarrow (k-j_3)(l-j_1)} + X_{j_3 j_1}^{\uparrow \downarrow (l-j_3)(k-j_1)} + D_{j_3 l}^{\uparrow \downarrow (j_1-j_3)(k-l)} + \nu(j_3 \uparrow, k \downarrow; j_1 \uparrow, l \downarrow) \right) \right].
\end{aligned} \tag{A.3}$$

Using our previously established symmetries (4.33) we can cast this into the form

$$\begin{aligned}
& -\frac{1}{2} T^2 \sum_{\omega_n, \omega'_n} \mathcal{G}_{jk}^R(\omega_n) \mathcal{G}_{j_1 j_2}^R(\omega'_n) \mathcal{G}_{j_2 j_3}^R(\omega'_n) \mathcal{G}_{lj}^R(\omega_n) \\
& \left[P_{j_3 j_1}^{\uparrow \uparrow (k-j_3)(l-j_1)} - D_{j_1 j_3}^{\uparrow \uparrow (l-j_1)(k-j_3)} - P_{j_3 j_1}^{\uparrow \downarrow (k-j_3)(l-j_1)} - X_{j_1 j_3}^{\uparrow \downarrow (l-j_1)(k-j_3)} \right. \\
& \left. + D_{j_3 l}^{\uparrow \uparrow (j_1-j_3)(k-l)} + \bar{X}_{j_3 l}^{\uparrow \downarrow (j_1-j_3)(k-l)} + \nu(j_3 \sigma, k \sigma; j_1 \sigma, l \sigma) - \nu(j_3 \sigma, k \bar{\sigma}; j_1 \sigma, l \bar{\sigma}) \right].
\end{aligned} \tag{A.4}$$

Now we can take advantage of our approximative treatment of longer ranged feedback and replace two summations over the whole central region by reduced summations over

p, q from $-L, L$ where L is the feedback range. We finally end up with

$$\begin{aligned}
& -\frac{1}{2}T^2 \sum_{\omega_n, \omega'_n} \mathcal{G}_{j(p+j_3)}^R(\omega_n) \mathcal{G}_{j_1 j_2}^R(\omega'_n) \mathcal{G}_{j_2 j_3}^R(\omega'_n) \mathcal{G}_{(q+j_1)j}^R(\omega_n) \\
& \quad \times \left[P_{j_3 j_1}^{\uparrow\uparrow pq} - D_{j_3 j_1}^{\uparrow\uparrow pq} - P_{j_3 j_1}^{\uparrow\downarrow pq} - X_{j_3 j_1}^{\uparrow\downarrow pq} \right. \\
& \quad \left. + \nu(j_3\sigma, p+j_3\sigma; j_1\sigma, q+j_1\sigma) - \nu(j_3\sigma, p+j_3\bar{\sigma}; j_1\sigma, q+j_1\bar{\sigma}) \right] \quad (\text{A.5}) \\
& -\frac{1}{2}T^2 \sum_{\omega_n, \omega'_n} \mathcal{G}_{j(q+l)}^R(\omega_n) \mathcal{G}_{(j_3+p)j_2}^R(\omega'_n) \mathcal{G}_{j_2 j_3}^R(\omega'_n) \mathcal{G}_{lj}^R(\omega_n) \\
& \quad \times \left[D_{j_3 l}^{\uparrow\uparrow pq} + \bar{X}_{j_3 l}^{\uparrow\downarrow pq} \right]
\end{aligned}$$

In the $T \rightarrow 0$ case, the frequency summations become integrals, which can be computed numerically. However, these integrations are relatively expensive in computation time and thus our preferred method for computing the susceptibility was to use a difference quotient, as explained earlier in section 3.6.

B. List of Figures

1.2. Cut through the semiconducting layers of our GaAlAs-GaAs structure . . .	8
1.1. Bandstructures of the semiconductors GaAlAs and GaAs	8
1.3. Saddlepoint like potential	9
1.4. Quantized conductance in the original paper by Van Wees et al.	10
3.1. Graphical depiction of our model Hamiltonian	20
3.2. Depiction of the current operator	24
3.3. Paths in the complex plane for the conductance computation	31
3.4. Paths in the complex plane for the density computation	35
4.1. Diagrammatic form of the flow equations for the vertex	43
4.2. Graphical depiction of the block matrix structure in the vertex quantities	57
4.3. The independent elements of the $P^{\sigma\sigma}$ channel	66
4.4. The independent elements of the $P^{\uparrow\downarrow}$ and $X^{\uparrow\downarrow}$ channels	66
4.5. The independent elements of the $\bar{X}^{\uparrow\downarrow}$ channel	67
4.6. The independent elements of the $D^{\sigma\sigma}$ channel	67
5.1. Tight binding chain	69
5.2. LDOS of a tight binding chain	70
5.3. LDOS of a tight binding chain in a color plot.	70
5.4. LDOS of a chain with parabolic barrier top	70
5.5. Dependence of the LDOS at the center of the QPC on the frequency . . .	71
5.6. The non-interacting conductance as a function of the gate voltage	72
5.7. Conductance for different on-site interaction strengths	72
5.8. The spin resolved, non-interacting conductance	73
5.9. On-site interacting, spin resolved conductance	74
5.10. Magnetic field dependence of the on-site interacting conductance	74
5.11. The local electron density	75
5.12. The total susceptibility for the on-site case	76
5.13. The local susceptibility for the on-site case	76
6.1. The on-site conductance with varying feedback lengths	78
6.2. The shifted on-site conductance with varying feedback lengths	79
6.3. The total on-site susceptibility with varying feedback lengths	80
6.4. The local on-site susceptibility with varying feedback lengths	80
6.5. The conductance for longer ranged feedback and various on-site interac- tion strengths	81

6.6. The total susceptibility for longer ranged feedback and various on-site interaction strengths	81
6.7. Comparison between the Kubo and the ordinary site resolved susceptibilities	82
6.8. The self-energies for the on-site interacting case with different feedback lengths	83
6.9. The diagonals of the self-energies for the on-site interacting case with different feedback lengths	83
6.10. The first and second off-diagonals of the self-energies for different feedback ranges	84
6.11. The conductance resulting from truncation of the selfenergy	85
6.12. Tight binding chain with effectively reduced hopping	85
6.13. Change in the potential shape due to reduced central hopping	86
6.14. Diagrammatic relation between the selfenergy and the two particle vertex	87
6.15. The different vertex contributions to the first off-diagonal of the self-energy	88
6.16. The magnitude of the different channels plotted against gate voltage for different interaction strengths	89
6.17. Graphical depiction of the $X_{ji}^{\sigma\bar{\sigma}00}$ channel plotted for $L = 0$	90
6.18. The $X_{ji}^{\sigma\bar{\sigma}lk}$ channel for the $L = 2$ case	91
6.19. The electron density distribution in the z-direction of a 2DEG	92
6.20. The interaction strength $W_{l_2}(\Delta x)$	95
6.21. The discretized interaction as used in our calculations	96
6.22. Conductance curves for longer ranged interactions for different l_2	97
6.23. The local susceptibilities for different l_2	99
6.24. The conductance for different magnetic fields with $l_2 = 1.88$	99
6.25. The conductance for very small off-site interactions	101
6.26. The self-energy in the regime of the conductance shift	101
6.27. The electron density in the regime of the conductance shift	102
6.28. A Wigner like crystallization effect	103
6.29. The density n_0 at the center of the QPC as a function of gate voltage . .	103
6.30. The conductance of a quartic barrier QPC for varying on-site interaction strengths	105
6.31. The conductance of a sextic barrier QPC for varying on-site interaction strengths	106
6.32. The conductance of a octic barrier QPC for varying on-site interaction strengths	106
6.33. The non-interacting LDOS for a quantum dot potentia	107
6.34. The transition from a QPC to a QD hosting one electron	108
6.35. A quantum dot hosting 3 electrons	109
6.36. A quantum dot hosting 7 electrons	110
6.37. The conductance for the 3 electron dot for different magnetic fields B . .	110
6.38. Analysis of the effective level position	111

C. Bibliography

- [1] Bauer Florian, Heyder Jan, Schubert Enrico, Borowsky David, Taubert Daniela, Bruognolo Benedikt, Schuh Dieter, Wegscheider Werner, von Delft Jan, and Ludwig Stefan. Microscopic origin of the ‘0.7-anomaly’ in quantum point contacts. *Nature*, 501(7465):73–78, Sep 2013.
- [2] B. J. van Wees, H. van Houten, C. W. J. Beenakker, J. G. Williamson, L. P. Kouwenhoven, D. van der Marel, and C. T. Foxon. Quantized conductance of point contacts in a two-dimensional electron gas. *Phys. Rev. Lett.*, 60:848–850, Feb 1988.
- [3] S. Ratz, A. Donarini, D. Steininger, T. Geiger, A. Kumar, A. K. Hüttel, C. Strunk, and M. Grifoni. Thermally induced subgap features in the cotunneling spectroscopy of a carbon nanotube. *ArXiv e-prints*, August 2014.
- [4] K. J. Thomas, J. T. Nicholls, M. Y. Simmons, M. Pepper, D. R. Mace, and D. A. Ritchie. Possible spin polarization in a one-dimensional electron gas. *Phys. Rev. Lett.*, 77:135–138, Jul 1996.
- [5] Yigal Meir, Kenji Hirose, and Ned S. Wingreen. Kondo model for the “0.7 anomaly” in transport through a quantum point contact. *Phys. Rev. Lett.*, 89:196802, Oct 2002.
- [6] S. M. Cronenwett, H. J. Lynch, D. Goldhaber-Gordon, L. P. Kouwenhoven, C. M. Marcus, K. Hirose, N. S. Wingreen, and V. Umansky. Low-temperature fate of the 0.7 structure in a point contact: A kondo-like correlated state in an open system. *Phys. Rev. Lett.*, 88:226805, May 2002.
- [7] Chuan-Kui Wang and K.-F. Berggren. Local spin polarization in ballistic quantum point contacts. *Phys. Rev. B*, 57:4552–4556, Feb 1998.
- [8] Léon Van Hove. The occurrence of singularities in the elastic frequency distribution of a crystal. *Phys. Rev.*, 89:1189–1193, Mar 1953.
- [9] Y.V. Nazarov and Y.M. Blanter. *Quantum Transport: Introduction to Nanoscience*. Cambridge University Press, 2009.
- [10] R. Landauer. Spatial variation of currents and fields due to localized scatterers in metallic conduction. *IBM J. Res. Dev.*, 1(3):223–231, July 1957.
- [11] J.W. Negele and H. Orland. *Quantum Many-particle Systems*. Advanced Books Classics. Westview Press, 2008.
- [12] V. Meden. Lecture notes on the *Functional renormalization group*.

-
- [13] C. Karrasch. Transport Through Correlated Quantum Dots – A Functional Renormalization Group Approach. *eprint arXiv:cond-mat/0612329*, December 2006.
- [14] S. Andergassen, T. Enss, C. Karrasch, and V. Meden. A Gentle Introduction to the Functional Renormalization Group: The Kondo Effect in Quantum Dots. In B. Barbara, Y. Imry, G. Sawatzky, and P. C. E. Stamp, editors, *Lecture Notes in Physics, Berlin Springer Verlag*, volume 645 of *Lecture Notes in Physics, Berlin Springer Verlag*, pages 1–4020, 2008.
- [15] Henrik Bruus and Karsten Flensberg. *Many-body quantum theory in condensed matter physics - an introduction*. Oxford University Press, 2004.
- [16] A. Oguri. Transmission Probability for Interacting Electrons Connected to Reservoirs. *Journal of the Physical Society of Japan*, 70:2666, September 2001.
- [17] Nikolai Ufer. Conductance anomalies in quantum point contacts functional renormalization group applied to a 2d hubbard model. Master’s thesis, LMU München, 2011.
- [18] G.D. Mahan. *Many-Particle Physics*. Physics of Solids and Liquids. Springer, 2000.
- [19] F. Bauer, J. Heyder, and J. von Delft. Functional renormalization group approach for inhomogeneous interacting Fermi systems. *Phys. Rev. B*, 89(4):045128, Jan 2014.
- [20] C. Karrasch, R. Hedden, R. Peters, T. Pruschke, K. Schönhammer, and V. Meden. A finite-frequency functional renormalization group approach to the single impurity Anderson model. *Journal of Physics Condensed Matter*, 20:H5205, Aug 2008.
- [21] Severin G. Jakobs, Mikhail Pletyukhov, and Herbert Schoeller. Nonequilibrium functional renormalization group with frequency-dependent vertex function: A study of the single-impurity anderson model. *Phys. Rev. B*, 81:195109, May 2010.
- [22] T. R. Morris. The Exact Renormalization Group and Approximate Solutions. *International Journal of Modern Physics A*, 9:2411–2449, 1994.
- [23] J.R. Dormand and P.J. Prince. A family of embedded Runge-Kutta formulae. *Journal of Computational and Applied Mathematics*, 6(1):19–26, 1980.
- [24] M. Büttiker. Quantized transmission of a saddle-point constriction. *Phys. Rev. B*, 41:7906–7909, Apr 1990.
- [25] O. Goulko, F. Bauer, J. Heyder, and J. von Delft. The effect of spin-orbit interactions on the 0.7-anomaly in quantum point contacts. *ArXiv e-prints*, August 2014.
- [26] R. van Leeuwen, N. E. Dahlen, and A. Stan. Total energies from variational functionals of the Green function and the renormalized four-point vertex. *Phys. Rev. B*, 74(19):195105, November 2006.

-
- [27] A. M. Lunde, A. DeMartino, A. Schulz, R. Egger, and K. Flensberg. Electron-electron-interaction effects in quantum point contacts. *New Journal of Physics*, 11(2):023031, Feb 2009.
- [28] Florian Bauer. *Microscopic Origin of the 0.7-Anomaly in Quantum Point Contacts*. PhD thesis, LMU München, 2014.
- [29] A. Jeffrey and D. Zwillinger. *Table of Integrals, Series, and Products*. Elsevier Science, 2000.
- [30] E. Wigner. On the interaction of electrons in metals. *Phys. Rev.*, 46:1002–1011, Dec 1934.
- [31] J. Heyder, F. Bauer, E. Schubert, D. Borowsky, D. Schuh, W. Wegscheider, J. von Delft, and S. Ludwig. On the relation between the 0.7-anomaly and the Kondo effect: Geometric Crossover between a Quantum Point Contact and a Kondo Quantum Dot. *ArXiv e-prints*, Sep 2014.
- [32] Jun Kondo. Resistance Minimum in Dilute Magnetic Alloys. *Progress of Theoretical Physics*, 32(1):37–49, 1964.
- [33] Florian Bauer. 0.7 anomaly of quantum point contacts treatment of interaction with functional renormalization group. Master’s thesis, LMU München, 2008.
- [34] M. Büttiker, Y. Imry, R. Landauer, and S. Pinhas. Generalized many-channel conductance formula with application to small rings. *Phys. Rev. B*, 31:6207–6215, May 1985.
- [35] A.L. Fetter and J.D. Walecka. *Quantum Theory of Many-particle Systems*. Dover Books on Physics. Dover Publications, 2003.
- [36] J. Zinn-Justin. *Quantum Field Theory and Critical Phenomena*. International series of monographs on physics. Clarendon Press, 2002.
- [37] S. Datta. *Electronic Transport in Mesoscopic Systems*. Cambridge Studies in Semiconductor Physics and Microelectronic Engineering. Cambridge University Press, 1997.
- [38] I.N. Bronštejn, G. Musiol, and H. Mühlig. *Taschenbuch der Mathematik*. Deutsch, 2008.
- [39] A. Altland and B. Simons. *Condensed Matter Field Theory*. Cambridge University Press, 2006.
- [40] Katharina Eissing. Functional renormalization group applied to a multimode quantum point contact. Master’s thesis, LMU München, 2013.

Acknowledgment

I thank Jan von Delft for the topic and the supervision of this work. I enjoyed the working in his group and the kind and uncomplicated atmosphere very much.

A very special thanks goes to Florian Bauer and Jan Heyder for tutoring me and giving me tons of advice regarding physics, programming and writing of this thesis. Furthermore, they let me use their matrix class, ODE-solver and various other code that I used throughout this thesis.

A big thanks also to Dennis Schimmel who always had the time to answer my questions and giving me lots of advice on field theory, diagrams and physics in general. Aside from that, he always picked us up for lunch and made sure -by the hard work of counting- that nobody was forgotten.

Furthermore, I want to thank Olga Goulko for giving me her spin-orbit data for comparison.

I would also like to thank my office colleagues Dimitri "Dima" Pimenov, Nils-Oliver Linden, and Kevin Jägering for the bright office atmosphere and lots of shared cookies. Furthermore, I thank our next door colleague and friend Johannes Hauschild for sharing his superior latex skills with me.

In the very end, I thank my parents who supported me during my whole studies and were always there for me.

Statement of authorship

Herewith, I certify that this thesis is the result of my own work and that I have only used the acknowledged sources.

Munich, November 14, 2014

(Lukas Weidinger)